INTEGRATED CIRCUIT “ASTROLABE” ANGULAR DISPLACEMENT SENSOR USING ON-CHIP PINHOLE OPTICS

by

Udumbara Wijesinghe

APPROVED BY SUPERVISORY COMMITTEE:

____
Dr. Mark Lee, Chair

____
Dr. Hal Edwards

____
Dr. Andrew Marshall

____
Dr. William Vandenberghe

____
Dr. Chadwin Young

To year 2020, for reducing the lab work and the length of this dissertation

INTEGRATED CIRCUIT “ASTROLABE” ANGULAR DISPLACEMENT SENSOR USING ON-CHIP PINHOLE OPTICS

by

UDUMBARA WIJESINGHE, BS, MS

DISSERTATION

Presented to the Faculty of

The University of Texas at Dallas

in Partial Fulfillment

of the Requirements

for the Degree of

DOCTOR OF PHILOSOPHY IN

MATERIALS SCIENCE AND ENGINEERING

THE UNIVERSITY OF TEXAS AT DALLAS

December 2020

ACKNOWLEDGMENTS

I want to extend my sincere gratitude to my PhD advisor Professor Mark Lee for being a caring and fantastic mentor. I have been working with Professor Lee since Fall 2016 on two different projects. Being his first research student on Silicon optical devices, I had to build everything from nothing. I needed his constant advice and support in selecting and buying necessary parts and equipment, designing experiments, measurement setups, and Graphical User Interfaces to collect data. The many discussions we have had throughout the years helped me to improve my knowledge and skills. I consider myself fortunate to work with someone inspired and motivated and always wondered how I got the weekly schedule at 6:30 every Monday morning. I highly appreciate his guidance and immense patience throughout the years.

I am indebted to the knowledge I gained from Dr. Hal Edwards of Texas Instruments, who has been a close collaborator, honorary mentor, great visionary, and a caring friend for me these years. My research is based on his idea of an optical sensor and the prototype layouts he designed. I worked with him two summers as a visiting researcher and an intern at Texas Instruments. He always encouraged me to think "outside the box" and helped me to design industrial-level sensors from simple sketches I made on a PowerPoint, which was a dream come true. His guidance and support in theoretical and TCAD modeling are priceless. He always amazed me with how much one can do in a lifetime.

I wish to express my deepest gratitude to Professor Andrew Marshall and Akash Dey of the UTD Electrical Engineering Department, who supported me with amplifier circuit designs and Noise Model. The knowledge I gained from them is invaluable.

I would also like to thank my PhD committee members, Professor Chadwin Young and Professor William Vandenberghe, for being on my committee and for providing constructive comments and insights. They were very supportive throughout the exam scheduling process, and it could not have been any better without them.

I want to pay special regards to my Texas Instruments collaborators Dr. William Krenik, Dr. Can Duan, Dr. Matthew Thompson, Dr. Robert Doering, Dr. Rahmi Hezar, Dr. Robert Todd, Dr. John Arch, Dr. Tami McQuhae, Dr. Shaoping Tang, Dr. Clint Naquin, and Dr. Timothy Rost for permitting me to use the design tools at Texas Instruments and spending their valuable time on helping me to design the second generation of the Astrolabe sensors. They all were extremely talented and kind-hearted individuals. Discussions I had with them and the experience we share grow my interest in working in the industry.

I want to thank David Taylor, Ashley Willess, and Julie Welch for their support. I would also like to show gratitude to the amazing professors I met in the Materials Science and Engineering, Physics, and Electrical Engineering departments who gave me advice for life and for the most extraordinary knowledge they shared.

I wish to thank my two smart sisters and friends, who made my life more cheerful and eventful. I am indebted to my loving parents for always being by my side while encouraging me to go forward and constantly asking me, "so when will you graduate" (I'm done finally!).

Finally, I would like to thank `YOU,' who took the trouble to read this when there are so many important things to read in the following pages.

November 2020

INTEGRATED CIRCUIT “ASTROLABE” ANGULAR DISPLACEMENT SENSOR USING ON-CHIP PINHOLE OPTICS

Udumbara Wijesinghe, PhD
The University of Texas at Dallas, 2020

Supervising Professor: Mark Lee

An integrated circuit sensor capable of tracking the angular displacement of an object tagged with a quasi-point source of light, such as a light emitting diode (LED), is designed, developed, experimentally characterized and physically modeled. The sensing element consists of four photo-cathodes enclosed inside an integrated circuit metal box with a pinhole aperture, which eliminates the need for external focusing optics. The angular displacement of an LED along both orthogonal latitudinal and longitudinal arcs is encoded as normalized photo-cathode current imbalances. A set prototype sensor including variations in aperture shape, aperture dimension, cathode separation, surface gratings, and blocking structures were fabricated using industrially standard “0.18 μm technology node” silicon complementary metal-oxide semiconductor (CMOS) technology. In these prototype sensors, the sensor signal is found to be linearly proportional to LED angular position across an approximately ± 50° field-of-view. A simple one-dimensional model of sensor response is developed, and the fundamental performance characteristics of prototype sensors are presented. A figure-of-merit is introduced that helps determine the uncertainty in angular measurement for a given measurement bandwidth and incident optical power. In these prototype astrolabes, the amplified signal figure-of-merit roughly a factor of 10 worse than needed to be practically useful.

Based on the results of the prototype sensors, a wide range of improved second-generation sensor layout variations was designed, fabricated, and experimentally tested. Second-generation astrolabe variations included, anode gratings, guard rings, aperture area variations, cathode separation variations, cathode type variations, unit cell dimension variations and some sensors had integrated on-chip preamplifiers. The improved features and their impact on sensor characteristics are presented. More advanced physics-based 1-d and 2-d theoretical models have been derived in order to understand the operating principles of the sensor thoroughly. Numerical technology computer-aided design (TCAD) models of the type used widely in the semiconductor industry have been used to simulate the device physics of the sensors. The figure-of-merit obtained from the unamplified signals of the second generation astrolabes is three times better than that of the prototype sensors. However, second generation sensors show only 30% improvement with signal amplification compared to the 85% improvement resulted from the sensor first generation. Possible noise sources that could affect the sensor performance have been studied, modeled and a new measurement setup is proposed to track the angular position of a moving object in real time.

TABLE OF CONTENTS

LIST OF FIGURES

LIST OF TABLES

CHAPTER 1

INTRODUCTION

Sensors capable of tracking the motion of an object through space – *i.e.*, giving an electronic readout that encodes an object's 2- or 3-dimensional position at different times – can find numerous applications ranging from feedback control of robotic motion, position fixing and distance triangulation, automated tool alignment, and proximity actuation of a device or function [1] [2] [3] [4] [5] For these kinds of applications a sensor should be able to track displacements on human time- and distance scales, *i.e.*, at ≥ 1 m of the distance across its field-of-view at video rate bandwidth or faster (≥ 100 Hz), and have a reasonable spatial resolution as defined by a specific application, but typically < 1 mm [6](Fig 1.1).

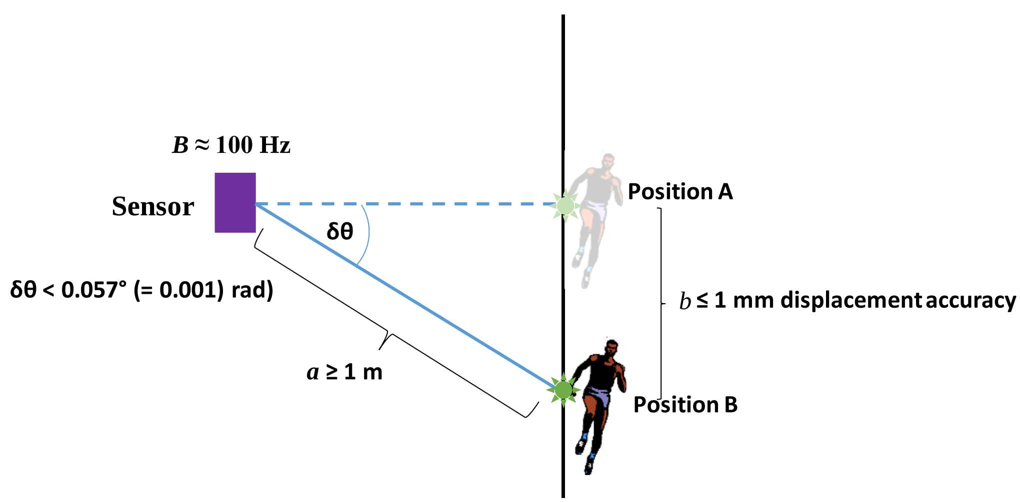

Fig.1.1: Geometrical parameters of the sensor application *a*- radial distance across the field of view which is ≥ 1 m. *b*- displacement resolution which is < 1 mm and the corresponding angular resolution $\delta\theta < 0.057°$.

Active pixel sensor (APS) cameras that track objects using video capture and image analysis [7] [8] [9], are probably the most widely known existing technology in this application space. The major drawback of APS systems relates to their cost and complexity.

Relatively expensive APS imaging chips and readout circuits, very high quality external optics, and dedicated high-speed image processing are needed. For simple repetitive displacement sensing tasks where imaging is unnecessary, a less complicated, more cost-effective form of displacement sensing is desirable.

Position sensitive detectors (PSD), routinely used for optical alignment, output a current or voltage giving the 2-d coordinates of a light spot on a sensor surface. Most PSDs employ either quadrant photodiodes (QPD) [10] [11] or lateral effect photosensors (LEP) [12] [13] [14]. Used with focusing optics and/or laser spot illumination, PSDs can track the displacement of an object tagged by a light source. QPDs are typically used to measure small displacement changes, such as the deflection of an atomic force microscope cantilever [15]. LEP systems have been used to track a laser-illuminated corner cube at distances > 100 m by monitoring the laser's retro-reflection [16].

In this dissertation we introduce a simple integrated circuit (IC) sensor that generates an analog signal proportional to the angular displacement of an object tagged by a quasi-point source of light. The angular signal is derived from an imbalance in photocurrents arising from the position of a light spot cast by the light tag through an integrated pinhole aperture onto a silicon surface between matched photocathodes. Because of a resemblance to the ancient star-tracking navigational tool called an Astrolabe [17], we call this type of sensor an IC Astrolabe. Unlike in APS systems, Astrolabes do not require external optics or any electronics for image processing which makes them easy to fabricate.

QPDs and LEPs also output a normalized photocurrent imbalance to indicate light spot position on their surfaces. However, the physical mechanism generating the astrolabe's signal is different. Unlike QPDs, the astrolabe does not require a light spot to overlap multiple photocathodes, making the astrolabe's response insensitive to the shape of the light spot. Also, the fact that the light spot in an astrolabe can be far from any cathode permits it to sense light spot position over a longer length scale than a QPD. Unlike an LEP, the astrolabe does not employ the lateral photoelectric effect. Consequently, the *p-n* junction area in an astrolabe can be made significantly smaller than in an LEP, reducing total dark current and parasitic capacitance. LEPs are also highly sensitive to surface recombination and the material quality of a thin heavily doped layer [18], problems avoided in the astrolabe design.

The use of pinhole optics (Fig.1.2) is simple and offers complete freedom from linear distortion, virtually infinite depth of field and an angular field that can be made up to 90°. It obviates the need for sophisticated optics such as external lenses, mirrors, and optical alignment which saves the fabrication cost, reduce the weight and size of the sensor, and results in greater mechanical and thermal stability since there is no need to maintain optical alignment against mechanical motions / vibrations and temperature changes [19]. Astrolabes can also operate against normal background illumination conditions with much wider field-of-view than most existing QPD or LEP, so they are easier to use than existing PSD displacement tracking systems.

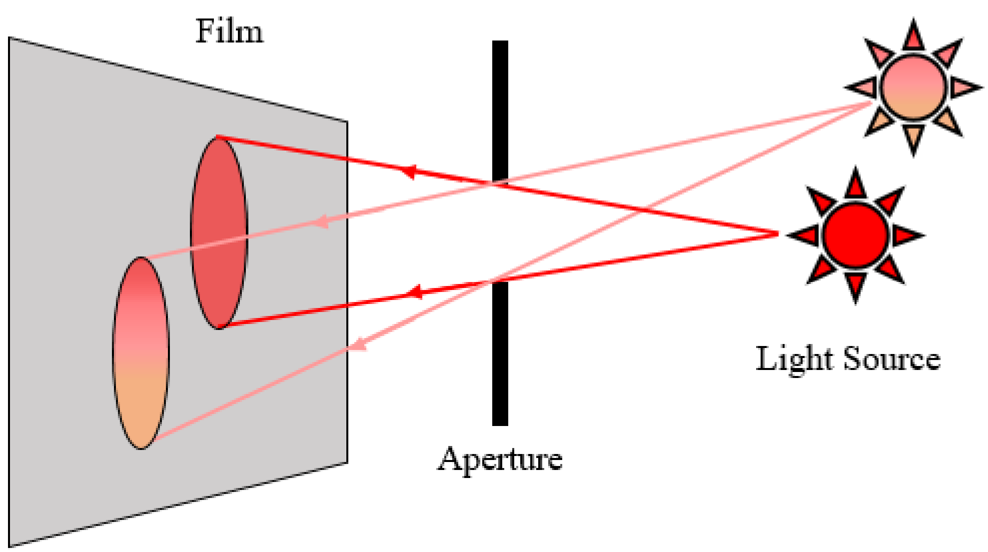

Fig.1.2: Illustration of an image casting from a pinhole aperture; the same optics are used in Astrolabe sensors.

CHAPTER 2

SIMPLE THEORETICAL MODEL FOR SENSOR OPERATION

In this chapter we develop a simple theoretical model for a prototype Astrolabe sensor operation based on the one-dimensional time-independent diffusion of the photogenerated carriers. Corrections were made considering Snell's law of refraction and the depth dependence of the photogenerated carriers. Later we use the theoretical model to understand the behavior and performance of the prototype Astrolabe sensor with the goal of developing a new sensor with better performance.

2.1 Normalized Photocurrent

This section follows the account published in Ref. [6]. Fig. 2.1. is an illustration (not to scale) of a cross-section of an integrated circuit (IC) Astrolabe sensor unit cell. Two identical n^+-doped cathodes, C_L on the left and C_R on the right, are embedded in a *p*-doped anode equidistant from an integrated pinhole aperture. The basic operating principle consists of two steps. First, light rays from a distant point source pass through the pinhole and cast an image light spot onto the Si anode, locally generating photocarriers. Second, the relative position of this image between the pair of biased cathodes is detected as a photocurrent imbalance. The angular displacement θ_{in} of the light source is derived from this photocurrent imbalance together with the device geometry and the law of refraction.

With a point light source at distance d >> aperture dimension, the object is taken to be at infinity so parallel light rays are incident at θ_{in} relative to the normal to the aperture plane, see Fig. 2.1. Because a pinhole aperture has infinite depth-of-field [19], no focusing optics are needed to image the point source. Light rays incident from air refract through the SiO_2 and the Si anode, so the net refraction angle in the anode is $\theta_{refr} = sin^{-1}\left[\frac{sin\theta_{in}}{n_{Si}}\right]$.where the real index $n_{Si} \geq 3.5$ for above-bandgap light in Si [20]. Because n_{Si} is large, we make the approximation $\theta_{refr} \approx \theta_{in}/n_{Si}$.At a depth z into the anode, the center of the light spot is displaced a distance $\delta(z) \approx (d_{ox} + z)\,\theta_{in}/n_{Si}$ in the x-direction from the center line.

The light is absorbed in the anode, generating electron and hole photocarriers. With both cathodes positively biased at the same potential relative to the anode, photoelectrons will diffuse to and be collected by the cathodes. If θ_{in} = 0 the situation is symmetric among the cathodes, so in Fig. 2.1. the left cathode current I_L would equal the right cathode current I_R. However, if $\theta_{in} \neq 0$ then the image light spot will be closer to one cathode (C_L in Fig. 2.1.) than the other (C_R). The electrical resistance to C_L should then be smaller than the resistance to C_R, resulting in $I_L > I_R$ for the simplified 1-d geometry of Fig 2.1. Normalizing the photocurrent difference ($I_L - I_R$) to the total photocurrent ($I_L + I_R$) eliminates extensive effects like cathode area and incident light intensity. Thus, information about θ_{in} should be encoded in the normalized photocurrent difference ($I_L - I_R$)/($I_L + I_R$).

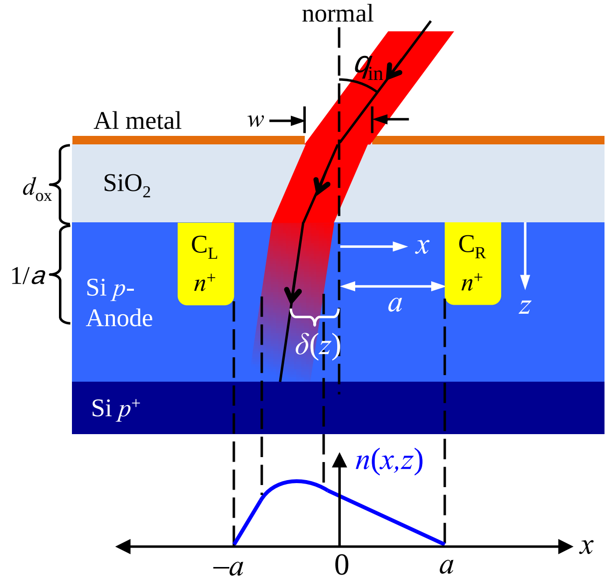

Fig.2.1: (Top) Illustration (not to scale) of a unit cell cross-section through the pinhole aperture of width w and two n^+ cathodes C_L (left) and C_R (right). A light beam incident at angle θ_{in} is indicated in red as refracting across the SiO_2 and Si layers and being absorbed in the anode. The directions x and z and dimensions a, $\frac{1}{\alpha}$, d_{ox}, and $\delta_{(z)}$are indicated. (Bottom) Sketch of the photoelectron density $n(x,z)$ that solves (2.2) and (2.3) as a function of position x between cathodes at a fixed depth z. $n(x)$ is quadratic inside the illuminated region, linear outside the illuminated region, continuous at all x, and zero at the cathodes.

The diffusion of photoelectrons generated by light absorption in the anode was calculated to form a 1-d analytical model to understand the device physics picture of the above concept. We make the simplifying assumption that every photon incident on the anode creates an electron-hole pair and neglect recombination loss in the anode (i.e., 100% quantum efficiency). From the TCAD models of the sensors the recombination loss can be found and added as a correction, this will be discussed further in Chapter 7.Taking the light intensity in the anode to be exponentially decaying characterized by a wavelength-dependent absorption coefficient α [21], charge conservation gives the total current as:

$$I_L + I_R = -qw \int_0^{\infty} U_0 \exp(-\alpha z)\, dz \tag{2.1}$$

where w is the aperture width, q is the electron charge, U_0 is the light intensity at the anode surface, and z is the depth into the anode as indicated in Fig.2. The upper integration limit can be taken to ∞ with little error since the anode thickness is > $\frac{1}{\alpha}$.

Photoelectrons are generated inside the illuminated region and diffuse in the ± x-direction towards the cathodes. The photoelectron density $n(x,z)$ at any given depth z can be obtained from the time-independent 1-d diffusion equation [22]. Outside the illuminated region, where no photocarriers are generated.

$$0 = D\frac{\partial^2 n_{(x)}}{\partial x^2} \tag{2.2}$$

$$n_{(x,z)} = Ax + B \tag{2.2.1}$$

where D is the diffusion coefficient. (2.2) is solved by a linear function (2.2.1), where A and B are arbitrary constants. Assuming each cathode is a perfect recombination center for photoelectrons diffusing in from the anode, we then require $n(\pm a,z) = 0$. Applying this condition in (2.2.1), the photogenerated carrier concentration in left region $n_{L(x,z)}$,and the right region $n_{R(x,z)}$can be written with A_1 , A_3 arbitrary constants;

$$n_{L(x,z)} = A_1\,(x + a) \qquad -a \le x \le \delta - \frac{w}{2} \tag{2.2.1.1}$$

$$n_{R(x,z)} = A_3\ (x - a) \qquad \delta + \frac{w}{2} \le x \le a \tag{2.2.1.2}$$

Inside the illuminated region, the photogenerated carrier concentration is $n_{I(x,z)}$;

$$0 = D\frac{\partial^2 n_{I(x,z)}}{\partial x^2} + U_0 e^{-\alpha z}{}_{(x,z)} \tag{2.3}$$

$$n_{I(x,z)} = \frac{-U_0 e^{-\alpha z} x^2}{2D} + Cx + E \qquad \delta - \frac{w}{2} \le x \le \delta + \frac{w}{2} \tag{2.3.1}$$

which is solved by a quadratic function (2.3.1) where, C and E are arbitrary constants. The solutions of *n*(*x*,*z*); (2.2.1.1), (2.2.1.2) and (2.3.1) must be continuous at the boundaries between illuminated and un-illuminated regions. The functional form of *n*(*x*,*z*) is sketched in Fig.2.1. (bottom). Applying boundary conditions for the continuity,

$$n_{L(x,z)}|_{\delta-\frac{w}{2}} = n_{I(x,z)}|_{\delta-\frac{w}{2}} \tag{2.4.1}$$

$$A_1\ \left(\delta - \frac{w}{2} + a\right) = -\frac{U_0 e^{-\alpha z}\left(\delta - \frac{w}{2}\right)^2}{2D} + C\left(\delta - \frac{w}{2}\right) + E \tag{2.4.1.1}$$

$$\frac{dn_{L(x,z)}}{dx}|_{\delta-\frac{w}{2}} = \frac{dn_{I(x,z)}}{dx}|_{\delta-\frac{w}{2}} \tag{2.4.2}$$

$$A_1\ = -\frac{U_0 e^{-\alpha z}\left(\delta - \frac{w}{2}\right)}{D} + C \tag{2.4.2.1}$$

$$n_{I(x,z)}|_{\delta+\frac{w}{2}} = n_{R(x,z)}|_{\delta+\frac{w}{2}} \tag{2.4.3}$$

$$-\frac{U_0 e^{-\alpha z}\left(\delta + \frac{w}{2}\right)^2}{2D} + C\left(\delta + \frac{w}{2}\right) + E = A_3\ \left(\delta + \frac{w}{2} - a\right) \tag{2.4.3.1}$$

$$\frac{dn_{I(x,z)}}{dx}|_{\delta+\frac{w}{2}} = \frac{dn_{R(x,z)}}{dx}|_{\delta+\frac{w}{2}} \tag{2.4.4}$$

$$-\frac{U_0 e^{-\alpha z}\left(\delta + \frac{w}{2}\right)}{D} + C\ = A_3 \tag{2.4.4.1}$$

The photocurrent density can then be obtained by applying Fick's law which describes the behavior of diffusive flux to the gradient of the concentration. It postulates that the flux goes from regions of high concentration to regions of low concentration, with a magnitude that is proportional to the concentration gradient [23]. for left region and right region,

$$J_{L(z)} = Dq\frac{dn_{L(x,z)}}{d(-x)} = -DeA_1 \qquad -a \le x \le \delta - \frac{w}{2}$$

$$J_{R(z)} = Dq\frac{dn_{R(x,z)}}{dx} = DeA_3 \qquad \delta + \frac{w}{2} \le x \le a \tag{2.5}$$

Solving (2.4.1.1), (2.4.2.1), (2.4.3.1) and (3.4.4.1) results in:

$$A_1 = \frac{U_0e^{-\alpha z}(a-\delta)w}{2Da} = \frac{U_0e^{-\alpha z}\left(a - d_{ox}\theta_{refr} - z\theta_{refr}\right)w}{2Da}$$

$$A_3 = -\frac{U_0e^{-\alpha z}(a+\delta)w}{2Da} = -\frac{U_0e^{-\alpha z}\left(a + d_{ox}\theta_{refr} + z\theta_{refr}\right)w}{2Da} \tag{2.6}$$

According to the Fig.2.1.; $\delta = h\theta_{refr} = (d_{ox}+z)\theta_{ref}$, where d_{ox} is the thickness of the oxide layer. Therefore;

$$J_{L(z)} = -DqA_1 = -\frac{qwU_0e^{-\alpha z}\left(a - d_{ox}\theta_{ref} - z\theta_{ref}\right)}{2a}$$

$$J_{R(z)} = DqA_3 = -\frac{qwU_0e^{-\alpha z}\left(a + d_{ox}\theta_{ref} + z\theta_{ref}\right)}{2a} \tag{2.7.1}$$

Integrating over depth gives the total left and right currents,

$$J_L = \int_0^\infty -\frac{qwU_0e^{-\alpha z}\left(a - d_{ox}\theta_{ref} - z\theta_{ref}\right)}{2a}\,dz = \frac{qwU_0}{2a\alpha}\left(-a + d_{ox}\theta_{ref} + \frac{\theta_{ref}}{\alpha}\right)$$

$$J_R = \int_0^{\infty} -\frac{qwU_0 e^{-\alpha z}\left(a + d_{ox}\theta_{ref} + z\theta_{ref}\right)}{2a}\,dz = -\frac{qwU_0}{2a\alpha}\left(a + d_{ox}\theta_{ref} + \frac{\theta_{ref}}{\alpha}\right) \qquad (2.7.2)$$

Therefore, the normalized photocurrent signal Σ;

$$\Sigma = \frac{J_{signal}}{J_{total}} = \frac{J_L - J_R}{J_L + J_R} = \left(\frac{d_{ox}}{a} + \frac{1}{a\alpha}\right)\theta_{ref} \qquad (2.8)$$

We consider the refraction at the Si-SiO$_2$ interface, by applying Snell's law of refraction [24];

$$n_{Si}\theta_{ref} = \theta_{in} \qquad (2.9)$$

where, n_{Si} is the refractive index of the Si substrate. Substituting in (2.8) will give,

$$\Sigma = \frac{J_{signal}}{J_{total}} = \frac{J_L - J_R}{J_L + J_R} = \frac{I_L - I_R}{I_L + I_R} = \left(d_{ox} + \frac{1}{\alpha}\right)\frac{\theta_{in}}{an_{Si}} \qquad (2.10)$$

where the dimensions a and d_{ox} are indicated in Fig.2.1. This shows that the normalized photocurrent imbalance signal Σ is linearly proportional to the incident angle θ_{in} with a proportionality coefficient that depends on sensor layout geometry and light wavelength. Qualitatively, this linearity should break down when θ_{in} is large enough that light shines directly on a cathode. Photoelectrons generated in a cathode do not need to diffuse to be collected and so will lead to signal saturation. From Fig.2.1, as θ_{in} increases light will initially intersect a cathode well below the anode surface where the intensity is weakest, so there should be a gradual approach to saturation. Thus, we expect the onset of a sub-linear Σ vs. θ_{in} response at relatively high θ_{in}. Using the geometry of Fig.2.1, we estimate that light starts hitting the left cathode at $\theta_{in} \approx 30°$. As a consequence, Σ should begin turning sublinear above 30° to 40°, becoming fully saturated as more intense light hits the cathode at shallower depths.

2.2 Response Time

Diode storage time is an estimate of the response time to an optical pulse. This is the total time taken by the photogenerated carriers from an optical pulse to reach the cathodes. The relation between the total photocurrent density and the total minority carrier concentration in the active area of the sensor can be written as;

$$J_{total} = \frac{-qn_{total}}{\tau} \tag{2.11}$$

Where τ is the response time of the sensor and n_{total} is the total minority carrier concentration in the active region of the sensor, which can be found by;

$$n_{total} = \int_{0}^{\infty}\int_{-a}^{a} n(x,z)dx\,dz = \int_{0}^{\infty}\int_{-a}^{\delta-\frac{w}{2}} n_{L(x,z)}dx\,dz + \int_{0}^{\infty}\int_{\delta-\frac{w}{2}}^{\delta+\frac{w}{2}} n_{I(x,z)}dx\,dz + \int_{0}^{\infty}\int_{\delta+\frac{w}{2}}^{a} n_{R(x,z)}dx\,dz$$

Solving the above equation results;

$$\tau = \left(\frac{a^2}{2D}\right)\left[1 - \frac{1}{3}\left(\frac{w}{a}\right)^2 - \left(\frac{{d_{ox}}^2\alpha^2 - 2d_{ox}\alpha - 2}{a^2\alpha^2{n_{si}}^2}\right){\theta_{in}}^2\right] \tag{2.12}$$

The above equation shows for a given wavelength the response time is determine by the cathode separation. Therefore, to gain high speed the cathode separation should be a minimum.

CHAPTER 3

ASTROLABE SENSOR FIRST GENERATION

We experimented on a set of prototype (first generation) Astrolabe sensors that included variations in aperture dimension, aperture shape, cathode position, anode grating, and the inclusion of blocking structures. These first generation Astrolabes were designed by our Texas Instruments collaborator Dr. Hal Edwards and fabricated by Texas Instruments using standard commercial Si CMOS processing technology. Based on the fundamental performance characteristics of sensitivity and noise density, we introduce a figure-of-merit (FoM) to determine the uncertainty in angular measurement for a given measurement bandwidth and incident optical power. Results obtained from aperture dimension and shape has been published [6].

3.1 Sensor Fabrication and Layout Design

The Astrolabe sensors were fabricated on a commercial 0.18 µm technology node CMOS process line normally used to fabricate power ICs. For each sensor, the anode consisted of a 20 µm thick p layer (10^{15} to 10^{17} cm^{-3}) above a deep p^+ layer (> 10^{18} cm^{-3}) on a p-type Si wafer. A d_{ox} = 10 µm layer of SiO_2 on the Si surface was grown to support an aluminum metal layer that formed the camera box. Four photo-cathodes were formed by ion implanting n^+ wells (~ 10^{17} cm^{-3}) to a depth of ~ 10 µm into the anode in a square layout (Fig.2.1). The aperture in the Al metal is centered among cathodes. The basic unit cell of each Astrolabe sensor consisted of four nominally identical photo-cathodes arranged at the corners of a 12 µm x 12 µm square encased in the pinhole camera box.

Fig.3.1 shows plan view designs (to scale) of eight sensor unit cells, called Layouts A, B, C, D, E, F, G and H. The reddish shading covering most of the cell represents the aluminum box layer on the upper surface. The center aperture opens onto the Si anode surface, colored green. The four photo-cathodes (under the aluminum box layer) are labeled C1, C2, C3, and C4.

The layouts differ in the size and shape of their apertures, cathode position, grating of the anode substrate and blocking structures placed in the middle of photo active area. Layouts A-F have plus shaped apertures.

The “+” shaped aperture was tried because it was thought that illuminating an extended line could make the photoelectron diffusion process more one-dimensional and hence closer to the simple 1-d analytical model of Chapter 2.

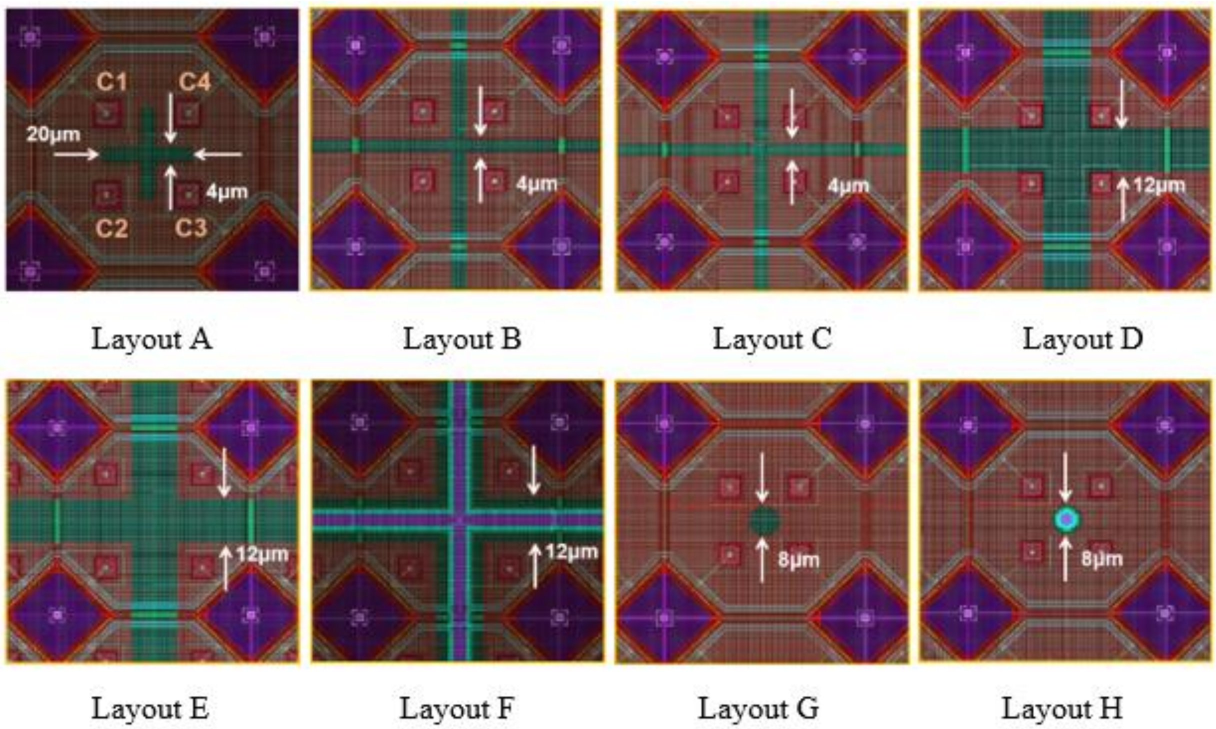

Fig.3.1: Plan view of the Astrolabe sensor unit cell design layouts (to scale), referred to as Layouts A-H. Reddish shaded regions represent the top Al metal. Aperture openings are green, which indicates the anode surface. The cathodes are the four squares labeled C1, C2, C3, and C4 in Layout A.

Layout A has a small “+” aperture, while Layout B extends the arms of the “+” to the cell boundaries. Layout C is very similar to Layout B except the anode surface has a grating to minimize the reflection of incident light. Layout D has widened slits compared to Layout B, and Layouts E and F are modifications of Layout D. Cathode position is varied in Layout E to identify the role in cathode position in normalized photocurrent signal as displayed in Eq. (2.10.)

Layout F also has the same cathode separation as layout E in addition to a blocking structure to decrease the signal level for very bright objects. Layout G has a more conventional octagonal, nearly circular, small pinhole aperture. Layout H is a modification of Layout G with a blocking structure in the middle of the photoactive area. Dimension details of the layout aperture and the special features are given in Table 3.1. The % Open Area is the ratio of the aperture area to the unit cell area.

Table 3.1: Layout aperture type, shape, area and special features.

Layout Name	Aperture Shape	Aperture Area (um2)	% Open Area	Special Features
A	Plus	144	5.76	Small slit
B	Plus	384	15.4	Full slit
C	Plus	384	15.4	Anode grating
D	Plus	1056	42.2	Wide full slit
E	Plus	1056	42.2	Cathode pulled back
F	Plus	1056	42.2	Blocking Structure
G	Octagon	53	2.11	Smaller aperture
H	Octagon	53	2.11	Blocking Structure

Each Astrolabe chip consisted of an array of $8 \times 8 = 64$ identical unit cells, each cell 50×50 μm^2, for a total chip area of 400×400 μm^2. All 64 C1 cathodes were connected in parallel to a common C1 bonding pad to output a total current I_1, and similarly for C2, C3, and C4 and their currents I_2, I_3, and I_4. Each chip had a common anode bonding pad used as the circuit ground. Each chip was mounted in an uncovered 8-pin dual inline package (DIP) (Fig.3.2).

Unlike the model of Chapter 2, the actual Astrolabes were 2-dimensional and tracked angular displacement in two orthogonal arcs. Sweeping a light source along a latitudinal arc (left⇔right in Fig.3.1, like latitude lines on a map), the left-side photocurrent is $I_L = I_1 + I_2$, and the right-side current is $I_R = I_3 + I_4$. From Eq. (2.10), the normalized latitudinal signal Σ_{LAT} is then:

$$\Sigma_{LAT} = \frac{(I_1 + I_2) - (I_3 + I_4)}{I_1 + I_2 + I_3 + I_4} \tag{3.1.1}$$

Sweeping a light source along a longitudinal arc (top⇔bottom in Fig.3.1, like longitude lines on a map), the top-side photocurrent is $I_1 + I_4$, and the bottom-side current is $I_2 + I_3$. The normalized longitudinal signal Σ_{LON} is then:

$$\Sigma_{LON} = \frac{(I_1 + I_4) - (I_2 + I_3)}{I_1 + I_2 + I_3 + I_4} \tag{3.1.2}$$

Σ_{LAT} and Σ_{LON} are orthogonal. For general 2-d angular displacements, the azimuthal angle ϕ relative to the latitudinal direction is given by $\phi = tan^{-1}\left[\frac{\Sigma_{\mathrm{LON}}}{\Sigma_{\mathrm{LAT}}}\right]$.

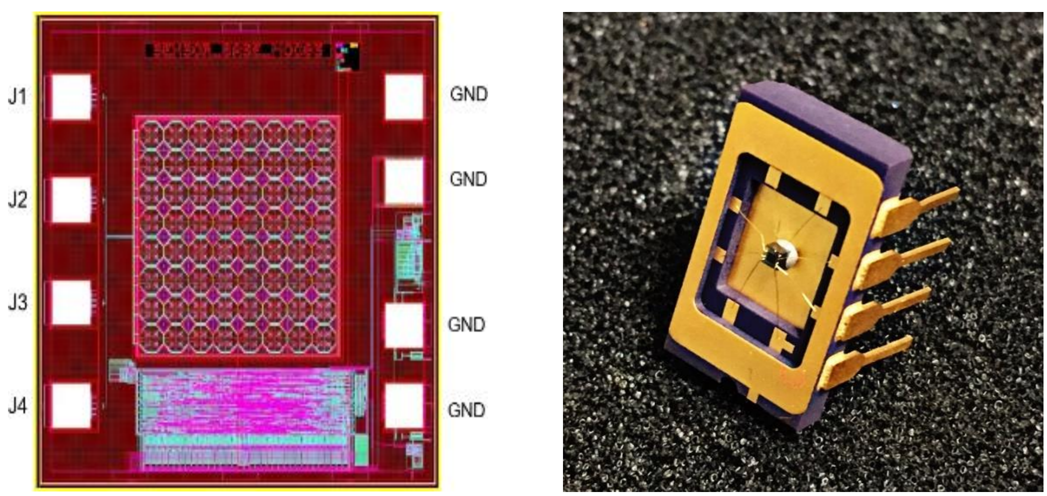

Fig.3.2: (a) Pin configuration of the sensor, four ground connections of each photodiode and cathode connections. (b) The packaged device, connections are wire bonded to the package pins.

3.2 Experimental Procedure

To measure performance, an open DIP containing an Astrolabe chip was plugged into a vector board socket and mounted on a Thorlabs PRMTZ8 digitally controlled rotation stage, with the chip centered on the rotation axis. An LED, fixed in position, was used as the quasi-point source of light. LEDs of wavelength 830 nm (infrared), 660 nm (red), and 525 nm (green) were used. The LED was typically placed 0.2 m from the sensor, facing normal to the plane of the vector board when the rotation stage was set at 0°. Data were also taken at greater distances. Optical power incident onto to the DIP package was determined by placing a Thorlabs S130C power sensor directly in front of the sensor chip prior to rotation measurements. At any wavelength, LED intensity was adjusted through a combination of LED bias and distance so that the incident power was 300 µW over the 9.5 mm diameter aperture of the power sensor. Assuming uniform illumination, total power incident on the 400 × 400 μm^2 sensor chip was then 0.68 µW.

During measurements, all anode-cathode *pn* junctions were reverse biased at a constant 1.5 V. At this bias the photocathodes were current sources, so a quad transimpedance amplifier (TIA) (LMP2234) was mounted on the same vector board and connected to the Astrolabe DIP via short (~ 1 cm) soldered wires. The TIA generated four output voltages $V_n = -RI_n$ (n = 1 to 4) where R is the fixed transimpedance. These V_n can thus be used in place of the currents I_n to calculate Σ_{LAT} and Σ_{LON} using Eq. (3.1).

Angular sensitivity measurements were performed by rotating the sensor from –90° to +90° relative to the LED in 1° steps, where 0° represents normal incidence. At each rotation angle, the amplified photocurrents V_1, V_2, V_3, V_4 were measured using Keithley 2401 Source Measure Units with 21.7 ms integration time and 10 count averaging. Photocurrent noise measurements were measured by recording a 50 s time record of each V_n with 21.7 ms time constant, no averaging, at fixed angle. Average and variance statistics were then computed from these time records. In all cases photocurrents were first measured with LED off in both dark (black box) and ambient laboratory light conditions. The power meter read about 30 nW in the dark and 30 µW in ambient light with LED off. Photocurrents were then measured with LED on against both dark and ambient background light conditions.

Photocurrent signal data shown here are the difference between LED on and LED off in ambient light conditions, *i.e.* $V_n = V_n$(LED on) – V_n(ambient light) at each rotation angle. These are the V_n used to compute the normalized current ratio signals defined in (3.1) at each angle for an arc sweep.

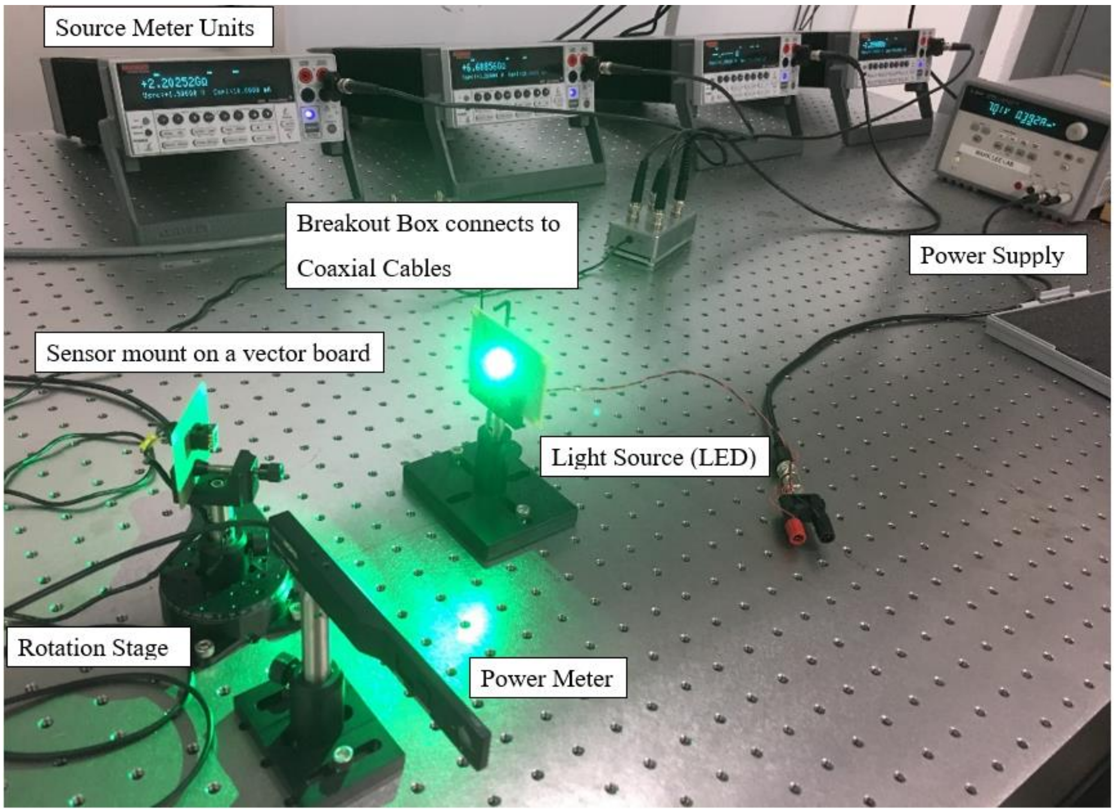

Fig.3.3: Overview of the experimental setup; the sensor DIP is mounted on a vector board and fixed on a rotation stage perpendicular to the LED light source, powered by the power supply. The resulting photocurrent signals are connected to BNC cables of the Source Meter Units through a breakout box. An optical power meter could be placed on the same plane as the sensor to record incident power from the LED.

3.3 Sensor Performance and Characterization

3.3.1 Horizon and Field-of-View

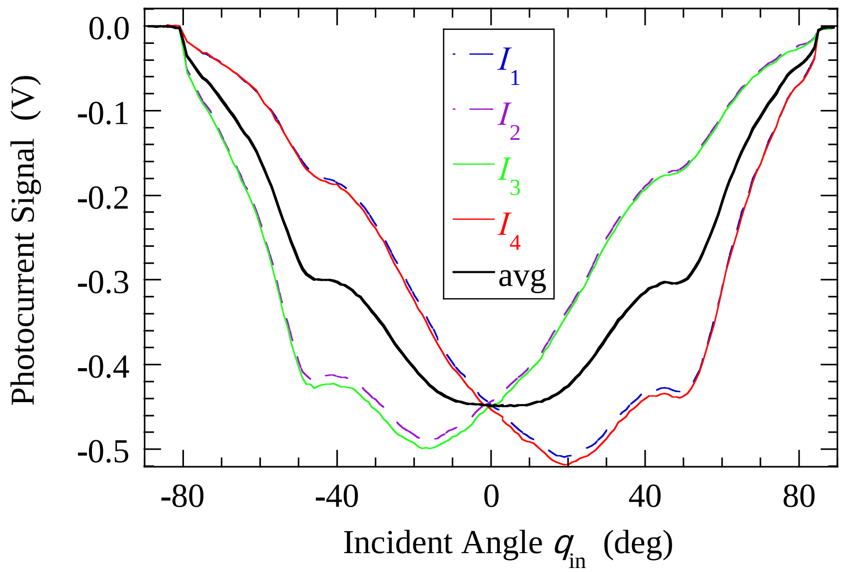

Fig.3.4: Amplified photocurrent signal I_1 from cathode C1 (dashed blue), I_2 from cathode C2 (dashed purple), I_3 from cathode C3 (solid green) and I_4 from cathode C4 (solid red) along with the average of these four signals (solid black) for a Layout A sensor plotted against light incidence angle for a longitudinal sweep.

Fig.3.4 shows the photocurrent signals as defined in the preceding paragraph for each cathode as a function of θ_{in} for a Layout A sensor using a 660 nm LED light tag swept longitudinally from –90° < θ_{in} < 90°. These currents are clearly angle-sensitive with a horizon of nearly ± 80°, beyond which insufficient light from the LED enters the pinhole. Also shown is the average of the four cathode signals, which has a maximum at 0°. Fig.3.5 (a) shows Σ_{LAT} and Σ_{LON} from a Layout A sensor for: i) a longitudinal arc sweep, and ii) a diagonal arc sweep at $\phi \approx 45°$, *i.e.* in the direction from cathodes C1 ⇔ C3 in Fig.3.1 For the longitudinal sweep, Σ_{LAT} is essentially zero, demonstrating the orthogonality of longitudinal and latitudinal signals. For the diagonal sweep, $\Sigma_{\mathrm{LAT}}/\Sigma_{\mathrm{LON}} \approx 1$ as expected since tan (45°) = 1. For the longitudinal sweep in Fig.3.5 (a), Σ_{LON} is essentially linear with θ_{in} for relatively low angles as expected from Eq. (2.10).

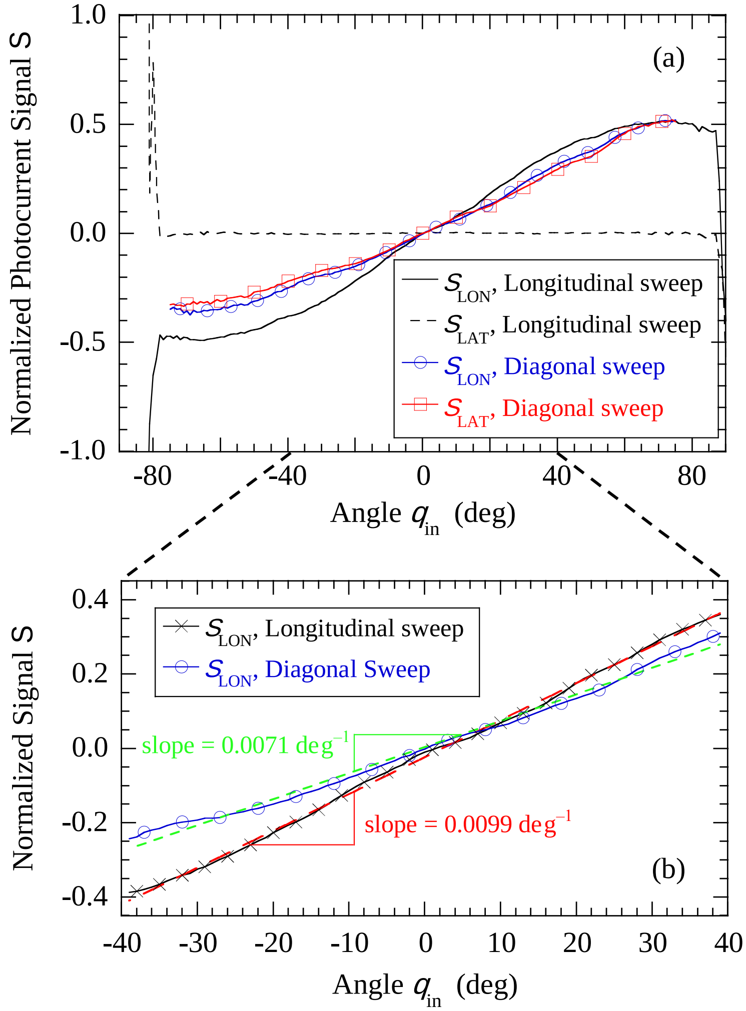

Fig.3.5: (a) Normalized photocurrent signals Σ_{LON} (solid black) and Σ_{LAT} (dashed black) for a longitudinal sweep, and Σ_{LON} (blue with open circles) and Σ_{LAT} (red with open squares) for a diagonal sweep at $\theta \approx 45°$ azimuth angle from the latitude direction. (b) Detail of the low angle longitudinal signals from -40° < θ_{in} 40°. The red dashed line is a linear fit to the longitudinal sweep data, and the green dashed line is a linear fit to the diagonal sweep data.

At higher angles Σ_{LON} becomes sub-linear, as described at the end of Chapter 2. The physical horizon at which light incident on the aperture no longer hits the anode is near ± 80°, close to the absolute geometrical limit of ± 90°. However, although the signal-to-noise ratio is still good for $|\theta_{in}|$ between 50° and 80°, Σ_{LON} becomes too weakly dependent on θ_{in} to determine angle.

We therefore define the linear field-of-view to be the θ_{in} where $|\Sigma_{LON}|$ falls 1 dB below its low angle linear extrapolation, in analogy to gain compression of an amplifier. For all layouts this linear field-of-view is around ± 50°.

3.3.2 Angular Sensitivity

The layouts differ in the magnitude of the signal slope at low angles. From Fig.3.5, we define the angular sensitivity $S = \Delta\Sigma/\Delta\theta_{in}$ as the slope of a line fit to the Σ_{lon} vs. θ_{in} data for $|\theta_{in}| < 40°$, as shown in Fig.3.5 (b). A larger value of S means greater sensitivity to small changes in θ_{in}. Table.3.2 shows S for a longitudinal sweep for the sensor layouts at the three wavelengths used.

Table 3.2: Angular Sensitivity

Layout	Sensitivity (deg-1)		
	830 nm	660nm	525 nm
A	0.0064	0.0090	0.0086
B	0.0033	0.0045	0.0044
C	0.0049	0.0051	0.0048
D	0.0025	0.0035	0.0034
E	0.0023	0.0031	0.0029
F	0.0036	0.0048	0.0047
G	0.0072	0.0101	0.0096
H	0.0091	0.0131	0.0128

The experimental results show that S is higher for layouts with smaller % Open Area, probably the result of the light spot being more localized for smaller apertures. The blocking structures placed in the middle of the active area allows the light into the edges. Higher S obtained from layouts with blocking structures compared to its identical layout without the blocking structure shows that the light collected at the center of the aperture does not contribute to the S as much as the edges which are more dependent on the shadowing by the aperture edges.

According to Eq. (2.10), greater S is expected for Layout E in comparison with Layout D due to the increased cathode separation from 12 µm to 19.5 µm. This disagreement with empirical results may be due to photocarrier recombination over a long distance which suggest carrier lifetime and the time dependency of the diffusion equations should be considered for a more complete understanding. The anode grating in Layout C (0.25 µm wide lines with 0.525 µm pitch) shows a 47% increase at 830 nm and roughly 10% increase at visible wavelengths in S compared to that of Layout B (0.45 µm wide squares with 0.75 µm pitch), highlighting the fact that adding a roughness to the anode surface can improve the sensor performance. However, the dimensions, periodicity, and the shape of the grating to be optimized.

In addition, S increases as wavelength decreases from 830 nm to 660 nm and remains nearly constant between 660 nm to 525 nm. Since n_{Si} increases by about 10% from 830 nm to 525 nm [20], Eq. (2.10) predicts S should be slightly larger for 830 nm compared to 525 nm light, opposite to what is observed. A possible reason for the discrepancy is the neglect of recombination in the 1-d model. The 830 nm light can generate photoelectrons below the depth of the cathode, requiring those electrons to diffuse upward via a longer path that yields a higher probability of recombination.

Eq. (2.10) from the 1-d model shows that S depends on sensor geometry through the parameters a and d_{ox} and on wavelength through α. Empirically, although a and d_{ox} are the same for Layout A, B, D and G, S is still layout dependent at any given wavelength. The reason for this may be the 2-d nature of the actual devices. Intrinsically 2-d design parameters such as shape and area of the pinhole aperture and carrier diffusion in a plane cannot be captured in a 1-d model. Therefore, to understand the behavior of the sensors a 2-d model is needed which accounts the 2-d diffusion of the photocarriers, an advanced 2-d model will be discussed in Chapter 4.

3.3.3 Angular Noise Density

Fig.3.6. shows a time record of Σ_{LON} using a 660 nm LED for a longitudinal sweep using a Layout A sensor. From this data, the signal noise density (in Hz$^{-1/2}$) is $\sigma\tau^{1/2}$, where σ is the standard deviation of Σ_{LON} and τ is the measurement integration time. The data of Fig.3.6 was measured using $\tau = 21.7$ ms.

The angular noise density η (in deg/Hz$^{1/2}$) is then $\eta = \sigma\tau^{1/2}/S$. Table.3.3 summarizes angular noise density values measured for the sensor layouts and wavelengths under our standard measurement conditions.

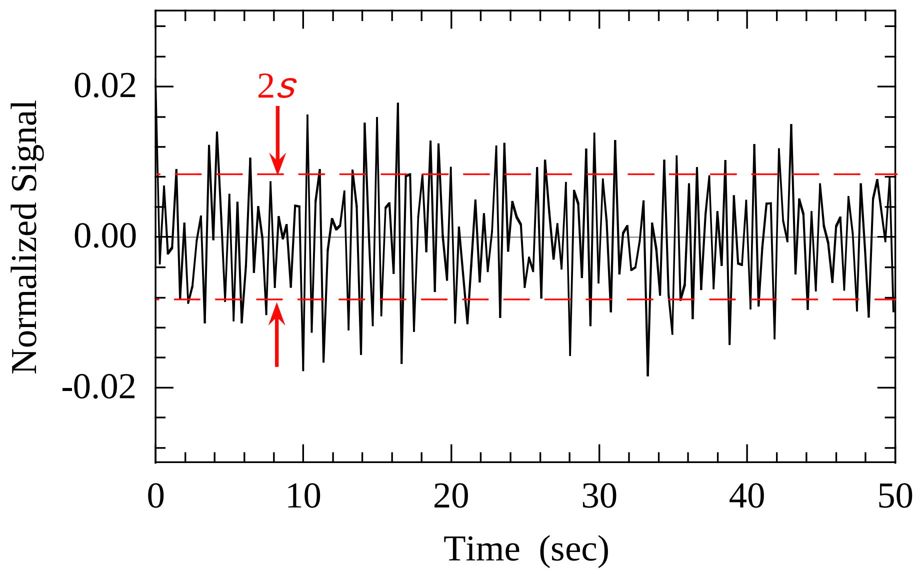

Fig.3.6: Normalized longitudinal sweep signal (solid black) recorded as a function of time using a 21.7 ms time constant. The red dashed lines represent ± one standard deviation (σ) about the average.

Experimental results show that η is lowest for 660 nm light compared to 830 nm and 525 nm. Increased noise at 525 nm may arise because the carriers are generated closer to the SiO_2 interface, where interface roughness and dangling bonds may act as significant noise sources. At 830 nm η is larger than at 660 nm because of a lower experimental S value. As expected, the data also show that the smaller aperture results in higher η due to fewer photo-generated carriers at the anode surface. Similar understanding can be used to describe the results obtained from the sensors with blocking structures. Also, as described in the sensitivity data analysis, recombination effects might reduce the number of photogenerated carriers sensed by the cathodes in layouts with pulled-back cathodes and hence increase η. Significantly high η at 525nm for Layout C is possibly due to the increase in anode surface area and hence the number of SiO_2 dangling bonds.

However, the effects of surface gratings still need to be analyzed thoroughly to understand its effects on sensor performance. Chapter 6 will discuss the impact of gratings on an advanced sensor in detail.

Table 3.3: Angular Noise Density

Layout	Noise Density (deg/√Hz)		
	830 nm	660nm	525 nm
A	0.144	0.108	0.184
B	0.143	0.110	0.167
C	0.085	0.092	0.191
D	0.092	0.083	0.132
E	0.091	0.091	0.138
F	0.103	0.089	0.125
G	0.328	0.283	0.410
H	0.491	0.374	0.554

3.3.4 Figure of Merit

Fig.3.7 shows that at fixed wavelength η scales inversely with light power P_{in} from 0.05 to 1.6 μW incident onto the chip. Because ηP_{in} = constant for a given sensor layout and LED wavelength, we introduce this as a figure-of-merit (FoM) for the Astrolabe sensor. This FoM is useful because the angular uncertainty $\delta\theta$ associated with an angle measurement using light power P incident onto the chip and measurement bandwidth B is then $\delta\theta$ = (FoM) $B^{1/2}/P$. Since the goal is to minimize $\delta\theta$ within application bandwidth and illumination power limitations, the FoM value should be minimized. Table.3.4 summarizes the FoM values for each layout at different LED wavelengths.

To estimate how small a FoM value needs to be in order to be practically useful, we define a simple criterion: tracking human time-scale motions with ≤ 1 mm displacement accuracy along an arc at a distance of 1 m from the sensor requires an angular uncertainty $\delta\theta < 0.057°$ (= 0.001 rad) at video rate bandwidths, *i.e.* $B \approx 100$ Hz. To accomplish this requires $\eta < 0.0057$ deg/Hz$^{1/2}$.

If $P = 1$ μW is incident on the chip, this requires FoM < 0.057×10^{-7} deg·W/Hz$^{1/2}$. Comparing this to Table.3.4, Layout D at 660 nm has the minimum FoM but is a factor of 10 times higher than the FoM value needed to achieve this level of accuracy.

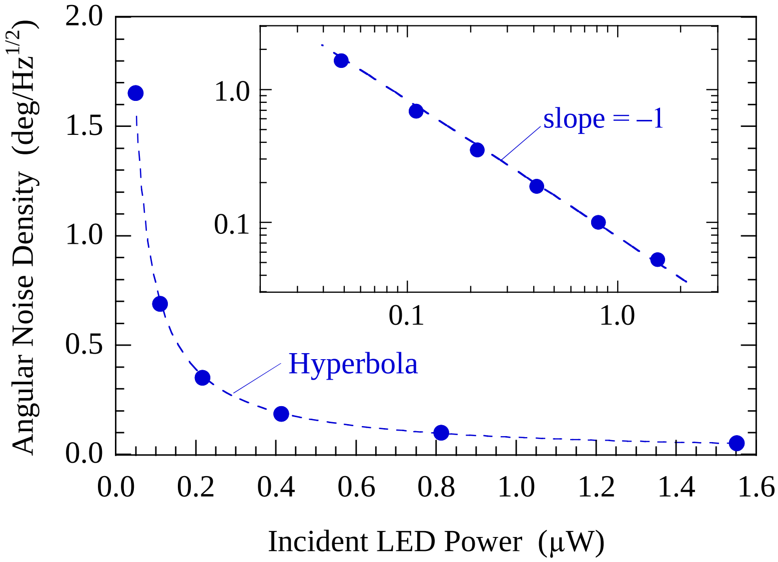

Fig.3.7: Angular noise density vs. LED illumination power incident onto sensor chip Layout A against a dark background. The dashed line in the main figure is a fit to a hyperbola. Inset: same data plotted on a log-log scale. The dashed line indicates a slope of –1.

Table 3.4: Figure of Merit

Layout	FoM (10^{-7} deg.W/√Hz)		
	830 nm	660nm	525 nm
A	1.04	0.76	1.38
B	1.04	0.77	1.25
C	0.65	0.64	1.38
D	0.69	0.59	0.96
E	0.68	0.64	0.99
F	0.74	0.62	0.90
G	2.39	1.98	2.94
H	3.69	2.64	4.10

3.3.5 Sensor Speed

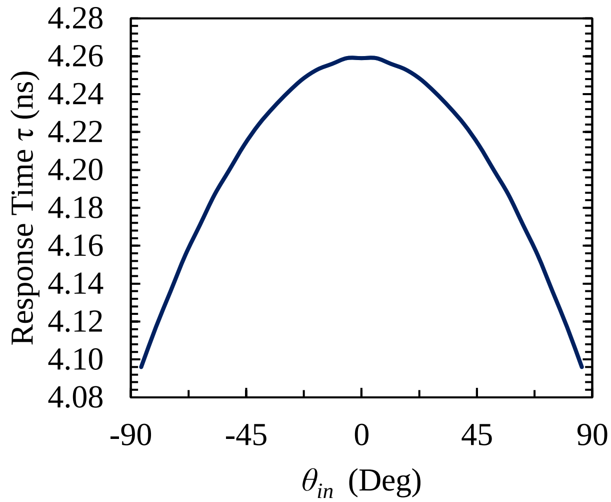

Fig.3.8: Response Time with θ_{in} calculated from Eq. (2.12) for a unit cell of layout A with 12 µm cathode separation, 4 µm aperture width, and d_{ox}= 10 µm under the illumination of for 660 nm wavelength LED.

The speed of a photodiode is determined by two factors; The response time of the photocurrent and the RC time constant of its equivalent circuit. The response time of the sensor can be estimated by the diode storage time for an optical pulse. The variation of response time with θ_{in} under the illumination of 660 nm wavelength LED for a unit cell of layout A is shown in Fig.3.8. The values were calculated from the Eq.(2.12) with D, the diffusion coefficient for Si D=3.6×10^{-3} m^{2}s^{-1}, wavelength dependent parameters n_{si}=3.8, α=2.58×10^5 µm^{-1} [20] and the layout parameters a=12 µm, d_{ox}= 10 µm, and w= 4 µm. According to the Eq. (2.12), a determines the response time and the effect of other parameters are negligible. The estimated result is ~ 4 ns. From Fig.3.8 the response time is for any practical purpose independent of angle, varying by < 4% about the mean from +90° to -90°.This result is understandable because the photogenerated carriers travel across 6 µm distance. However, in a practical world this value can be altered by the intrinsic resistance of the sensor layout as the sensor unit cell contains four photocathodes and the layout contains an array of sensors connected in parallel.

The speed of the photodiode is dependent on the input impedance of the trans impedance amplifier (TIA) because the intrinsic capacitance of the diode junction combines with this impedance to produce a low pass filter. The speed of the Astrolabe sensor for practical applications were investigated by our collaborators at the Electrical Engineering Department Dr. Andrew Marshall and Akash Dey.

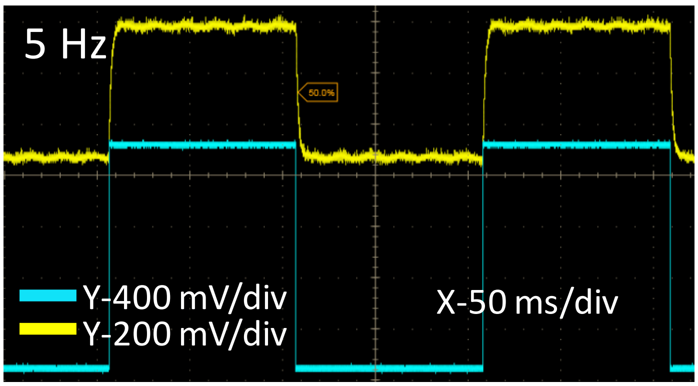

(a)

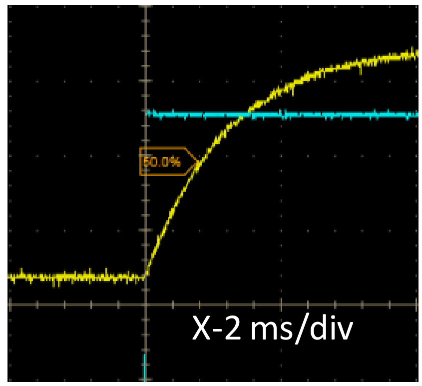

(b)

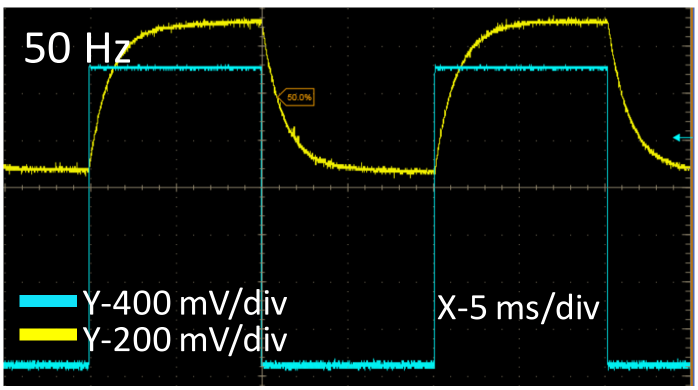

(c)

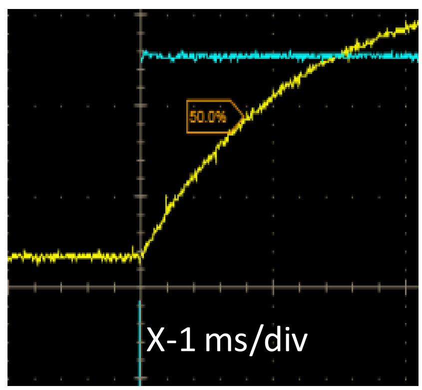

(d)

Fig.3.9: Oscilloscope traces of a square wave driven (blinking) LED in blue and the corresponding Astrolabe photodiode (cathode C1 and the anode) response in yellow for the layout A under the illumination of 660 nm wavelength LED with blinking frequency of (a),(b) 5 Hz, and (c),(d) 50 Hz. Dotted grid lines show a major division of the axis and the corresponding values per divisions are given at the bottom of the plot. (b) and (d) shows the RC time constant of (a) and(c) respectively.

To measure the sensor speed, an LED was placed normal to the sensor 20 cm away and blinked with a known frequency with an Arduino setup. Fig.3.9 shows the oscilloscope trace of the square wave driving the LED (in blue) and the corresponding Astrolabe photodiode (cathode C1 and the anode) response in yellow for the layout A under the illumination of 660 nm wavelength LED. The RC time constant for the combination of TIA and the photodiode is found to be about 1 ms. This is much slower compared to the intrinsic response time of the sensor shown in Fig.3.8. Extrinsic factors such as parasitic capacitance and resistance drain the photocurrent and limit response time.

Having a TIA monolithically integrated on to sensor chip can eliminate the soldered wire connectors to the astrolabe chip and hence reduce the RC time constant by reducing the parasitic capacitance and the resistance which improve the sensor speed.

3.4 Performance Limitations and Improvements for the Next Generation

3.4.1 Signal Deviations from the Linearity

First generation sensor data described in section 3.3.2 shows that S varies with the wavelength of the light source. Variation in Σ with source wavelength obtained for Layout D is shown in Fig.3.10 (a) confirms this phenomenon is valid for a broad spectrum of source wavelengths, including two IR wavelengths. Σ was further analyzed by subtracting the measured value from its line fit for θ_{in} ± 40° and plotting against θ_{in}, see Fig.3.10 (b). For a given layout and source wavelength, a periodic, reproducible, sine like pattern symmetrical around θ_{in}= 0° was observed. Possible reasons for these small deviations from linearity include, edge diffraction from the pinhole aperture and constructive/destructive interference of the reflected light between the Si surface and the underside of the metal box lid.

To understand the dominant cause for the deviations in Σ from linearity, the deviation patterns of Layout B and C which have identical layouts except for use of different anode surface gratings were studied for different source wavelengths. Fig.3.11 (c) shows identical deviation patterns for Layout B and C at 525nm meanwhile in Fig.3.11 (a) and (b) Layout B and C show phase shifted and differently shaped deviation patterns.

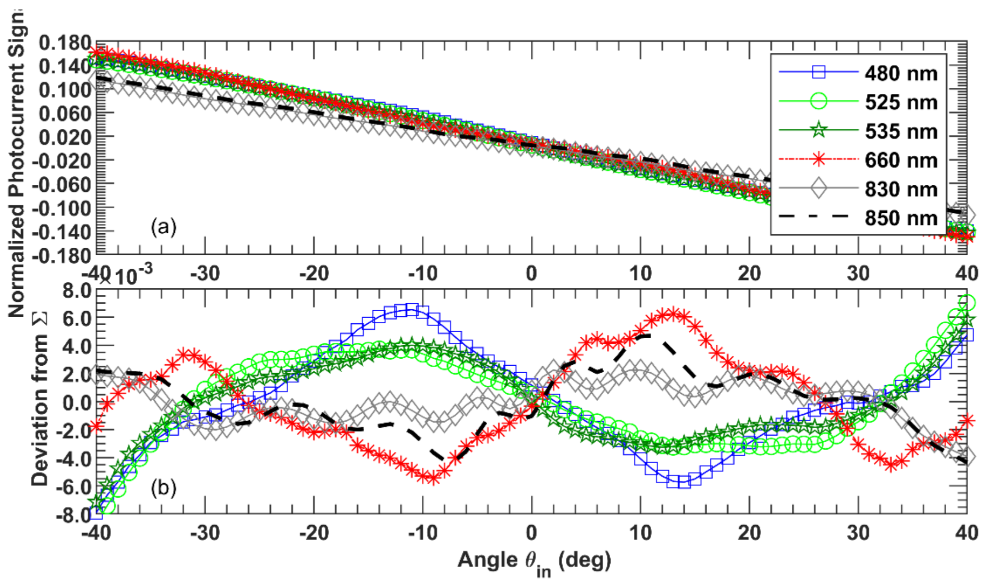

Fig.3.10: (a) Longitudinal arc sweeps of normalized photocurrent signal Σ when the light source wavelength = 480 nm (blue with open squares), 525 nm (green with open circles), 535 nm (dark green with open stars), 660 nm (red with asterisks), 830 nm (grey with open diamonds), and 850 nm (dashed black) of layout D, (b) Corresponding deviation of Σ from the linear fit for θ_{in} ± 40° for each wavelength, with the same line notation.

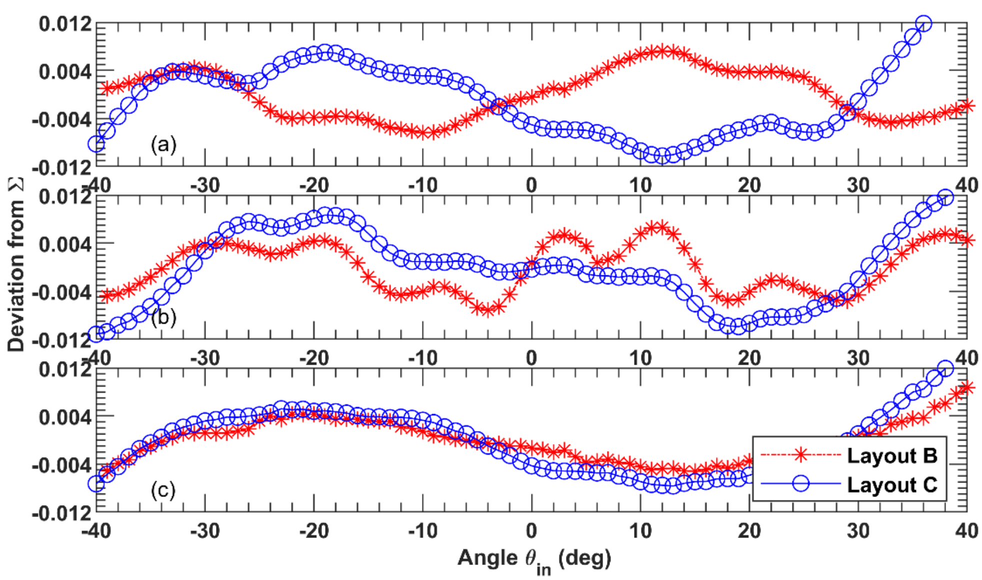

Fig.3.11: Deviation of the Σ with its line fit for θ_{in} ± 40° for Layout B (red with asterisks) and Layout C (blue with open circles) under the illumination of (a) 830 nm (b) 660 nm and (c) 525 nm light sources.

Since the aperture dimensions are the same in both layouts the corresponding edge diffraction is also the same at any given wavelength. Therefore, the different deviation patterns in Fig.3.11 (a) and (b) is a result of surface reflection due to different anode surface gratings. The impact of grating is significant at higher wavelengths. Also, the analysis shows deviations in Σ depends on θ_{in}, hence for high precision applications these repeatable non-linear patterns either need to be corrected for or suppressed.

3.4.2 Signal Enhancement

Table 3.5: Percentage Quantum Efficiency

Layout	%Quantum Efficiency		
	830 nm	660nm	525 nm
A	46	54	49
B	45	48	43
C	45	50	42
D	44	44	44
E	47	47	42
F	22	24	22
G	51	55	49
H	26	29	24

Table 3.5 shows the percentage quantum efficiency relative to the sensor open area for all the layouts at LED wavelengths of 830 nm, 660 nm and 525 nm, all with 0.68 μW incident power on the sensor chip. The results shows ~ 50% Quantum efficiency for the sensors except for the ones with blocking structures. The prototype layouts have 5.25 x 5.25 μm^2 square cathodes extend ~10 μm deep into the Si substrate.

A possible solution to improve the quantum efficiency is to increase the cathode dimensions, although that would involve a trade-off between improving the collection efficiency of the photocurrent and increasing the noise figure as it also increases the contact area to the Si-SiO_2 interface. Reducing the cross-sectional area of the cathode and adding a buried *n*- doped layer to the cathodes could serve the purpose of improving photocurrent collection efficiency without increasing the noise due to the surface dangling bonds at the Si-SiO_2 interface.

3.4.3 Signal Amplification

By analyzing the range of photocurrent signals and their standard deviations obtained under ambient light, dark, and illumination of 830nm, 660 nm, 525nm LEDs for different sensor layouts, an onboard TIA was developed by our collaborators Akash Dey and Dr. Andrew Marshall in the UTD Electrical Engineering Department. Fig.3.12 (a) shows the placement of the amplifier with the Astrolabe sensor and (b) amplifier circuit design for one photodiode of the sensor.

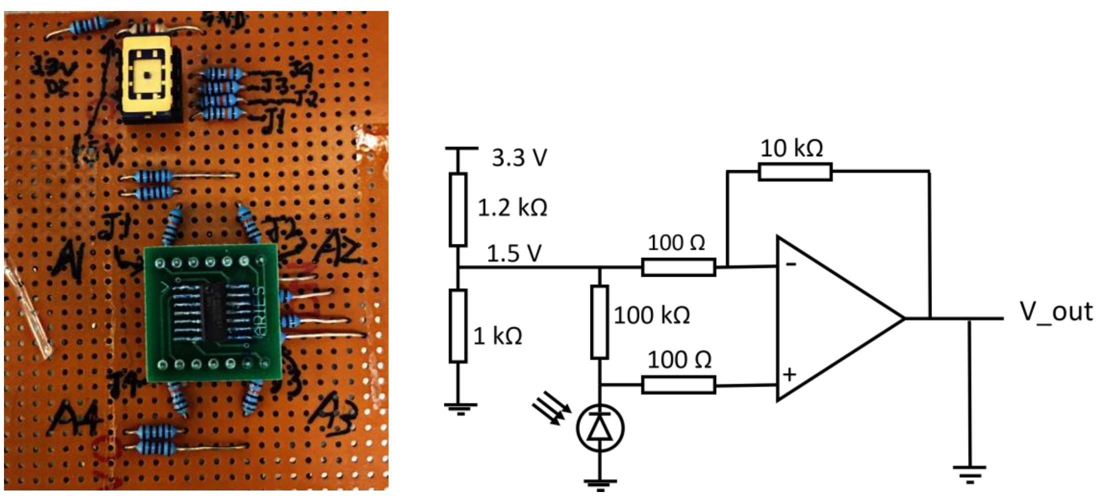

(a) (b)

Fig.3. 12: (a) on- board amplifier placement with the Astrolabe sensor. (b) Amplifier circuit design for one photodiode of the sensor

All the data presented in this Chapter was analyzed for amplified photocurrent signals because we found an 85% improvement of the FoM when using the TIA as opposed to measuring the photocurrent directly, see Fig.3.13. The best sensor candidate in the first generation still needs to improve its FoM by a factor of 10 to obtain the desired accuracy (≤ 1 mm displacement at video rate bandwidths) to track human time-scale motions. Better FoM should be obtainable with a monolithically integrated on-chip TIA, because it reduce the distance between the sensor and the amplifier and eliminate the soldered connections which reduces the parasitic resistance and the capacitance. Parasitic components drain photocurrent and slower the sensor response.

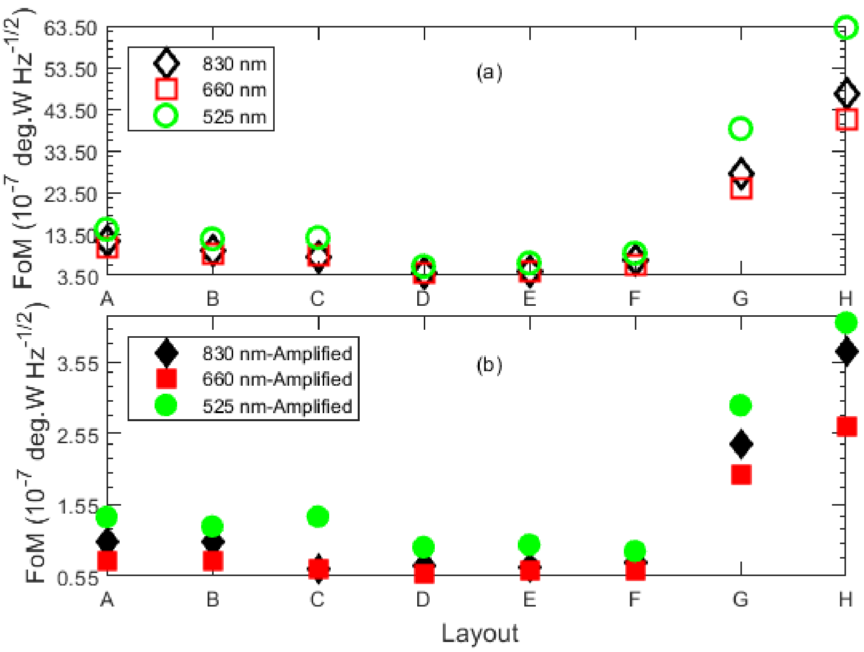

Fig.3. 13: (a) Variations in FoM for the amplified signal under the illumination of 838 nm (open black diamond),660nm (open red squares) and 525nm (open green circles) light sources. (b) Variations in FoM under the illumination of 838 nm (filled black diamond),660nm (filled red squares) and 525nm (filled green circles) light sources.

CHAPTER 4

ADVANCED THEORETICAL MODEL FOR SENSOR OPERATION

Due to the 2-d nature of the first generation Astrolabe sensors, it was not possible to fully interpret the experimental data in the context of the simple 1-d model of Chapter 2. Therefore, a second-generation was made with both explicitly 1-d as well as improved 2-d sensor layouts. Based on the layout geometry and the law of refraction, an advanced theoretical model was derived for the angular displacement θ_{in} of the light source from the photocurrent imbalance, considering the time-dependent diffusion mechanism of the photogenerated carriers in steady state.

4.1 1-d Sensor Theoretical Model

4.1.1 1-d Sensor Total Current and Normalized Photocurrent

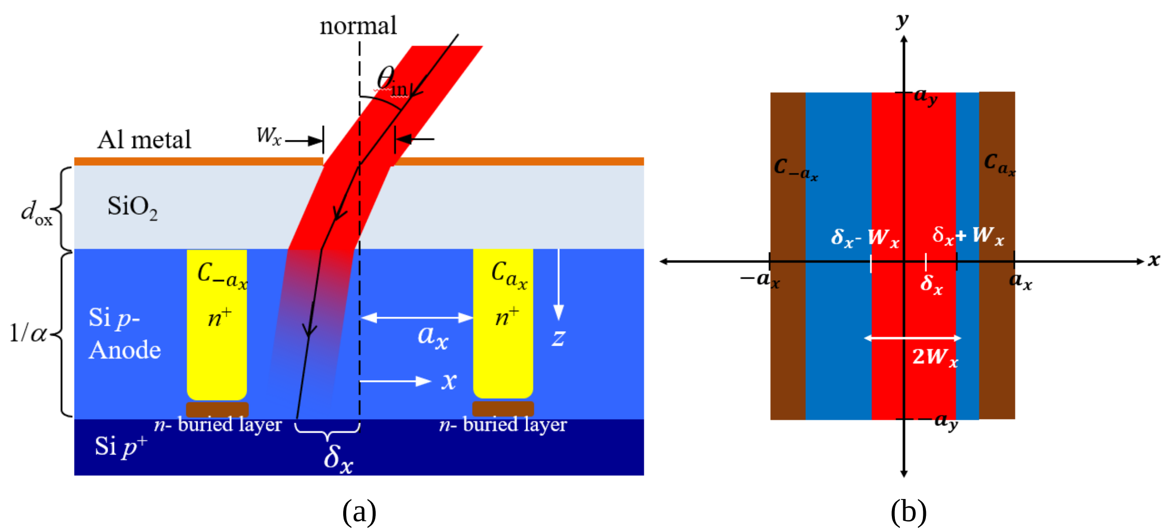

Fig.4.1: Illustration of (a) side (cross-sectional) view and (b) top (plan) view and dimensional parameters of a 1-d sensor. The 1-d sensor contains a slit aperture and cathodes are placed parallel to the edges Red, blue and the yellow/brown areas are illuminated region, anode, and the cathode, respectively. Cathodes C_{a_x} and C_{-a_x} are labeled according to their position. Aperture width is $2W_x$. δ_x is the displacements of the light spot from the center. $2a_y$ is the length of the cathode.

The second generation 1-d sensor contains a slit aperture with two cathodes placed parallel to the aperture edges at a distance a_x from the center as illustrated on Fig.4.1. The anode active area is the area between the two cathodes C_{a_x} and C_{-a_x}. Considering the length of the cathodes $2a_y$, the active area is then $2a_x \times 2a_y$. The aperture is uniformly illuminated resulting in uniform electron hole pair generation rate G. Compared to G the carrier recombination is assumed to be negligible. In the initial iteration of the derivation, the depth dependence of the incident light was not considered. Adding the depth dependence as a correction will be discussed in Chapter 7.

The time dependent diffusion equation can be written as follows [25];

$$\frac{\partial n_{(x,t)}}{\partial t} = D\left(\frac{\delta^2 n_{(x,t)}}{\delta x^2}\right) \tag{4.1}$$

Here, $n_{(x,t)}$ is the photogenerated carrier density along the x direction at time t and D is the diffusion constant. Using separation of variables [25], assume the solution to (4.1) is $n_{(x,t)} = X_{(x)}T_{(t)}$, substituting the solution in (4.1) and dividing both sides by $X_{(x)}T_{(t)}$;

$$\frac{T'_{(t)}}{T_{(t)}} = D\left(\frac{X''_{(x)}}{X_{(x)}}\right) \tag{4.2}$$

Take α, β constants where $\alpha^2 = D\beta^2$

$$\frac{T'_{(t)}}{T_{(t)}} = -\alpha^2 \rightarrow T_{(t)} = \exp(-\alpha^2 t) \tag{4.3.1}$$

$$\frac{X''_{(x)}}{X_{(x)}} = -\beta^2 \rightarrow X_{(x)} = \sin\{\beta(x - x_0)\} \tag{4.3.2}$$

Here x_0 is the boundary of the photogenerated carrier diffusion. Assuming cathodes are perfect recombination centers, using the coordinates in Fig.4.1(b) gives; $n_{(a_x,t)} = 0$ and $n_{(-a_x,t)} = 0$ which leads to $X_{(a_x)} = 0$ and $X_{(-a_x)} = 0$ respectively. Setting the boundary in Eq. (4.3.2) to $x_0 = -a_x$ results in:

$$\beta_{(m)} = \frac{m\pi}{2a_x} \ , \quad {\alpha_{(m)}}^2 = D\left(\frac{\pi m}{2a_x}\right)^2 \qquad\qquad m = 1,2 \ldots . \infty \tag{4.4}$$

With the values of $\beta_{(m)}$ and $\alpha_{(m)}$, (4.3.1) and (4.3.2) can be rewritten as follows for an instantaneous light pulse created at time t_0;

$$T_{(t,m)} = exp\left\{-D\left(\frac{\pi m}{2a_x}\right)^2 (t - t_0)\right\} \tag{4.5.1}$$

$$X_{(x,m)} = \sin\left\{\frac{m\pi}{2a_x}(x + a_x)\right\} \tag{4.5.2}$$

Therefore, summing over all possible values of m, $n_{(x,t)}$ can be written as;

$$n_{(x,t)} = \sum_{m=1}^{\infty} A_m \sin\left\{\frac{m\pi}{2a_x}(x + a_x)\right\} \times exp\left\{-D\left(\frac{\pi m}{2a_x}\right)^2 (t - t_0)\right\} \tag{4.6}$$

With assumption of uniform illumination and negligible recombination, the optical pulse created at time t_0 with photogeneration rate G creates the same amount of electron-hole pairs in the region $\delta_x - W_x < x < \delta_x + W_x$ on the Si substrate. *i.e.* $n_{(x,t=t_0)} = G$. Therefore, at $t = t_0$, A_m in equation (4.6) can be written as follows [25] [26];

$$A_m = G\frac{1}{a_x}\int_{\delta_x - W_x}^{\delta_x + W_x} \sin\left\{\frac{m\pi}{2a_x}(x + a_x)\right\} dx = \left(\frac{-4G}{m\pi}\right)\sin\left\{\frac{m\pi}{2a_x}(\delta_x + a_x)\right\}\sin\left(\frac{m\pi}{2a_x}W_x\right) \tag{4.7}$$

Steady state can be achieved by integrating the optical pulse created at t_0 to infinity

$$\int_{-\infty}^{t} T_{(m,t=t_0)}\, dt_0 = \int_{-\infty}^{t} exp\left\{-D\left(\frac{\pi m}{2a_x}\right)^2 (t - t_0)\right\} dt_0 = \frac{1}{D\left(\frac{\pi m}{2a_x}\right)^2} \tag{4.8}$$

Therefore, from (4.6), (4.7) and (4.8) the photogenerated carrier density at steady state;

$$n_{(x)} = \frac{-16Ga_x{}^2}{D\pi^3}\sum_{m=1}^{\infty}\frac{1}{m^3}\sin\left\{\frac{m\pi}{2a_x}(\delta_x + a_x)\right\}\sin\left(\frac{m\pi}{2a_x}W_x\right)\sin\left\{\frac{m\pi}{2a_x}(x + a_x)\right\} \quad (4.9)$$

The current density at the cathode $C_{a_x} = J_{a_x}$ can be found by Fick's Law of Diffusion [23];

$$J_{a_x} = -D(-q)\frac{dn_{(x)}}{dx}\Big|_{x=a_x}$$

$$= \frac{-8Gqa_x}{\pi^2}\sum_{m=1}^{\infty}\frac{1}{m^2}\sin\left\{\frac{m\pi}{2a_x}(\delta_x + a_x)\right\}\sin\left(\frac{m\pi}{2a_x}W_x\right)\cos(m\pi) \quad (4.10)$$

Where, q is the charge of the photogenerated carriers,

Then by multiplying J_{a_x} by the length of the cathode $2a_y$ the current at the cathode $C_{a_x} = I_{a_x}$;

$$I_{a_x} = \int_{-a_y}^{a_y} J_{a_x}\,dy = \frac{-16Gqa_xa_y}{\pi^2}\sum_{m=1}^{\infty}\frac{1}{m^2}\sin\left\{\frac{m\pi}{2a_x}(\delta_x + a_x)\right\}\sin\left(\frac{m\pi}{2a_x}W_x\right)(-1)^m \quad (4.11.1)$$

Similarly, we can find,

$$I_{-a_x} = \int_{-a_y}^{a_y} J_{-a_x}\,dy = \frac{16Gqa_xa_y}{\pi^2}\sum_{m=1}^{\infty}\frac{1}{m^2}\sin\left\{\frac{m\pi}{2a_x}(\delta_x + a_x)\right\}\sin\left(\frac{m\pi}{2a_x}W_x\right) \quad (4.11.2)$$

Then, the nonzero values of total current and the current imbalance;

$$I_{total} = I_{a_x} + I_{-a_x} = \frac{32Gqa_xa_y}{\pi^2}\sum_{m,odd}^{\infty}\frac{1}{m^2}\sin\left\{\frac{m\pi}{2a_x}(\delta_x + a_x)\right\}\sin\left(\frac{m\pi}{2a_x}W_x\right) \quad (4.12.1)$$

$$I_{a_x} - I_{-a_x} = \frac{-32Gqa_xa_y}{\pi^2}\sum_{m,even}^{\infty}\frac{1}{m^2}\sin\left\{\frac{m\pi}{2a_x}(\delta_x + a_x)\right\}\sin\left(\frac{m\pi}{2a_x}W_x\right) \tag{4.12.2}$$

For the movement of the light spot along the x axis, the normalized photocurrent signal Σ_x;

$$\Sigma_x = \frac{I_{a_x} - I_{-a_x}}{I_{a_x} + I_{-a_x}} = \frac{-\sum_{m,even}^{\infty}\frac{1}{m^2}\sin\left\{\frac{m\pi}{2a_x}(\delta_x + a_x)\right\}\sin\left(\frac{m\pi}{2a_x}W_x\right)}{\sum_{m,odd}^{\infty}\frac{1}{m^2}\sin\left\{\frac{m\pi}{2a_x}(\delta_x + a_x)\right\}\sin\left(\frac{m\pi}{2a_x}W_x\right)} \tag{4.13}$$

The geometrical offset of the actual aperture location is $\delta_x = dtan\theta_{(x)ref}$. $d = d_{ox} + 1/\alpha$ is the distance from the top of the surface to where the carriers are generated as marked in Fig.4.1.(a). d_{ox} is the thickness of the SiO_2 layer and $1/\alpha$ is the penetration in Si for a given incident wavelength.

Considering the refraction occurs at Si-SiO_2 interface the Snell's Law [24] gives; $n_{Si}sin\theta_{(x)ref} = sin\theta_{(x)in}$. Where $\theta_{(x)ref}$ is the reference angle, $\theta_{(x)in}$ is the incidence angle and n_{Si} is the refractive index of the Si substrate for a given incident wavelength.

Therefore;

$$\delta_x = dtan\left\{sin^{-1}\left(\frac{sin\theta_{(x)in}}{n_{Si}}\right)\right\} \tag{4.14}$$

4.1.2 1-d Sensor Response Time

In a similar way described in Chapter 2, the response time can be estimated by finding the storage time of the photodiode. The total photogenerated carrier density in the active area of the sensor is,

$$n_{total} = 2a_y \times \int_{-a_y}^{a_y} n_{(x)}\, dx$$

$$n_{total} = -\frac{128\, G a_y {a_x}^3}{D\pi^4} \sum_{m,odd}^{\infty} \frac{1}{m^4} \sin\left\{\frac{m\pi}{2a_x}(\delta_x + a_x)\right\} \sin\left(\frac{m\pi}{2a_x} W_x\right) \tag{4.15}$$

Therefore, the response time can be found in a similar way as Chapter 2, Eq. (2.11) by replacing the total current with the expression in Eq. (4.13.1).

$$\tau = \left(\frac{4{a_x}^2}{D\pi^2}\right) \frac{\sum_{m,odd}^{\infty} \frac{1}{m^4} \sin\left\{\frac{m\pi}{2a_x}(\delta_x + a_x)\right\} \sin\left(\frac{m\pi}{2a_x} W_x\right)}{\sum_{m,odd}^{\infty} \frac{1}{m^2} \sin\left\{\frac{m\pi}{2a_x}(\delta_x + a_x)\right\} \sin\left(\frac{m\pi}{2a_x} W_x\right)} \tag{4.16}$$

4.2 2-d Sensors

4.2.1 2-d Sensor Total Current and Normalized Photocurrent

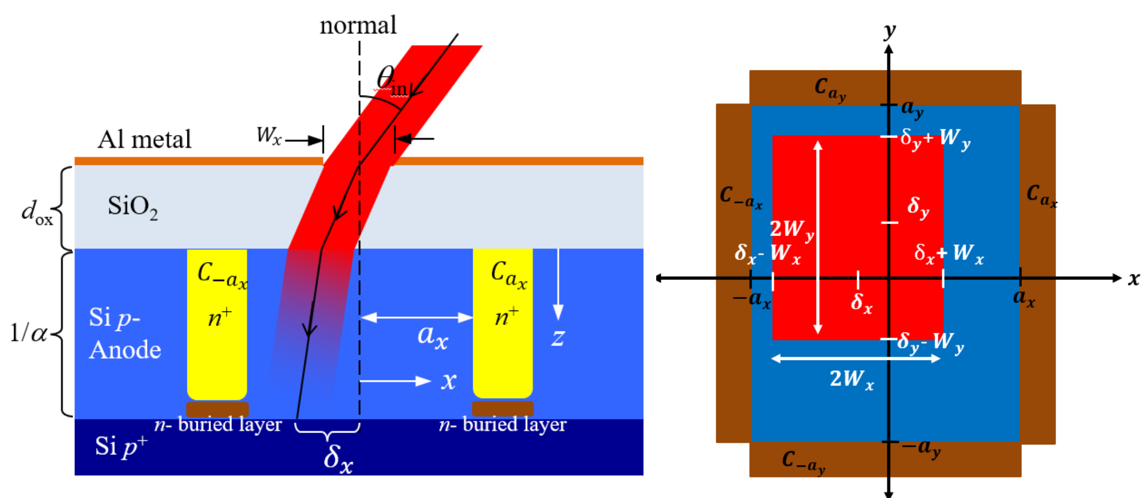

Fig.4.2: Illustration of (a) a side (cross-sectional) view (b) top (plan) view and the dimensional parameters of the 2-d sensor. The 2-d sensor contains a rectangular aperture and cathodes are placed parallel to the edges Red, blue and the yellow/brown areas are illuminated region, anode and the cathode respectively. Cathodes C_{a_x}, C_{-a_x}, C_{a_y} and C_{-a_y} are labeled according to their positions. Aperture width and height are equal to $2W_x$ and $2W_y$ respectively. δ_x and δ_y are displacements of the light spot from the center.

A 2-d model can be derived in a similar way as the 1-d model considering the time dependent 2-d diffusion of the photogenerated carriers. The anode active area for the 2-d sensors is the area between the four cathodes C_{a_x}, C_{-a_x}, C_{a_y}, and C_{-a_y}.The same steps and assumptions were applied in this model as in 1-d. The layout design and the dimensional parameters are shown in Fig.4.2.

Time dependent 2-d Diffusion Equation is [25],

$$\frac{\partial n_{(x,y,t)}}{\partial t} = D\nabla^2 n_{(x,y,t)} = D\left(\frac{\delta^2 n_{(x,y,t)}}{\delta x^2} + \frac{\delta^2 n_{(x,y,t)}}{\delta y^2}\right) \tag{4.17}$$

Using separation of variables [25], assume the solution to (4.17) is $n_{(x,y,t)} = X_{(x)}Y_{(y)}T_{(t)}$. Substituting this in (4.17) and dividing both sides by $X_{(x)}Y_{(y)}T_{(t)}$;

$$\frac{T'_{(t)}}{T_{(t)}} = D\left(\frac{X''_{(x)}}{X_{(x)}} + \frac{Y''_{(y)}}{Y_{(y)}}\right) \tag{4.18}$$

Take α, β, γ to be constants where $\alpha^2 = D(\beta^2 + \gamma^2)$

$$\frac{T'_{(t)}}{T_{(t)}} = -\alpha^2 \rightarrow T_{(t)} = \exp(-\alpha^2 t) \tag{4.19.1}$$

$$\frac{X''_{(x)}}{X_{(x)}} = -\beta^2 \rightarrow X_{(x)} = \sin\{\beta(x - x_0)\} \tag{4.19.2}$$

$$\frac{Y''_{(y)}}{Y_{(y)}} = -\gamma^2 \rightarrow Y_{(y)} = \sin\{\gamma(y - y_0)\} \tag{4.19.3}$$

Assuming cathodes are perfect recombination centers, at the boundaries

$$X_{(a_x)} = X_{(-a_x)} = Y_{(a_y)} = Y_{(-a_y)} = 0$$

As marked in the Fig.(4.2), the boundaries for equation (4.19.2) and (4.19.3) set to $x_0 = -a_x$ and $y_0 = -a_y$ respectively gives;

$$\beta_{(m)} = \frac{m\pi}{2a_x} \qquad m = 1,2 \ldots . \infty \tag{4.20.1}$$

$$\gamma_{(n)} = \frac{n\pi}{2a_y} \qquad n = 1,2 \ldots . \infty \tag{4.20.2}$$

With $\alpha^2 = D(\beta^2 + \gamma^2)$ we have;

$$\alpha_{(m,n)} = D\left(\frac{\pi}{2}\right)^2 \left[\left(\frac{m}{a_x}\right)^2 + \left(\frac{n}{a_y}\right)^2\right] \tag{4.20.3}$$

With the values given in (4.20.1), (4.20.2), and (4.20.3), we can rewrite equation (4.19.1), (4.19.2) and (4.19.3) as follows;

$$T_{(t,m,n)} = exp\left\{-D\left(\frac{\pi}{2}\right)^2 \left[\left(\frac{m}{a_x}\right)^2 + \left(\frac{n}{a_y}\right)^2\right](t - t_0)\right\} \tag{4.21.1}$$

$$X_{(x,m)} = \sin\left\{\frac{m\pi}{2a_x}(x + a_x)\right\} \tag{4.21.2}$$

$$Y_{(y,n)} = \sin\left\{\frac{n\pi}{2a_y}(y + a_y)\right\} \tag{4.21.3}$$

Therefore $n_{(x,y,t)}$ can be written with a constant A_{mn}

$$\begin{aligned} n_{(x,y,t)} = \sum_{m=1}^{\infty}\sum_{n=1}^{\infty} A_{mn} \sin\left\{\frac{m\pi}{2a_x}(x + a_x)\right\}\sin\left\{\frac{n\pi}{2a_y}(y + a_y)\right\} \\ \times exp\left\{-D\left(\frac{\pi}{2}\right)^2 \left[\left(\frac{m}{a_x}\right)^2 + \left(\frac{n}{a_y}\right)^2\right](t - t_0)\right\} \end{aligned} \tag{4.22}$$

In the 2-d model $n_{(x,y,t=t_0)} = G$ in the region $\delta_x - W_x < x < \delta_x$ and $\delta_y - W_y < y < \delta_y + W_y$ Therefore, A_{mn} at $t = t_0$ is:

$$A_{mn} = G\ \frac{1}{a_x}\int_{\delta_x - W_x}^{\delta_x + W_x} \sin\left\{\frac{m\pi}{2a_x}(x + a_x)\right\} dx\ \frac{1}{a_y}\int_{\delta_y - W_y}^{\delta_y + W_y} \sin\left\{\frac{n\pi}{2a_y}(x + a_y)\right\} dy$$

$$= \left(\frac{16G}{mn\pi^2}\right)\sin\left\{\frac{m\pi}{2a_x}(\delta_x + a_x)\right\}\sin\left(\frac{m\pi}{2a_x}W_x\right)\sin\left\{\frac{n\pi}{2a_y}(\delta_y + a_y)\right\}\sin\left(\frac{n\pi}{2a_y}W_y\right) \qquad (4.23)$$

For the 2-d layout, the steady state is obtained from;

$$\int_{-\infty}^{t} T_{(m,n,t=t_0)}\, dt_0 = \frac{1}{D\left(\frac{\pi}{2}\right)^2\left[\left(\frac{m}{a_x}\right)^2 + \left(\frac{n}{a_y}\right)^2\right]} \qquad (4.24)$$

Therefore, the carrier density at the coordinate (x, y) by (4.22), (4.23) and (4.24)

$$n_{(x,y)} = C\sum_{m=1}^{\infty}\sum_{n=1}^{\infty} C_{mn}C_mC_n \sin\left\{\frac{m\pi}{2a_x}(x + a_x)\right\}\sin\left\{\frac{n\pi}{2a_y}(y + a_y)\right\} \qquad (4.25)$$

Where;

$$C = \frac{64G}{D\pi^4}$$

$$C_{mn} = \frac{1}{mn\left[\left(\frac{m}{a_x}\right)^2 + \left(\frac{n}{a_y}\right)^2\right]}$$

$$C_m = \sin\left\{\frac{m\pi}{2a_x}(\delta_x + a_x)\right\}\sin\left(\frac{m\pi}{2a_x}W_x\right)$$

$$C_n = \sin\left\{\frac{n\pi}{2a_y}(\delta_y + a_y)\right\}\sin\left(\frac{n\pi}{2a_y}W_y\right) \qquad (4.25.1)$$

In a similar way as in 1-d model derivation, for a horizontal movement of the light spot, the currents read at the cathodes C_{a_x} and C_{-a_x} can be written as;

$$I_{a_x} = DqC \sum_{m=1}^{\infty} \sum_{n=1}^{\infty} C_{mn} C_m C_n \left(\frac{m}{n}\right) \left(\frac{a_x}{a_y}\right) (-1)^{\mathrm{m}} [1 - (-1)^n] \tag{4.26.1}$$

$$I_{-a_x} = DqC \sum_{m=1}^{\infty} \sum_{n=1}^{\infty} -C_{mn} C_m C_n \left(\frac{m}{n}\right) \left(\frac{a_x}{a_y}\right) [1 - (-1)^n] \tag{4.26.2}$$

Therefore, the normalized photocurrent signal for the horizontal movement of the light spot is;

$$\Sigma_x = \frac{I_{a_x} - I_{-a_x}}{I_{a_x} + I_{-a_x}} = \frac{\sum_{m,even}^{\infty} \sum_{n,odd}^{\infty} C_{mn} C_m C_n \left(\frac{m}{n}\right)}{\sum_{m,odd}^{\infty} \sum_{n,odd}^{\infty} -C_{mn} C_m C_n \left(\frac{m}{n}\right)} \tag{4.27}$$

Similarly, for the vertical movement of the light spot the currents read at the cathodes C_{a_y} and C_{-a_y} can be written as;

$$I_{a_y} = DqC \sum_{m=1}^{\infty} \sum_{n=1}^{\infty} C_{mn} C_m C_n \left(\frac{n}{m}\right) \left(\frac{a_x}{a_y}\right) (-1)^n [1 - (-1)^m] \tag{4.28.1}$$

$$I_{-a_y} = DqC \sum_{m=1}^{\infty} \sum_{n=1}^{\infty} C_{mn} C_m C_n \left(\frac{n}{m}\right) \left(\frac{a_x}{a_y}\right) [1 - (-1)^m] \tag{4.28.2}$$

The normalized photocurrent signal Σ_y;

$$\Sigma_y = \frac{I_{a_y} - I_{-a_y}}{I_{a_y} + I_{-a_y}} = \frac{\sum_{m,odd}^{\infty} \sum_{n,even}^{\infty} C_{mn} C_m C_n \left(\frac{n}{m}\right)}{\sum_{m,odd}^{\infty} \sum_{n,odd}^{\infty} -C_{mn} C_m C_n \left(\frac{n}{m}\right)} \tag{4.29}$$

The total current of the 2-d sensor is;

$$I_{total} = I_{a_x} + I_{-a_x} + I_{a_y} + I_{-a_y}$$

$$= DqCa_x a_y \sum_{m=1}^{\infty} \sum_{n=1}^{\infty} \left(\frac{1}{mn}\right)^2 C_m C_n [(-1)^m - 1][1 - (-1)^n] \tag{4.30}$$

For the horizontal movement of the light spot, the geometrical offset of the illuminated region on the y axis; δ_y is a constant. δ_x is the same as derived in 1-d model (equation (4.14)). Similarly, for the vertical movement of the light spot δ_x is a constant and δ_y can be written as;

$$\delta_y = dtan\left\{sin^{-1}\left(\frac{sin\theta_{(y)in}}{n_{Si}}\right)\right\} \tag{4.31}$$

For both 1-d and 2-d model, the generation rate of the photocarriers is given by equation (4.16).

4.2.2 2-d Sensor Response Time

Following the similar steps as in Sec. 4.1.2. The total photo generated carrier density in the active area of the sensor can be found by integrating $n_{(x,y)}$ over the boundaries of the active region.,

$$n_{total} = \left(\frac{-4Ca_xa_y}{\pi^2}\right)\sum_{m=1}^{\infty}\sum_{n=1}^{\infty}\left(\frac{1}{mn}\right)C_{mn}C_mC_n\,[(-1)^m - 1][1-(-1)^n] \tag{4.32}$$

Taking the total current in Eq. (4.30), the 2-d sensor response time can be written as,

$$\tau = \left(\frac{4}{D\pi^2}\right)\frac{\sum_{m,odd}^{\infty}\sum_{n,odd}^{\infty}\left(\frac{1}{mn}\right)C_{mn}C_mC_n}{\sum_{m,odd}^{\infty}\sum_{n,odd}^{\infty}\left(\frac{1}{mn}\right)^2 C_mC_n} \tag{4.33}$$

C_m, C_n and , C_{mn} are the same as in Eq. (4.25.1)

The experimental data of the first generation prototype sensors given in Chapter 3 showed an inverse relation between the aperture open area and the normalized photocurrent. However, we could not explain the underlying behavior because the simple theoretical model developed in Chapter 2 does not contain any term related to the aperture area.

The normalized photocurrent and θ_{in} relation in the advanced theoretical model for 1-d sensor and 2-d sensor contains an explicit aperture width term and therefore the aperture width dependency on sensitivity S can be investigated. Due to the Fourier series in the numerator and denominator of the above derived equations, the relation between layout parameters and the sensor characteristics is not immediately obvious. These models can be simplified further by analyzing the experimental results of the sensor which will be discussed on Chapter 5. Further, the theoretical model can be modified by adding physical correction terms such as carrier loss due to recombination, depth dependence of the incident light, boundary of the cathodes etc. which will be discussed in detail in Chapter 7.

CHAPTER 5

ASTROLABE SENSOR SECOND GENERATION

Based on the results obtained from the prototype first generation sensors as shown in Chapter 3, we designed an advanced second generation of the Astrolabe sensor. Layout variations were made to further analyze the behavior of geometrical parameters in both 1-d and 2-d sensors characteristics, to find the physical quantities that could be used to improve the sensor operating model, and to identify the layout features that could improve the sensor performance for practical applications. This chapter contains the layout design and construction of the second generation sensors and summarizes the results and findings we obtained.

5.1 Sensor Layout Design and Construction

Second generation layouts were designed on Cadence with the aid of SKILL programming and fabricated on a commercial 0.18 µm technology node CMOS process line at Texas Instruments. For each sensor, the anode consisted of a 20 µm thick *p* layer (10^{15} to 10^{17} cm^{-3}) above a deep p^+ layer (> 10^{18} cm^{-3}) on a *p*-type Si wafer. A d_{ox} = 10 µm layer of SiO_2 on the Si surface was grown to support an aluminum metal layer that formed the camera box. The aperture in the Al metal is centered among cathodes.

The second generation includes both 1-d and 2-d sensor layout designs to help us understand the difference between and limits of validity of the 1-d and 2-d theoretical models. 1-d sensors consist of slit apertures with two linear cathodes placed on either side of the slit, meanwhile 2-d sensors consist of square apertures with four line-cathodes placed at north south east and west.

Fig.5.1 (a) and (b) shows plan view designs (to scale) of 1-d and 2-d sensors respectively. The blue shading, covering most of the cell represents the Al box layer on the upper surface. The center aperture opens onto the Si anode surface, colored in black with blue-green p signs. The photo-cathodes (under the aluminum box layer) are colored in a white brick pattern.

The photo-cathodes were formed by ion implanting n^+ wells (~ 10^{17} cm^{-3}) to a depth of ~ 10 µm into the anode.

Unlike the first generation which used 5.25 x 5.25 μm^2 square cathodes, the second generation has 2 x 4 μm^2 square cathodes connected to an n - buried layer. Fig.5.2 shows the plan view (to scale) and the 3-d illustration of the n^+ and n - buried layer.

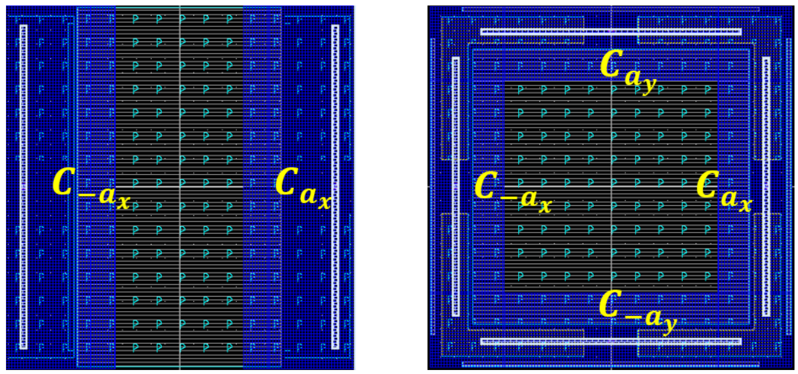

(a) (b)

Fig.5.1: (a) 1-d sensor (b) 2-d sensor plan view of the unit cell design layouts (to scale). Blue shaded regions represent the top Al metal. Aperture openings are black with blue p signs, which indicates the anode surface. Cathodes are the white bars placed either side of the aperture named C_{a_x}, C_{-a_x}, C_{a_y} and C_{-a_y} depending on their position.

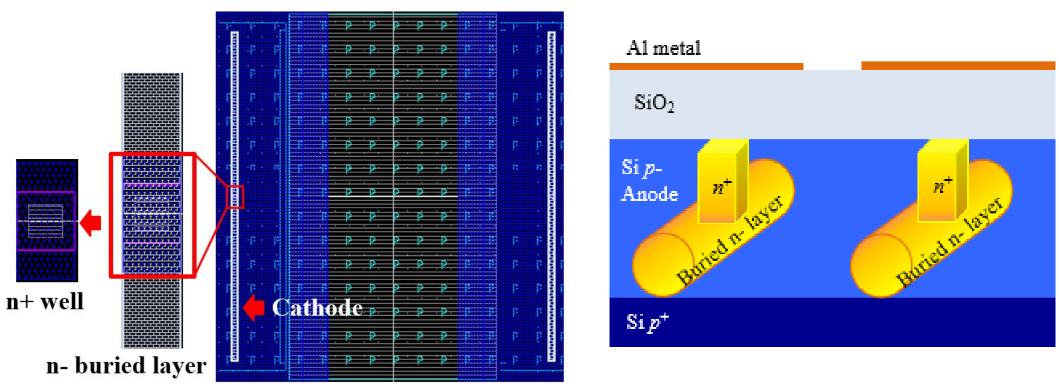

(a) (b)

Fig.5.2: (a) plan view of the $n+$ well and n-buried layer relative to the sensor layout (to scale). (b) A 3-d schematic illustration (not to scale) of second-generation cathode, with n^+ well connected to a n-layer buried in anode, close to the depth of photocarrier generation. Buried layer is parallel to the aperture extended all the way to the edges unless limited by fabrication processes rules.

This new cathode configuration was made to reduce the noise density as it reduces the cross section area at the Si/SiO_2 interface, where dangling bonds affect the mobility of carriers and create fluctuations in carrier density. Normalized photocurrent signal vs angle plots obtained from the first generation prototype sensors showed a saturation when the light spot shines onto a cathode. By reducing the width of the cathode, an extended field-of view is expected. The prototype sensors showed 50% quantum efficiency for 830 nm, 660 nm and 525 nm incident wavelengths. Therefore, to improve the collection efficiency of photogenerated carriers, the length of the cathode was increased by adding an *n*- buried layer which is parallel to the aperture and extends all the way to the edges unless limited by fabrication rules. Variations were made reducing the length of the *n*-buried layer and reducing the contact area of the n^+ wells with the SiO_2 layer to test the expected behavior.

Second generation sensor layouts have been designed that contain 100 µm×100 µm and 125 µm×125 µm unit cells, placed on a 1 mm × 1mm sensor area allowing the space to have 10×10 and 8×8 arrays of identical unit cells respectively. All the C_{a_x} cathodes are connected in parallel to a common C_{a_x} bonding pad to output a total current I_{a_x} and similarly for , C_{-a_x}, $C_{a_y}$and $C_{-a_y}$and their currents I_{-a_x}, $I_{a_y}$and I_{-a_y}. Each chip had a common anode bonding pad used as the circuit ground.

As shown in Chapter 3, the first generation sensors shows 85% improvement in the Angular Noise Density with a TIA on board. With an on -board TIA the best sensor candidate in the first-generation needed to improve its FoM by a factor of 10 to meet a desired accuracy criterion (≤ 1 mm displacement resolution at distance of 1 m with video rate bandwidth) to track human time-scale motions. Also, the sensors connected to a TIA mounted on a board had 1 ms RC time constant, which limits the speed of the sensor. Based on the results of the first generation sensors an integrated on -chip TIA was designed in the same processing node used to design the Astrolabe sensors and integrated into ten basic sensor layouts by our collaborators Akash Dey and Dr. Andrew Marshall in the UTD Electrical Engineering Department.

The second generation sensor has a 1.50 mm ×1.20 mm total area with 1.00 mm×1.00 mm sensing area which contains the array of sensor unit cells.

The on-chip TIA is monolithically integrated on-chip and occupies a footpring of 0.23 mm× 0.90 mm, situated 0.05 mm to the right of the sensing area. The amplifier area is covered by the same Al metal used to make the camera box of the sensor and both the amplifier and the sensor area have an *n*- buried layer boundary to absorb any stray electrons. Excluding the bonding pads, the rest of the sensor is covered with an Al alloy material (shaded in red in Fig.5.3) to avoid any photo carrier generation other than the sensing area. Each chip was mounted in an uncovered 20-pin dual inline package (DIP) (Fig.5.5 (b)).

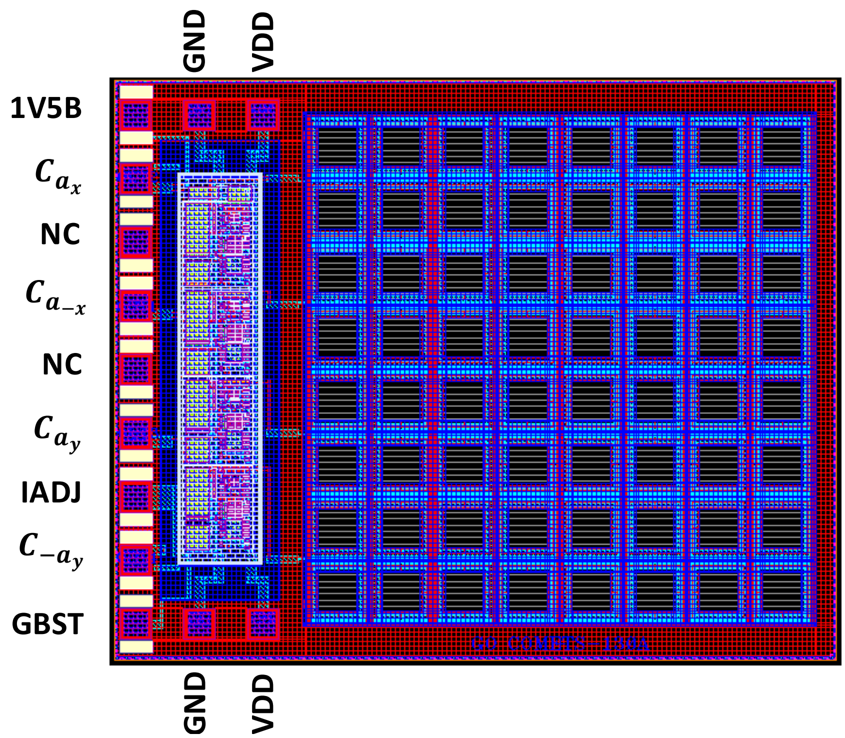

Fig.5.3: Layout view (to scale) of the Astrolabe sensor with bond pad identities. The sensor has a 1.50 mm ×1.20 mm total area with 1.00 mm×1.00 mm sensing area which contains the array of sensor unit cells. Here a TIA is integrated with the sensor and occupies a 0.23 mm× 0.90 mm area, situated 0.05mm right to the sensing area. The amplifier area is covered by the same Al metal used to make the camera box of the sensor (shaded in blue) and both the amplifier and the sensor area have an *n*- buried layer boundary to absorb any stray electrons. Except the bonding pads, the rest of the sensor is covered with an Al alloy (shaded in red) to avoid any photo carrier generation other than the sensing area.

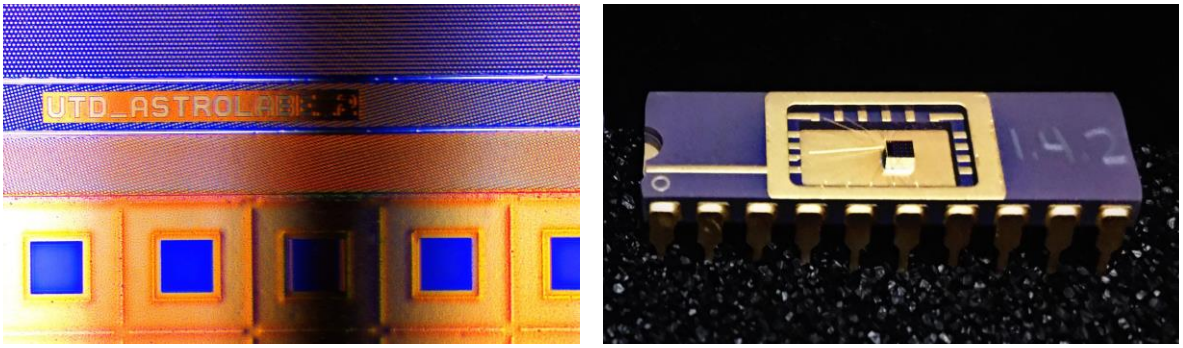

(a) (b)

Fig.5.4: (a) Microscopic image showing the unit cells of the actual sensor. (b) sensor wire bonded to a 20 pin dual in line package.

5.2 Sensor Performance

This section presents the unamplified experimental data obtained from 1-d and 2-d sensors. Due to the large number of sensor variations, TIA mounted on a board was eliminated in the preliminary study of the sensor characteristics. Goal is to find the optimal sensor based on the intrinsic characteristics so that one can design an on board or on chip amplifier specific to the sensor that could improve the sensor performance for a given application. Experimental values are compared with the advanced theoretical model. To understand the device physics of the sensors, a half pitch of the 1-d sensor unit cell was simulated using Synopsys TSuprem [27] and Medici [28] Technology Computer Aided Design (TCAD) for all the sensor layout variations. In the simulations, the same layout parameters were used as the actual fabrication process. The optical simulations of the devices were done with our collaborator at Texas Instruments, Dr. Hal Edwards.

5.2.1 1-d Sensors

Since the relation of percentage open area with sensitivity *S* is unclear in the tested layouts of the first generation sensors, five variations of percentage open area (9%, 16%, 25%, 36%, 49%) were designed in the new sensor layouts.

In the theoretical model the other parameter that affects the sensor sensitivity is the cathode separation. Therefore, two cathode separation variations were made for the sensor layouts with 16% open area and 25% open area. Table 5.1 contains the 1-d sensor layouts and the parameters.

Table 5.1: 1-d sensor layout parameters

Layout Name	$2a_x$ (µm)	$2W_x$ (µm)	W_x/a_x	% Open Area
D00	107	11.25	0.11	9
D10	107	20.00	0.19	16
D15	79.5	20.00	0.25	16
D20	107	31.25	0.29	25
D25	79.5	31.25	0.39	25
D30	107	45.0	0.42	36
D40	107	61.25	0.57	49

5.2.1.1 Total Current and Quantum Efficiency

Fig.5.5 shows the angular response of the total current, I_{total} of the layout D00 for -80 ° < θ_{in} < 80 ° obtained from 1.) the TCAD simulations, 2.) the 1-d advanced theoretical model of Chapter 4, 3) the measured experimental data under illumination of (a) 830 nm, (b) 660 nm and (c) 525 nm wavelengths. In the TCAD simulations photocarrier generations at a 11.25 µm depth from the top of the Al box was considered and the same depth (d in Eq. (4.15)) was used on the 1-d theoretical model calculations to match with the TCAD data. Refractive index of the Si, n_{Si} in Eq. (4.15) was taken as 3.60, 3.80, and 4.15 for 830nm, 660 nm and 525 nm incident wavelengths respectively [20]. The experimental data were collected using the same laboratory conditions described in Sec. 3.2 with the same measurement setup. Due to the large number of sensor variations, TIA mounted on a board was removed to in the preliminary study of the sensor characteristics. One can design an amplifier mounted on a board with a specific gain based on the intrinsic characteristics of the sensor. The experimental value for the photogeneration rate of the light source, G in Eq. (4.12.1) can be estimated by,

$$G = \frac{P_{in} cos\theta_{in}}{\pi r^2}\left(\frac{\lambda}{hc}\right) \tag{5.1}$$

Here P_{in} is the power for a normal incidence read by a detector with a aperture radius $r =$ 4.75 mm, which was kept at 250 µW for all three measurement wavelengths. h *is the* Plank's constant, c is the Speed of light and λ is the wavelength of the incident light. The summation of the Fourier series in theoretical model (Eq.4.12) was carried out from m = 1 to 100.

Fig.5.5 shows a good agreement between TCAD and experimental values of I_{total} for 660 nm incidence, for incident angles -80 ° < θ_{in} -80 °. The maximum values of the I_{total} obtained for different layouts are listed on Table 5.2.

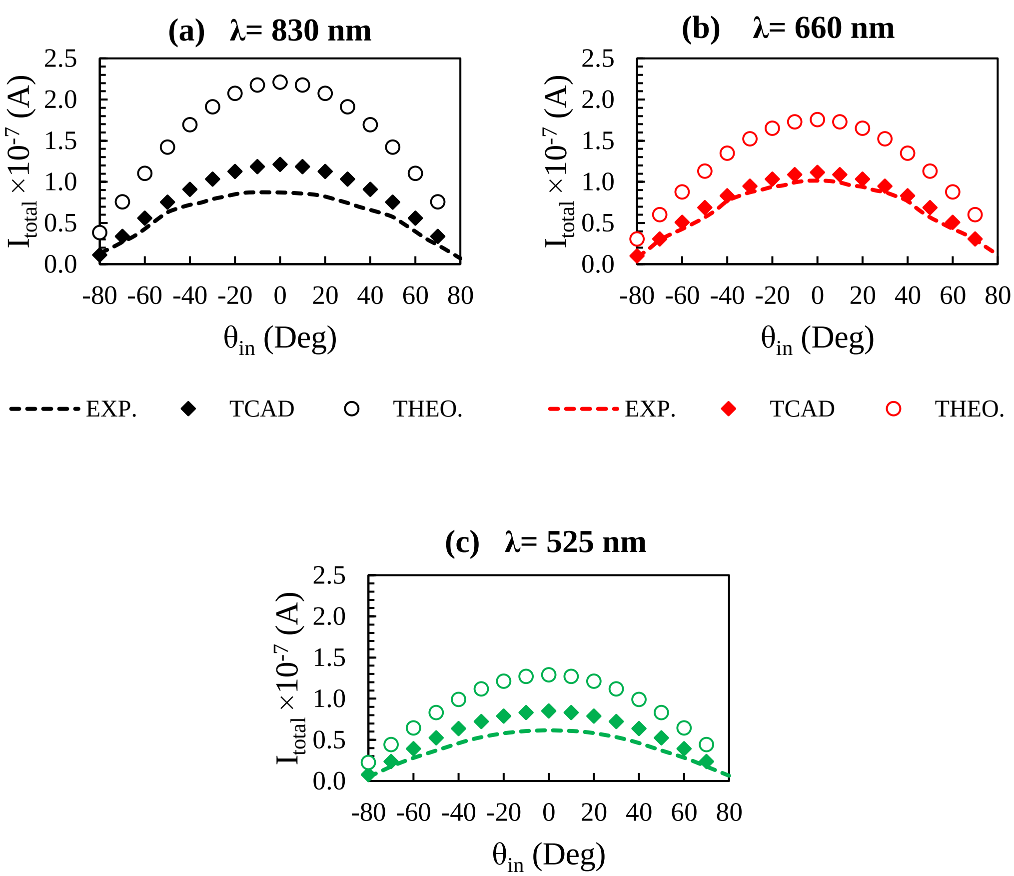

Fig.5.5: Theoretical, TCAD and experimental angular response of the total current, I_{total} of the layout D00 for -80 ° < θ_{in} < 80 ° under the illumination of (a) 830 nm (b) 660 nm and (c) 525 nm incident wavelengths.

The layout parameters used for the TCAD simulations were the same parameters used in the actual fabrication process and hence the experimental results are close to the values obtained from TCAD simulations. More realistic TCAD sensor models can account for different aspects of the device physics of the sensors, including factors such as reflection effects, carrier loss due to recombination and the true boundary of the cathode due to the *p-n* junction depletion region. These factors can be added as a correction factors to the theoretical model, which will be discussed in detail in Chapter 7. Since we assumed one photon creates one electron-hole pair in the theoretical model, the resulting values show higher I_{total} .

Table 5.2: Theoretical, TCAD and Experimental values of the maximum total current for 830 nm IR, 660 nm red and 525 nm green illumination

Layout Name	Maximum I_{total} (nA)								
	Theoretical			TCAD			Experimental		
	IR	Red	Green	IR	Red	Green	IR	Red	Green
D00	221	176	129	121	111	85	87	101	62
D10	393	312	229	215	198	151	150	180	111
D15	393	312	229	230	211	161	183	205	127
D20	613	488	358	337	310	236	265	269	181
D25	614	488	358	361	330	252	280	314	195
D30	883	702	516	488	448	342	375	417	261
D40	1202	956	702	670	616	470	513	564	333

The Quantum efficiency, the ratio between experimental and theoretical value of I_{total} is about 50%, 60% and 43% for λ=525 nm, λ=660 nm and λ=830 nm respectively. 525 nm wavelength has 1.27 µm absorption depth in Si [20] which is closer to the Si-SiO_2 interface with dangling bonds. The dangling bonds capture and emit photogenerated carriers and hence decrease their mobility [29] therefore, the number of electrons that reach to the cathodes will be reduced resulting in lower quantum efficiency. The *n*- buried layer is fabricated about 1.25 µm deep into the Si and unable to capture effectively the carriers generated by 830 nm wavelength, which has about a 15 µm absorption depth [20], and this also lowers the quantum efficiency at the longer wavelength. From a fabrication standpoint near 100% quantum efficiency is expected for 660 nm wavelength as it has a 3.88 µm absorption depth. This will be reduced by reflection losses.

Fresnel calculations estimate about 30% of incident power is lost due to multiple reflections at the SiO_2-air and SiO_2-Si interfaces, which could be reduced by antireflective coatings or gratings in future designs.

5.2.1.2 Angular Sensitivity

Angular Sensitivity, S is the proportionality constant of the relation between normalized photo current signal, Σ_x and θ_{in} as defined on Sec. 3.3.2. The experimental and TCAD S values were found by plotting the normalized photo current of the two cathodes against the θ_{in} , for -40° < θ_{in}< 40°. Similarly, theoretical S was found for -40° < θ_{in}< 40° by using the expression in Eq.(3.13) derived in the advanced 1-d theoretical model with the same d and n_{Si} values used to calculate I_{total} in Sec.5.2.1.1.

Table 5.3: Theoretical, TCAD and Experimental values of the Sensitivity for different sensor layouts for 830 nm IR, 660 nm red and 525 nm green LED sources

Layout Name	Sensitivity (deg^{-1})								
	Theoretical			TCAD			Experimental		
	IR	Red	Green	IR	Red	Green	IR	Red	Green
D00	0.0010	0.0009	0.0008	0.0022	0.0016	0.0014	0.0016	0.0012	0.0011
D10	0.0010	0.0009	0.0008	0.0022	0.0016	0.0014	0.0017	0.0013	0.0012
D15	0.0013	0.0012	0.0011	0.0028	0.0021	0.0018	0.0024	0.0018	0.0015
D20	0.0010	0.0009	0.0008	0.0022	0.0016	0.0014	0.0018	0.0013	0.0011
D25	0.0013	0.0012	0.0011	0.0028	0.0021	0.0018	0.0025	0.0018	0.0016
D30	0.0010	0.0009	0.0008	0.0022	0.0016	0.0014	0.0019	0.0013	0.0012
D40	0.0010	0.0009	0.0008	0.0022	0.0017	0.0014	0.0019	0.0013	0.0011

Due to the lack of parameters, the simple1-d theoretical model of Chapter 2 did not explain the aperture area dependence in S shown by the prototype sensors. The advanced theoretical model has an aperture width term inside a Fourier series. However, the calculated values of S for five different aperture widths show the impact of the aperture width is negligible, which is confirmed by the TCAD simulations and experimental data obtained for three different wavelengths (Table 5.3).

Further, the theoretical, TCAD and experimental values show that *S* is inversely proportional to cathode separation $2a_x$. Experimental data obtained for 660 nm incident wavelength shows good agreement with the theoretical and TCAD models, meanwhile 830 nm and 525 nm incidence show some inconsistency due to the low levels of photocurrents.

Theoretical, TCAD and experimental data shows very good match. TCAD gives 30% higher *S* compared to the experimental values and theoretical values are 30% lower compared to the experimental values. Photocurrents from the TCAD simulations were collected at a 11.25 μm depth from the top of the Al box assuming the *n*- buried layer efficiently collects all the carriers. This could be a reason TCAD gives slightly higher *S*. The theoretical model does not consider the depth dependence of the incident light, reflection effects, and carrier loss due to recombination resulting slightly lower *S* values. However, the parameters responsible for the discrepancy in the results is not obvious since we are analyzing normalized photocurrent to get the *S*.

Table 5.4: Sensitivity calculated from simple theoretical model

Layout Name	Sensitivity (deg^{-1})		
	IR	Red	Green
D00	0.0010	0.0010	0.0009
D10	0.0010	0.0010	0.0009
D15	0.0014	0.0013	0.0012
D20	0.0010	0.0010	0.0009
D25	0.0014	0.0013	0.0012
D30	0.0010	0.0010	0.0009
D40	0.0010	0.0010	0.0009

Further, *S* values calculated from the simple theoretical model at a depth of 11.25 μm agree very well with the values calculated from the advanced theoretical model (Table 5.4) and follow the trend of both experimental and TCAD data. The width dependency shown in the prototype sensors could be due to the combined 1-d and 2-d behavior of the '+' shape aperture.

Therefore, the simple model can be used to estimate the characteristics of 1-d sensors and the Fourier series in advanced theoretical model can be approximated to,

$$\frac{\delta_x}{2a_x} \sim \frac{-\sum_{m,even}^{\infty} \frac{1}{m^2} \sin\left\{\frac{m\pi}{2a_x}(\delta_x + a_x)\right\} \sin\left(\frac{m\pi}{2a_x} W_x\right)}{\sum_{m,odd}^{\infty} \frac{1}{m^2} \sin\left\{\frac{m\pi}{2a_x}(\delta_x + a_x)\right\} \sin\left(\frac{m\pi}{2a_x} W_x\right)} \tag{5.2}$$

The *S* values obtained from the first generation are relatively high with the best *S*=0.0131 deg $^{-1}$ for 660 nm incident wavelength. Layout D25 and Layout B with close aspect ratios (W_x/a_x) shows good agreement for 830 nm illumination and Layout B has four times higher *S* for visible wavelengths. However, the comparison between two generations is not completely fair due to the highly varied layout parameters including unit cell dimensions, aperture shape and cathode modifications.

5.2.1.3 Angular Noise Density

The angular noise density, $\eta = \sigma\tau^{1/2}/S$ where σ and τ are the standard deviation of Σ and the measurement integration time respectively. The experimental data were collected in the standard conditions described in Sec. 3.2 without any signal amplification. Table 5.5 summarizes the η values calculated for three different incident wavelengths. Number of photogenerated carriers are proportional to the sensor open area and hence η decreases with increasing sensor open area, which is confirmed by the quadratic relation of σ with the sensor open area for all three tested wavelengths as shown in Fig.5.6. Also, η increases approximately 30% when the cathode separation is doubled. As expected, 525 nm illumination results in higher η due to the lower quantum efficiency due to scattering from interface dangling bonds. σ is low for 660nm light source (Fig .5.6) as it has the highest tested quantum efficiency. However, the η is higher compared with 830 nm illumination due to the lower *S*.

Layout D with 42% open area in the first generation shows the lowest η, the best reported value without any signal amplification is 0.510 deg/√Hz under the illumination of 660 nm wavelength LED. Layout D40 with 49% open area and D25 with 25% open area with closer cathodes shows the lowest η for λ=830 nm in the second generation 1-d sensors, which are approximately three times lower than the lowest η in the first generation (Table 5.5).

Table 5.5: Angular Noise Density

Layout Name	Noise Density (deg/√Hz)		
	IR	Red	Green
D00	0.587	0.686	1.160
D10	0.333	0.405	0.691
D15	0.235	0.271	0.540
D20	0.218	0.305	0.610
D25	0.195	0.211	0.345
D30	0.218	0.267	0.420
D40	0.184	0.224	0.314

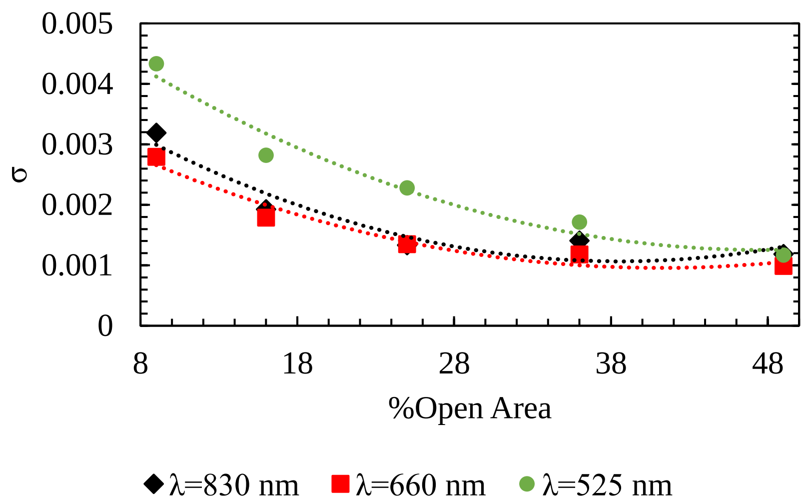

Fig.5.6: The variation of standard deviation of the normalized photocurrent, σ with the open area of 1-d sensors for 830 nm, 660 nm and 525 nm light sources.

5.2.1.4 Figure of Merit

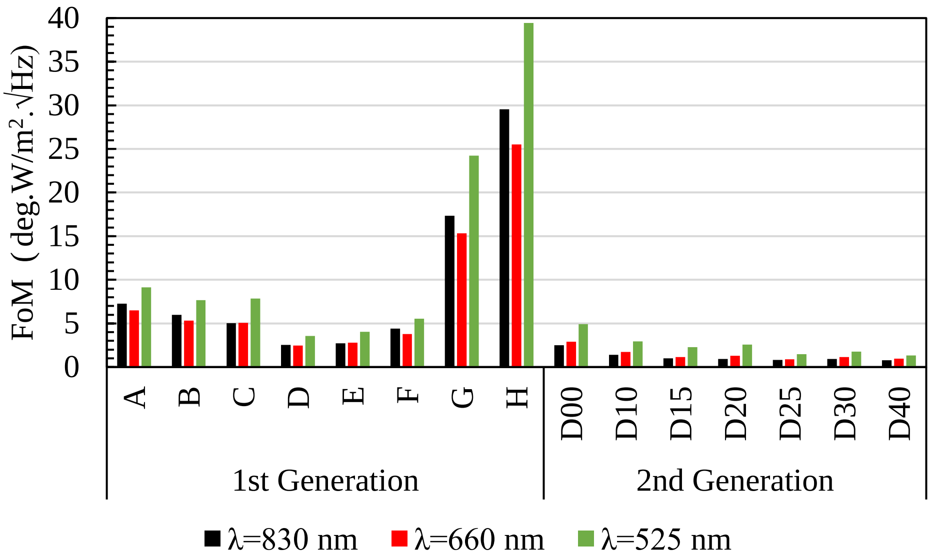

Fig.5.7: Sensor layouts in first generation and second generation and their FoM for λ=830 nm, 660 nm and 525 nm.

The second generation sensors have relatively large sensing area, 1000×1000 μm^2 compared to that of the first generations 400×400 μm^2 sensing area. For a fair comparison, incident power density was considered instead of incident power. Smallest FoM shows the best performance. Fig. 5.8 compares the FoM of the two sensor generations obtained for the unamplified signal under the standard measurement conditions, 21.7 ms measurement band width and a steady state light source with 0.13 μWμm^{-2} incident power. In both generations, FoM decreases with the increasing open area and reduced cathode separation of the sensor. The best FoM in second generation is three times lower than that of first generation due to the reduction in η, without amplification.

5.2.2 2-d Sensors

In order to compare the sensor performance with the 1-d sensors, the same five variations of percentage open area were designed in the 2-d sensor layouts keeping the cathode separation the same as 1-d. Also, the same cathode separation variations were made for the sensor layouts with 16% open area and 25% open area. Table 5.6 contains the 2-d sensor layouts and the parameters.

Table 5.6: 2-d sensor layouts and parameters

Layout Name	$2a_x$ (µm)	$2W_x$ (µm)	W_x/a_x	% Open Area
M 100	107	37.5	0.35	9
M 110	107	50.0	0.47	16
M 115	79.5	50.0	0.63	16
M 120	107	62.5	0.58	25
M 125	79.5	62.5	0.79	25
M 130	107	75.0	0.70	36
M 140	107	87.5	0.82	49

5.2.2.1 Total Current and Quantum Efficiency

Table 5.7: Experimental and theoretical values of total current for λ=830 nm IR, 660 nm red and 525 nm green.

Layout Name	Maximum I_{total} (nA)					
	Theoretical			Experimental		
	IR	Red	Green	IR	Red	Green
M 100	338	269	198	107	114	70
M 110	541	430	316	182	203	126
M 115	456	363	266	198	222	138
M 120	749	596	437	282	317	196
M 125	584	464	341	290	324	202
M 130	941	748	550	409	455	284
M 140	1094	870	639	558	624	390

Table 5.7 shows the theoretical and experimental values of total current for λ=830 nm, 660 nm and 525 nm. Due to the complexity, TCAD models were not simulated to compare the performance. Eq. (3.30) in the advanced 2-d theoretical model was used with the same wavelength parameters used in the 1-d theoretical model. Unlike in the 1-d layouts, there is a mismatch between the 2-d sensor layouts and the theoretical model as the fabrication rules prohibited extending the cathodes to the edges of the square aperture. Practically this should lower the I_{total} compared to the 1-d sensors with similar layout parameters. However, there is no significant variation observed in the experimental values. The average quantum efficiency for a given wavelength is the same as in the 1-d sensors, showing 60% of maximum for λ=660 nm which confirms the *n*- buried layer of the cathodes serve its purpose when the wavelength of the incident light is closer to 660 nm.

5.2.2.2 Angular Sensitivity

Theoretical values of *S* were calculated from Eq. (3.27) with the same wavelength parameters used in the previous sections. Table 5.8 summarizes the theoretical and experimental values of *S* for the wavelengths used. Compared with the experimental values of 1-d sensors, 2-d sensors also show higher *S* for λ=830 nm. *S* is approximately twice that of 1-d sensors under the visible wavelength illumination, and *S* increases an additional 20% when the cathode separation is reduced by half.

Table 5.8: Experimental and theoretical values of Sensitivity for λ=830 nm IR, 660 nm red and 525 nm green.

Layout Name	Sensitivity (deg^{-1})					
	Theoretical			Experimental		
	IR	Red	Green	IR	Red	Green
M 100	0.0022	0.0020	0.0019	0.0013	0.0020	0.0019
M 110	0.0018	0.0017	0.0016	0.0022	0.0021	0.0019
M 115	0.0018	0.0017	0.0016	0.0037	0.0031	0.0028
M 120	0.0015	0.0014	0.0013	0.0025	0.0022	0.0020
M 125	0.0011	0.0011	0.0010	0.0041	0.0033	0.0028
M 130	0.0011	0.0011	0.0010	0.0028	0.0023	0.0021
M 140	0.0007	0.0007	0.0006	0.0030	0.0024	0.0021

Theoretical model shows S should be larger for smaller aperture open area. Intuitively this should be true because the light beam is more localized when the aperture is small, and this was the trend we saw from the first generation prototype sensors. However, the experimental results of the 2nd generation 2-d sensors do not agree with this prediction. Fig.5.8 shows the experimental and theoretical results of S with aperture open area for three different wavelengths, in all three cases the experimental S increase with the open area of the aperture.

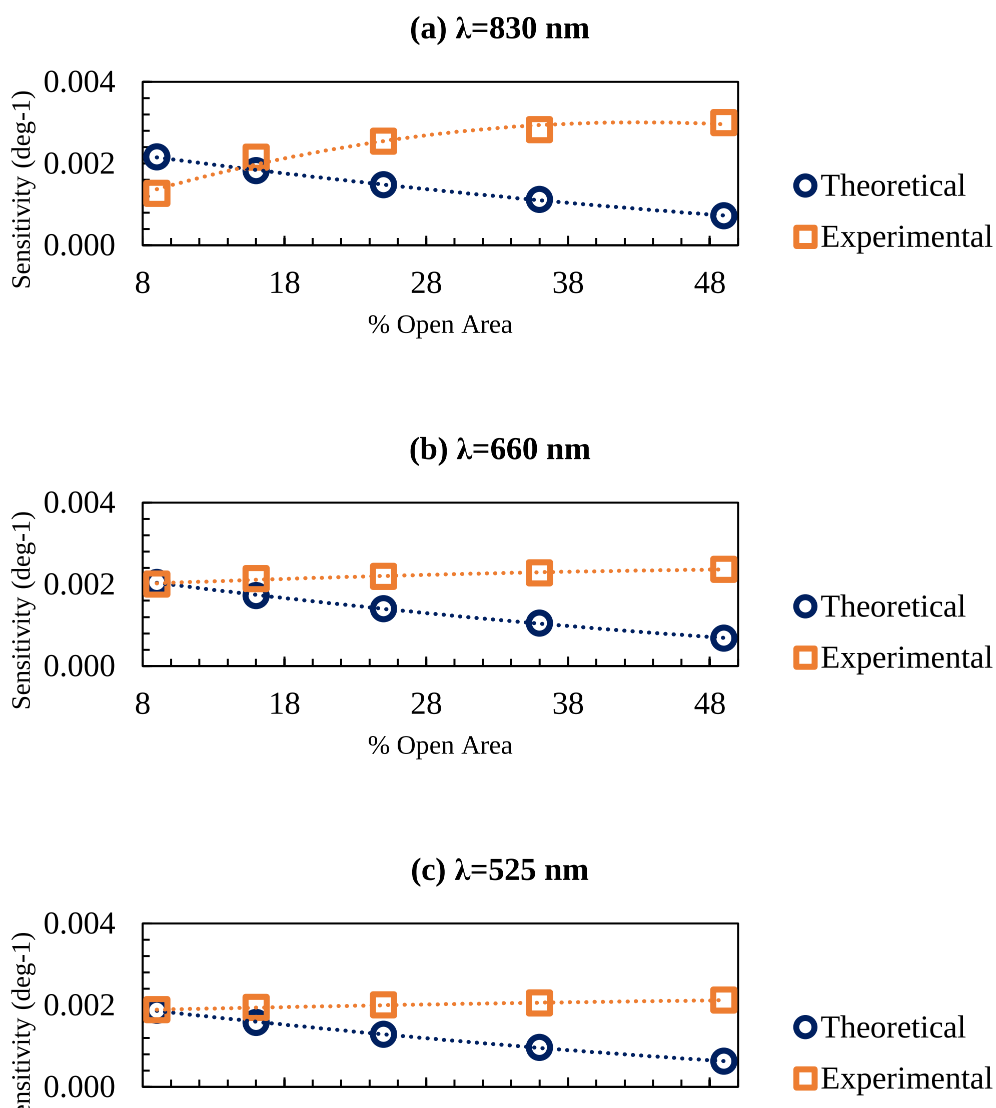

Fig.5.8: Theoretical and experimental Sensitivity for (a) λ=830 nm, (b) 660 nm and (c) 525 nm.

Why there is a disagreement between experimental and theoretical dependence of *S* on aperture area is not understood at this time. We can, however, speculate on possible causes of disagreement. Any reflection effects can be disregarded as the source of error because *S* is calculated from the normalized cathode currents. The observed behavior could possibly be explained by recombination effects. A photoelectron generated near the middle of the active region has a long distance to travel before it can be collected by a cathode and thus it is more likely to undergo recombination. Therefore, the contribution of photocarriers generated in the middle region of the active area to the cathode current is suppressed by recombination more than photocarriers generated near the cathodes. Prototype F and H with the blocking structures in the middle of the active area shows higher *S* compared to its identical layout without the blocking structure, this experimental result further confirms that the light collected at the center of the aperture does not contribute to the *S* as much as the edges. For a proper understanding of the sensor behavior one must add an appropriate recombination term in the derivation of the model.

5.2.2.3 Angular Noise Density

Table 5.9: Angular Noise Density

Layout Name	Noise Density (deg/√Hz)		
	IR	Red	Green
M 100	0.966	0.553	0.984
M 110	0.351	0.310	0.566
M 115	0.199	0.216	0.364
M 120	0.211	0.231	0.385
M 125	0.125	0.148	0.265
M 130	0.155	0.177	0.317
M 140	0.125	0.147	0.275

For the same reasons as 1-d sensors, the 2-d sensors' σ also decreases quadratically with increasing aperture area (Fig.5.9). Decreasing cathode separation by half decreases η by 40% and η is higher for λ=525 nm. Except for M 100; the sensor with smallest open area, η is approximately 30% lower in 2-d sensors compared with the 1-d sensors with similar layout parameters due to the two times higher S (Table 5.9).

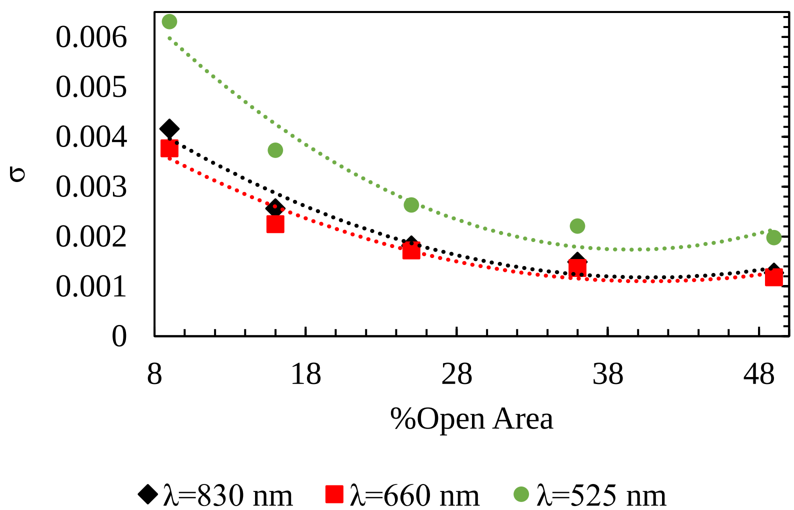

Fig.5.9: The variation of standard deviation of the normalized photocurrent, σ with the open area of 2-d sensors for λ=830 nm, 660 nm and 525 nm light sources.

5.2.2.4. Figure of Merit

Fig.5.10 compares the FoM of second generation 1-d and 2-d sensors. In both cases lower FoM is observed for sensors with higher percentage open area and FoM decreases with the cathode separation. The best FoM of new layouts in the second generation is approximately three times lower than that in first generation. If the amplifier mounted on a board could reduce the FoM further by 85%, the 1-d and 2-d sensors discussed in this section are capable of tracking human time-scale motions with ≤ 1 mm displacement accuracy as discussed in Sec.3.3.4.

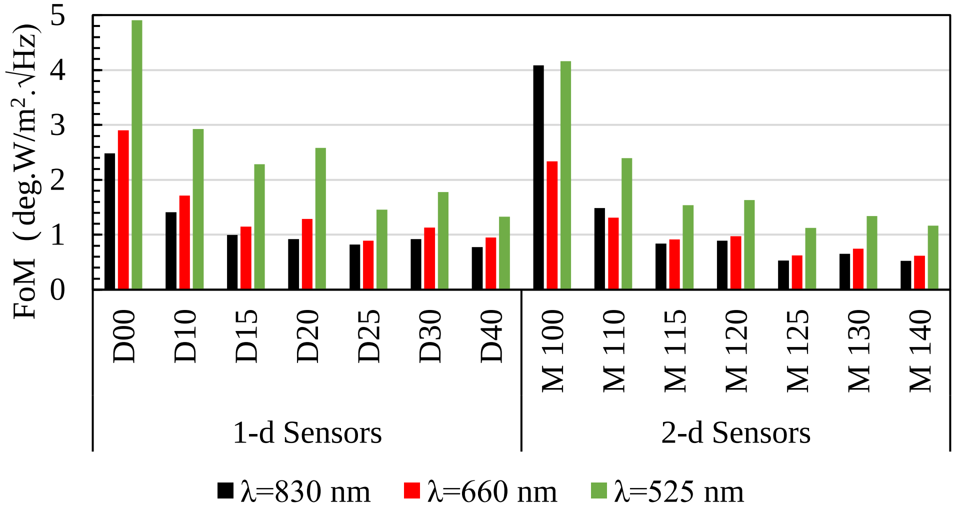

Fig.5.10: Figure of Merit of 1-d and 2-d sensors for λ=830 nm, 660 nm and 525 nm light sources.

5.3 Layout Features and Performance

This section discusses additional features which improve the quality and FoM of the sensors to be used in a wide range of possible applications.

5.3.1 Different Cathode Types

Table 5.10: Cathode features and FoM

Layout name	Cathode Feature	FoM (deg.W/µm^2.√Hz)		
		IR	Red	Green
M 030	Baseline	0.455	0.528	0.965
M 031	1/2 *n*- buried layer length	0.555	0.663	1.189
M 034	1/2 n^+ well cross- sectional area	0.476	0.610	1.092

As mentioned in the layout design, two 5.25 x 5.25 μm^2 square n^+ well cathodes in the first generation were replaced with a single 2 x 4 μm^2 square n^+ well connected to an n - buried layer in the second generation. In order to test the impact of new cathode, layout variations were made for 2-d sensor M 030 which has 100 µm unit cells with 36% open area, 82 µm cathode separation, 66 µm n - buried layer length and 2 x 4 μm^2 square n^+ well. Table 5.10 summarizes the cathode features and FoM.

Reducing the length of the cathode, reduces the quantum efficiency at the visible wavelengths. Illumination with IR creates photocarriers deeper than the n-buried layer and hence show no variations in quantum efficiency. The probability of photoelectrons reaching to the corners of the active region is low due to recombination effects and hence only a 24% reduction in S was observed with the reduction of cathode length for all the tested wavelengths, which increases FoM by the same percentage amount.

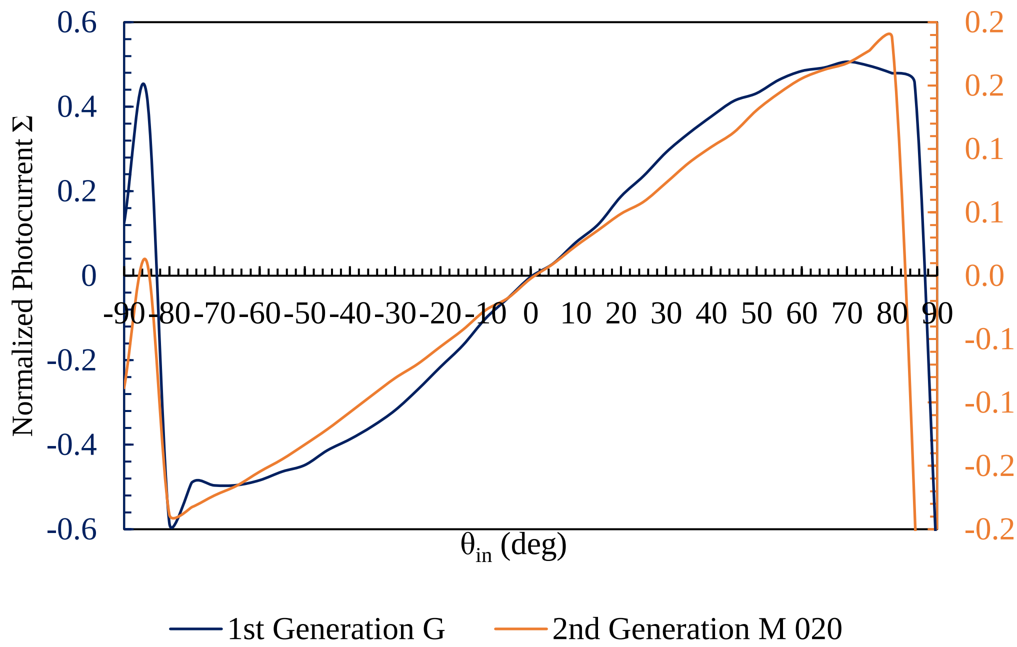

Fig.5.11: Field of View of first generation layout G and second generation layout M 20 for λ=660 nm.

Significant reduction in σ was expected by reducing the cross sectional area of the n^+ well as it reduces the contact area to the Si-SiO_2 interface where the carrier mobility decreases due to the dangling bonds. However, experimental results show only a 14% reduction under visible wavelength illumination. The other benefit of decreasing the dimensions of the n^+ well is that it could increase the field of view.

When the light is incident on the cathode, a saturation in photocurrents was observed in the prototype sensors. Fig.5.11 shows the field of view of prototype sensor G and of second generation 2-d sensor M 20, which have aspect ratios (W_x/a_x) of 0.67 and 0.61 respectively. Layout G with cathode width 5.25 µm shows a 40° linear field of view while layout M 20 with 2 µm cathode width shows a wide linear field of view about a 70° where the response remains linear almost right to the horizon.

5.3.2 Unit Cell Dimension Variations

Table 5.11: Layout variations made in 100 µm ×100 µm unit cells and their FoM

Layout Name	$2a_x$ (µm)	$2W_x$ (µm)	W_x/a_x	% Open Area	FoM (deg.W/µm^2.√Hz)		
					IR	Red	Green
M 010	82	40	0.49	16	0.91	0.97	1.69
M 020	82	50	0.61	25	0.64	0.72	1.22
M 030	82	60	0.73	36	0.45	0.53	0.96

By reducing the active area of the sensor, better performance was expected as it would reduce the total number of carrier recombination (assuming the carrier lifetime is a constant) which is a source of noise and loss of signal. 2-d layout M 110 (introduced in Sec. 5.2.2) has a 16% open area, 0.47 aspect ratio and composed of 125 µm ×125 µm unit cells, by keeping the percentage open area and the aspect ratio approximately a constant, layout M 010 was made with 100 µm ×100 µm unit cells in order to compare the effects of unit cell scaling in sensor performance. Similarly, layout M 020 and M 030 were made which contains small scale sensor unit cells of layout M 120 and M 130 respectively.

Table 5.11 contains the layout parameters and the FoM of the sensors made in smaller unit cells.

Reducing unit cell area also reduces the aperture area and the total photocurrent. Therefore, the reduction of recombination effects in the noise figure becomes insignificant relative to the total current. However, this will increase the number of carriers reaching to the cathode with position information and increase *S*. Experimental data shows sensors made with small unit cell increase *S* by 40% and the reduction in σ is below 10% for the same percentage open area. For all the tested wavelengths, the FoM of the sensors made with 100 µm ×100 µm unit cell shows about a 30% reduction compared to the sensors made in 125 µm ×125 µm unit cells (Fig.5.12).

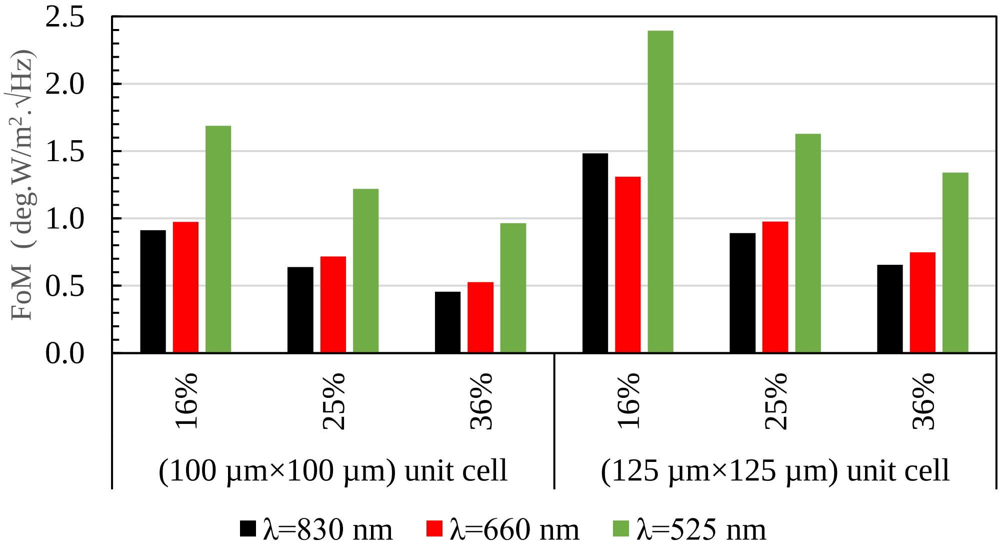

Fig.5.12: FoM of the sensors with same percentage open area made in 100 µm ×100 µm unit cell and 125 µm ×125 µm unit cell for λ= 830 nm, 660 nm and 525 nm.

5.3.3 Guard Ring

Crystallographic defects within the depletion region of the *pn* junction can randomly generate electron hole pairs [30]. When the sensor is illuminated, these randomly generated "stray" carriers can recombine with photogenerated electron and holes creating noise.

A test sensor layout (M 122) was made based on layout M 125 but adding a guard ring around each unit cell as shown in Fig.5.13.

Each guard ring consists of four n^+ wells at the corners of the unit cell connected by an *n*- buried layer which is connected to a bonding pad to be grounded in use. Experiments carried out in a dark environment (sensor covered with a black box) show I_{total} increases by 4% and the dark σ of the signal can be reduced by 15% by having a guard ring. Also, guard ring can prevent the photocarriers traveling to the neighboring unit cell.

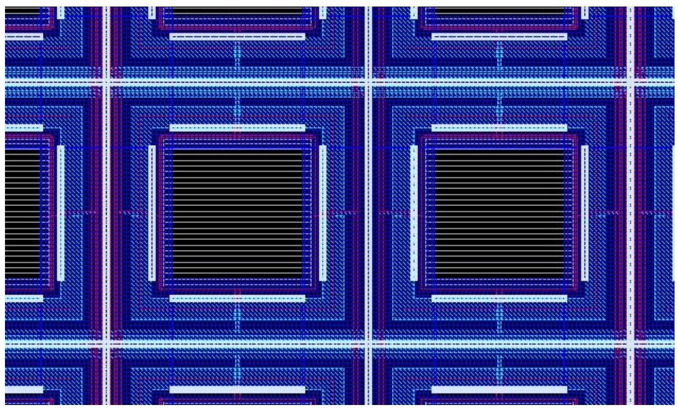

Fig.5.13: Layout view (to scale) of the Guard ring

5.3.4 On-chip Amplifier

First generation prototype sensors showed 85% improvement in FoM when used with an amplifier on board, placed few centimeters away from the sensor and connected to the sensor via soldered wire leads. A significant performance improvement was expected by monolithically integrating an amplifier, only 50 µm away from the sensor area on the same chip. However, experimental results of the second generation sensors show only a 30% improvement in the FoM using either an amplifier mounted on a board or an on chip amplifier. Table 5.12 contains the standard deviation of the normalized photo current signal measured for 50 s at 0° for λ=830 nm. To properly understand what is limiting the performance of the amplified signal we analyzed possible sources of noise (explain in chapter 7) and developed a noise model to find the optimal condition for the amplifier to operate.

Table 5.12: Amplifier types and standard deviation of the normalized photo current signal measured for 50 s at 0°

Layout	Amplifier Type	σ (10^{-3})
M 100	None	5.74
M 100	on board	3.74
M 100A	on chip, High Confidence	5.16
M 100AH	on chip, High Performance	3.89

5.3.4.1 Response speed with amplifier

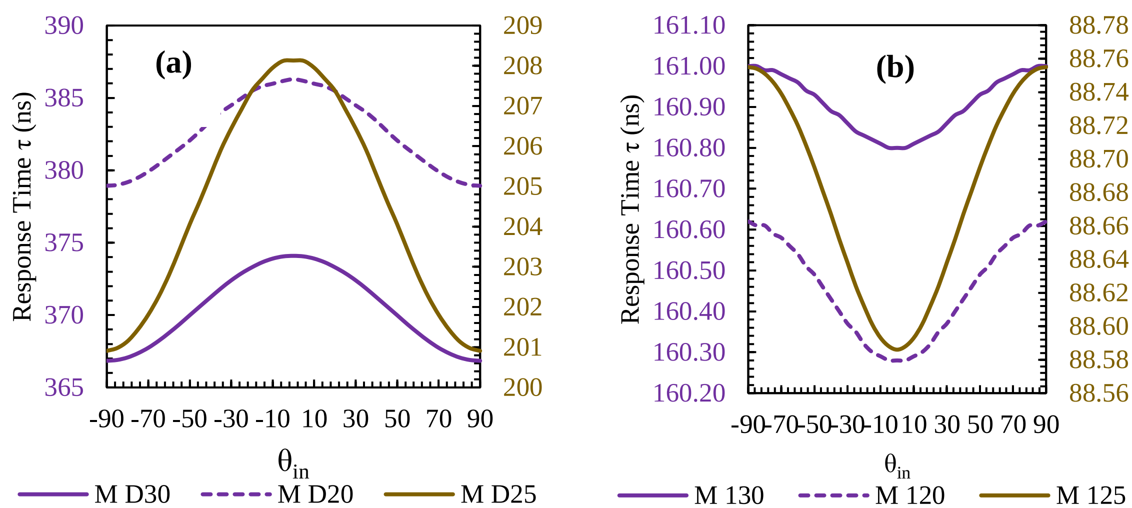

Fig.5.14: Response time with incident angle calculated from the theoretical model for (a) 1-d (b) 2-d sensors.

Fig.5.14 (a) shows the theoretical values of the 1-d sensor response time with the incident angle for layout M D30, M D20 and M D25 with 36% open area, 25% open area, and 25% open area with the closer cathodes, respectively. The response time is about 400 ns and is inversely proportional to the cathode separation. The angle dependency is insignificant. 2-d sensors show the same behavior (Fig.5.14 (b)) with half the values of 1-d sensors of the same type.

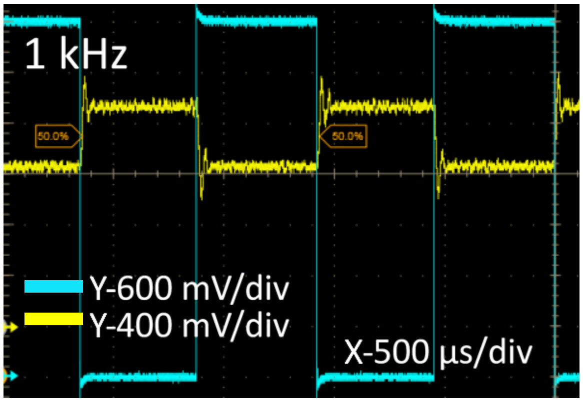

(a)

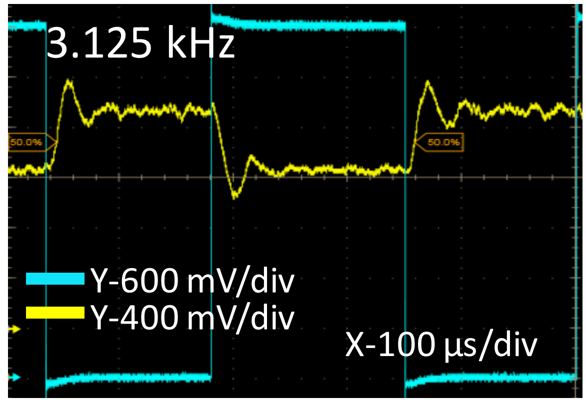

(b)

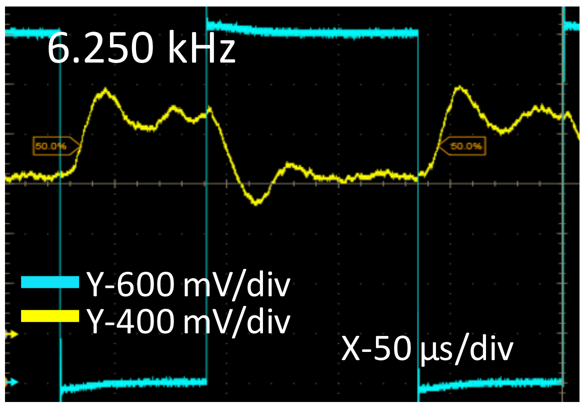

(c)

Fig.5.15: The oscilloscope trace of optical pulse across the LED in blue and the corresponding diode (cathode C1 and the anode) response in yellow for the layout M 100 under the illumination of 660 nm wavelength LED with the blinking frequency of (a) 1 kHz, (b) 3.125 kHz and (c) 6.250 kHz. Dotted grid lines show a major division of the axis and the corresponding values per divisions are given at the bottom of the plot.

Fig.5.15. shows the oscilloscope trace of the square wave driving the LED (in blue) and the corresponding Astrolabe photodiode (cathode C1 and the anode) response in yellow for the layout M 100A which has 9% open area and monolithically integrated amplifier, under the illumination of 660 nm wavelength LED. As described in Sec. 3.3.5 the speed of the sensor is ultimately limited by parasitic capacitance and the input impedance of the amplifier rather than by photocurrent drift speed.

Compared to the 1 ms RC time constant obtained with an on amplifier board for first generation prototypes (see Chapter 3.3.5), we found that having an amplifier integrated into the sensor layout decreases the RC time constant of the sensor to ~ 10 μs because monolithically integrated TIA on the sensor chip eliminate the soldered wire connectors to the Astrolabe chip and hence reduce the RC time constant significantly. Reduced time constant results higher sensor speeds.

CHAPTER 6

ASTROLABE SENSOR APPLICATION LIMITATIONS AND IMPROVEMENTS

This chapter discusses the limitations of the Astrolabe sensor as it pertains to some potential practical applications and some possible solutions that could be used to get around these limitations.

6.1 Tracking Multiple Objects

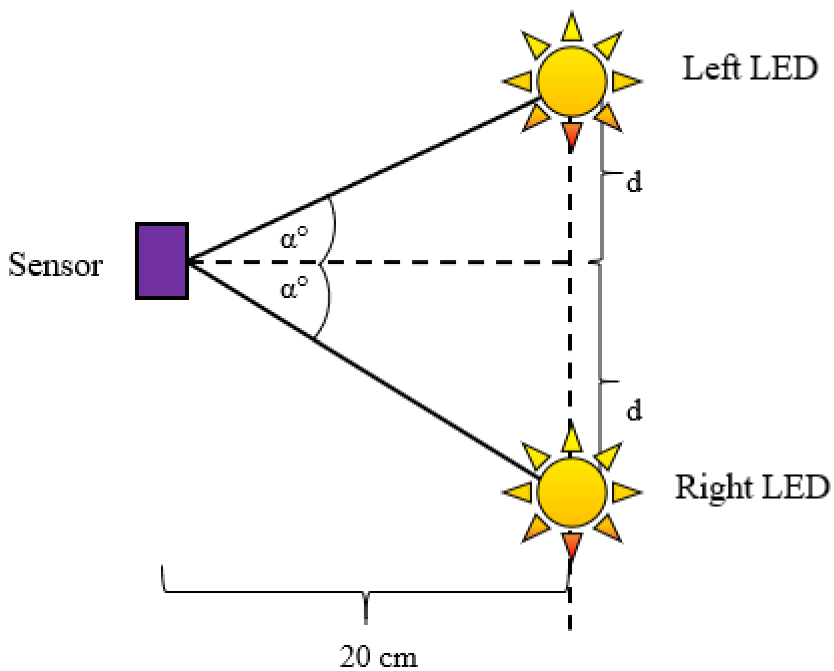

Fig.6.1: Schematic of the experimental setup-α is the viewing angle as seen from the center of the sensor. d is half the distance between LEDs.

For many application purposes, the ability to detect the position or motion of two separate light tags was tested with a 1st generation Layout A Astrolabe. As illustrated in the Fig.6.1, two 660 nm wavelength LEDs each with 300 μW incident power (directly read off the power meter placed 20 cm away from the LED) were placed such that, $\alpha = 10°$ and $d=3$ cm. Experimental data were analyzed using the standard laboratory conditions.

Fig.6.2 (a) shows the Σ for: *Case.1*: when both light sources are powered, *Case. 2*: powering only the left LED, *Case.3*: powering only the right LED and, *Case.4*:by replacing two LEDs with a single LED placed at the geometrical center with 550 µW incident power (power equivalent to the direct power read at the center when both LEDs are illuminated). The signals from *Case.1* and *Case.4* are identical while *Case.2* and *Case.3* shows a shift in Σ and its horizon. This data indicates that the sensor reads the centroid of illumination when using multiple light tags. Further, the above phenomenon is confirmed by the observed reduction in photocurrent signal with increasing α (Fig. 6.2 (b)) due to the decrease of the power read at the center as the light sources move farther apart from one another. This behavior was expected as the sensor follows simple pinhole optics. As a solution, an additional variable can be introduced to distinguish the light sources. For example, by modulating the light from each LED at a different frequency, which in case can be detected individually by combining the sensor with a lock in amplifier.

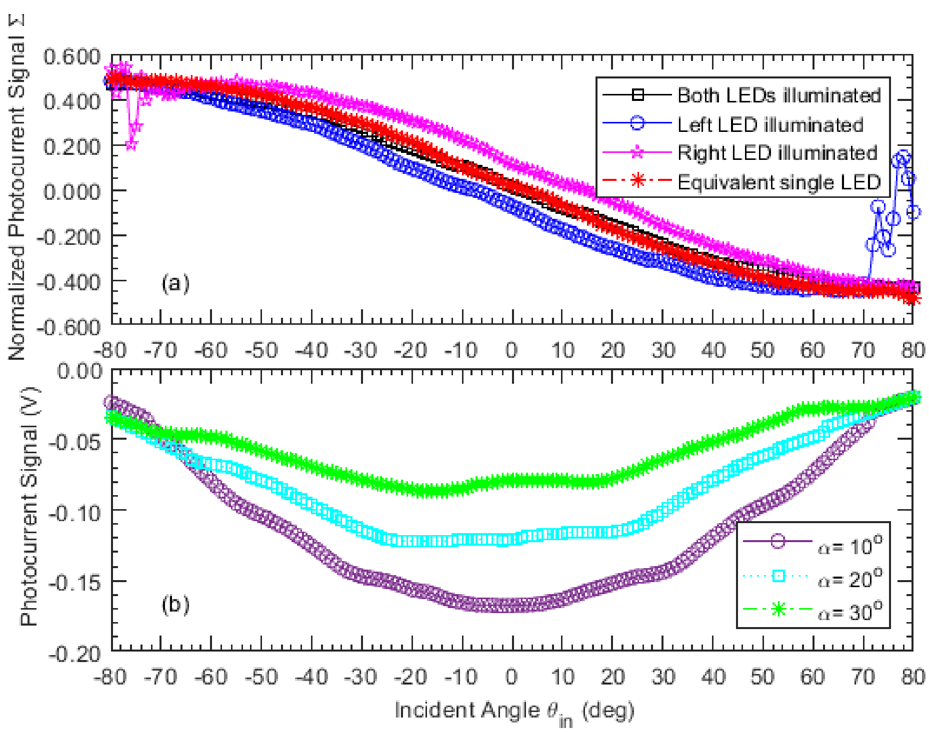

Fig.6.2: (a) Σ of Layout A under the illumination of 660 nm LED for Case.1 (black with open squares), Case.2 (blue with open circles), Case.3 (magenta with stars), and Case.4 (red with asterisks). (b) photocurrent signal when α =10° (purple with open circles), α =20° (light blue with open squares), and α =30° (green with asterisks).

6.2 Current Loss due to Surface Reflection

As described in Sec. 3.4.1, it was identified from the 1st generation prototype sensors that constructive and destructive interference between reflections at the Si–SiO_2 interface is responsible for the deviations from linearity of Σ plotted against the incident angle. These deviations add an error to the S of the sensor. Further analysis with Fresnel reflection calculations show that approximately 30% of incident power is lost due to multiple reflections at both the air-SiO_2 and the Si–SiO_2 interfaces, which can explain the roughly 60% maximum quantum efficiency obtained from the second generation sensors.

Creating a rough surface by adding ridges onto the Si surface to suppress surface reflections and enhance photocurrent density has been a major research area in energy harvesting using solar cells. Various numerical and experimental research has been done with solar cells optimizing the parameters of the ridges that could maximize the photocurrent density over a wide range of incident angles for the application purpose of harvesting maximum energy per day depending on the position of the Sun [31] [32] [33] [34] [35]. We used the same concepts on an Astrolabe sensor to minimize the reflections and enhance the sensor performance.

6.2.1 Gratings and Performance

In this section we present optimizing the surface roughness i.e. the dimensions of the gratings that could enhance the photocurrent signal and its stability over a wide range of incident angles for four different wavelengths: 830 nm, 660 nm, 525 nm and 480 nm. Then we expand the analysis to find the stability of Σ with the incident angle and hence the linearity of the Σ vs angle plot and the sensitivity *S*.

The layout variations introduced in the first generation were insufficient to understand grating effects. Therefore, a series of 1-d and 2-d sensor layouts with different grating dimensions were made in the second generation. Fig.6.3 shows an illustration of the side view (not to scale) and the basic dimensions of gratings on the Si-SiO_2 interface. The 1-d grating layouts; M D3N1, M D3N2, M D3N3 and M D3N4 contain parallel lines separated by 0.2 µm which extend all the way to the edge of the anode, perpendicular to the slit, with line widths (G_{width}) =0.225 µm, 0.325 µm, 0.425 µm, and 0.550 µm respectively.

2-d grating layouts; M 13N1, M 13N2, M 13N3 and M 13N4 contain squares separated by 0.2 μm with square widths (G_{width}) =0.50 μm, 0.60 μm, 0.75 μm, 1.00 μm respectively.

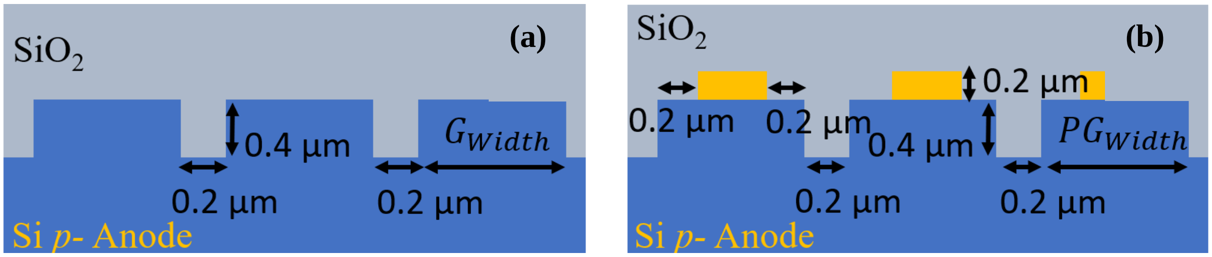

Fig.6.3: An illustration of the side view (not to scale) and the basic dimensions of (a) gratings with silicon and (b) gratings with polysilicon on the Si-SiO_2 interface.

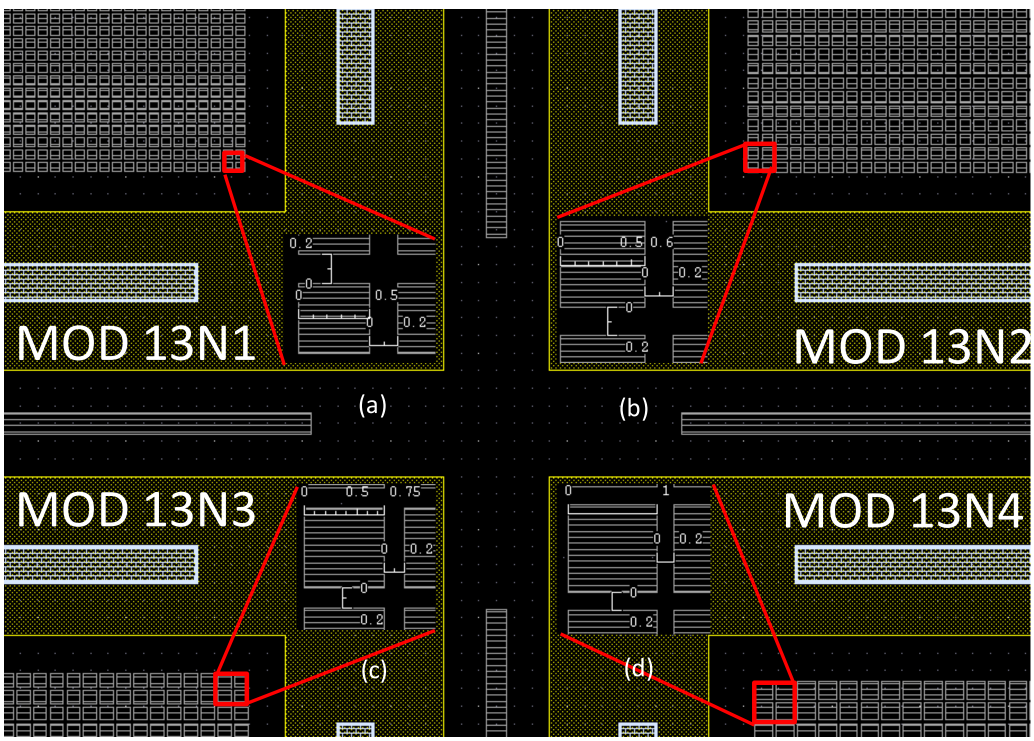

Fig.6.4: Layout (to scale) of the repeating unit of MOD 13NM. This contains the unit cells of MOD 13N1, MOD 13N2, MOD 13N3 and MOD 13N4 which has 0.2 μm parted squares with square width (G_{width}) =0.50 μm, 0.60 μm, 0.75 μm, 1.00 μm respectively. The magnified layout inside the red box with the grating dimensions is shown at the corner of each unit cell named (a),(b), (c) and (d).

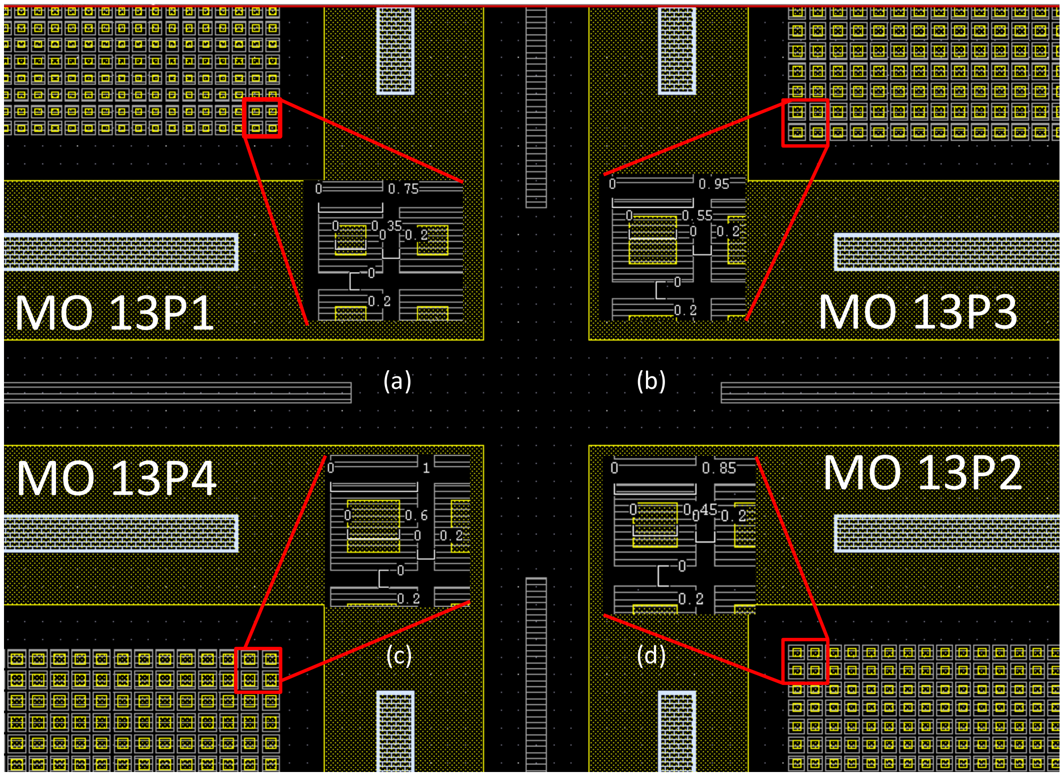

Fig.6.5: Layout (to scale) of the repeating unit of MOD 13PM. This contains the unit cells of MOD 13P1, MOD 13P2, MOD 13P3 and MOD 13P4 which has 0.2 µm parted squares with square width (PG_{width}) =0.75 µm, 0.85 µm, 0.95 µm, 1.00 µm respectively. The magnified layout inside the red box with the grating dimensions is shown at the corner of each unit cell named (a), (b), (c) and (d).

To minimize the wavelength dependence in interference, 1-d sensor M NM and 2-d sensor M 13NM were made with alternating unit cells of all four grating variations. Fig. 6.4 shows the layout (to scale) of the repeating unit of the M 13NM alternating grating arrangement. An improvement for the grating was made by adding polysilicon on top of the gratings. Fig.6.3 (b) shows an illustration of the side view (not to scale) and the basic dimensions of poly-gratings on the Si-SiO_2 interface. Reduced interference effects are expected as polysilicon has a higher refractive index. 2-d poly silicon gratings include five grating layouts; M 13P1, M 13P2, on M 13P3, M 13P4 and M 13PM with grating square widths (PG_{width}) =0.75 µm, 0.85 µm, 0.95 µm, 1.00 µm respectively, and a combination of all four gratings (Fig.6.5).

Due to the lack of resources only one polysilicon grating layout was made in 1-d, M D3NP. To test the effects of orientation of the grating with the angle of incidence M NV, a 1-d sensor was made with grating parallel to the slit aperture.

Table 6.1: Summary of grating types. All the grating layouts have 125 μm×125 μm unit cells with 107 μm cathode separation and 36% open area. In all the layouts gratings are separated by 0.2 μm distance.

Layout	Layout Description	Grating Dimensions (μm)	
		Height	Width
M 130	2-d, no gratings	-	-
M 13N1	2-d, square gratings	0.4	0.50
M 13N2	2-d, square gratings	0.4	0.60
M 13N3	2-d, square gratings	0.4	0.75
M 13N4	2-d, square gratings	0.4	1.00
M 13NM	2-d, Alternating unit cells of M 13N1, M 13N2, M 13N3 and M 13N4	0.4	0.50, 0.60, 0.75, 1.00
M 13P1	2-d, square gratings with Polysilicon	0.6	0.75
M 13P2	2-d, square gratings with Polysilicon	0.6	0.85
M 13P3	2-d, square gratings with Polysilicon	0.6	0.95
M 13P4	2-d, square gratings with Polysilicon	0.6	1.00
M 13PM	2-d, Alternating unit cells of M 13P1, M 13P2, M 13P3 and M 13P4	0.6	0.75, 0.85, 0.95,1.00
M D30	1-d, no gratings	-	-
M D3N1	1-d, line gratings, perpendicular to the cathodes	0.4	0.225
M D3N2	1-d, line gratings, perpendicular to the cathodes	0.4	0.325
M D3N3	1-d, line gratings, perpendicular to the cathodes	0.4	0.425
M D3N4	1-d, line gratings, perpendicular to the cathodes	0.4	0.550
M D3NM	1-d, Alternating unit cells of M D3N1, M D3N2, M D3N3and M D3N4	0.4	0.225,0.325, 0.425, 0.550
M D3NP	1-d, line gratings, perpendicular to the cathodes with Polysilicon	0.6	0.550
M D3NV	1-d, line gratings, parallel to the cathodes	0.4	0.225

Fig.6.6 (a) shows the 2-d sensor angle sweep of I_{total} for λ=660 nm for different grating widths. Data from each sensor were fit to an 6th order polynomial. Fig.6.6(b) shows the deviations of $I_{total,}$ obtained by subtracting the data from the polynomial fit to the signal. The deviations of the signal are repeatable sine like patterns with an amplitude that vary with the width of the gratings. As we discussed earlier, surface reflections and interference effects are responsible for the sine like patterns and for an ideal sensor this should be minimal.

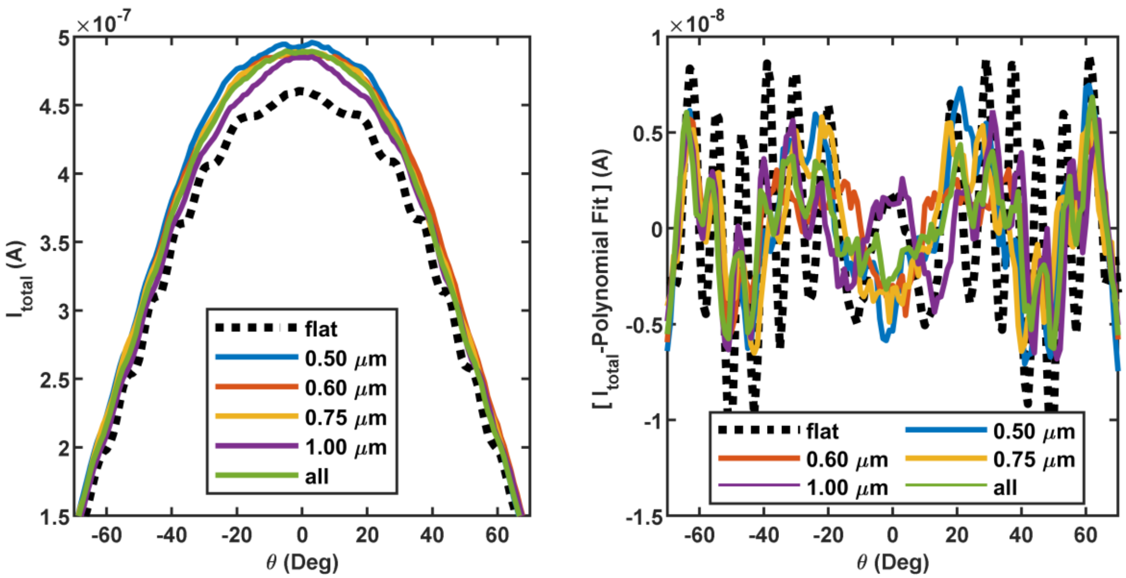

Fig.6.6: (a) shows the 2-d sensor angle sweep of I_{total} for λ=660 nm for different grating widths and (b) the fluctuations of the $I_{total,}$ obtained by subtracting its polynomial fit from the signal.

The impact of a grating depends on the incident wavelength. The quantum efficiency values calculated from the I_{total} at 0° for different grating types in 1-d and 2-d sensors are shown in Fig. 6.7. 830 nm wavelength creates carriers below the *n-* buried layer of the cathode and results in lower quantum efficiencies. Shorter wavelengths 480 nm and 525 nm create photoelectrons closer to the Si-SiO_2 interface where they lose mobility due to interface defects. Meanwhile, 660 nm wavelength creates photoelectrons closer to the buried layer resulting in relatively higher quantum efficiencies.

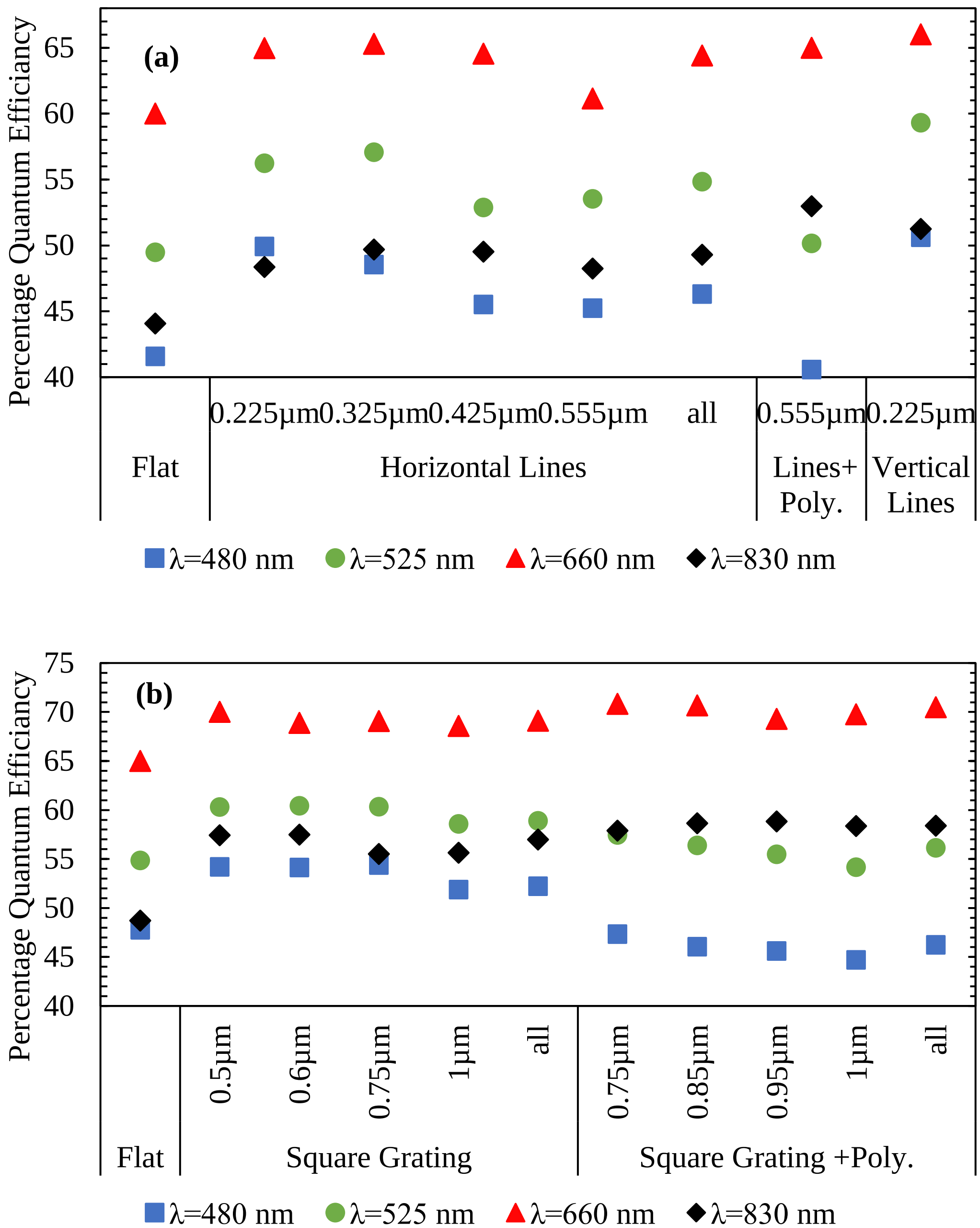

Fig.6.7: Percentage quantum efficiency values calculated from the I_{total} at 0° for different grating types in (a) 1-d and (b) 2-d sensors for λ=480 nm, 525nm, 660 nm and 830 nm.

Compared with the sensor with flat surface (no grating), gratings made with polysilicon show lower quantum efficiencies for short wavelengths with lower absorbing depths due to the additional height added by the polysilicon on top, but higher quantum efficiencies for longer wavelengths. In both 1-d and 2-d sensors, smaller width gratings show good enhancement of photocurrent. Vertical lines on 1-d sensors works better for longer wavelengths compared to the horizontal lines showing the orientation of the gratings has an impact on photocurrent enhancement. Alternating grating arrangements shows the average of its constituents.

Table 6.2: Current loss per unit area for different grating types

Layout	Current loss per unit area ($pA\ \mu m^{-2}$)			
	480 nm	525 nm	660 nm	830 nm
M 130	0.3224	0.3483	0.3653	0.6294
M 13N1	0.2880	0.3120	0.3126	0.5347
M 13N2	0.2875	0.3085	0.3262	0.5346
M 13N3	0.2877	0.3102	0.3223	0.5517
M 13N4	0.3001	0.3225	0.3375	0.5528
M 13NM	0.2985	0.3216	0.3246	0.5392
M 13P1	0.3255	0.3345	0.3156	0.5275
M 13P2	0.3315	0.3396	0.3178	0.5223
M 13P3	0.3351	0.3443	0.3261	0.5202
M 13P4	0.3394	0.3522	0.3233	0.5246
M 13PM	0.3321	0.3408	0.3174	0.5224
M D30	0.3203	0.3562	0.3813	0.6185
M D3N1	0.2781	0.3123	0.3312	0.5707
M D3N2	0.2803	0.3030	0.3325	0.5524
M D3N3	0.2989	0.3299	0.3412	0.5583
M D3N4	0.3016	0.3276	0.3589	0.5694
M D3NM	0.2946	0.3198	0.3395	0.5583
M D3NP	0.3290	0.3517	0.3332	0.5173

By using the theoretical derivations of total current for 1-d and 2-d sensors, the current loss per unit area for different types of gratings were found by taking the average of $(I_{total\_Theoretical} - I_{total\_Experimental})$ for $|\theta_{(x)in}| \leq 40°$ and dividing it by the active area of the sensor.The calculated values on Table 6.2 shows a maximum of 13% improvement with small width polysilicon gratings. It has been reported that adding an anti-reflective coating on top of the gratings can reduce the current loss per unit area by 50% [35] [36].

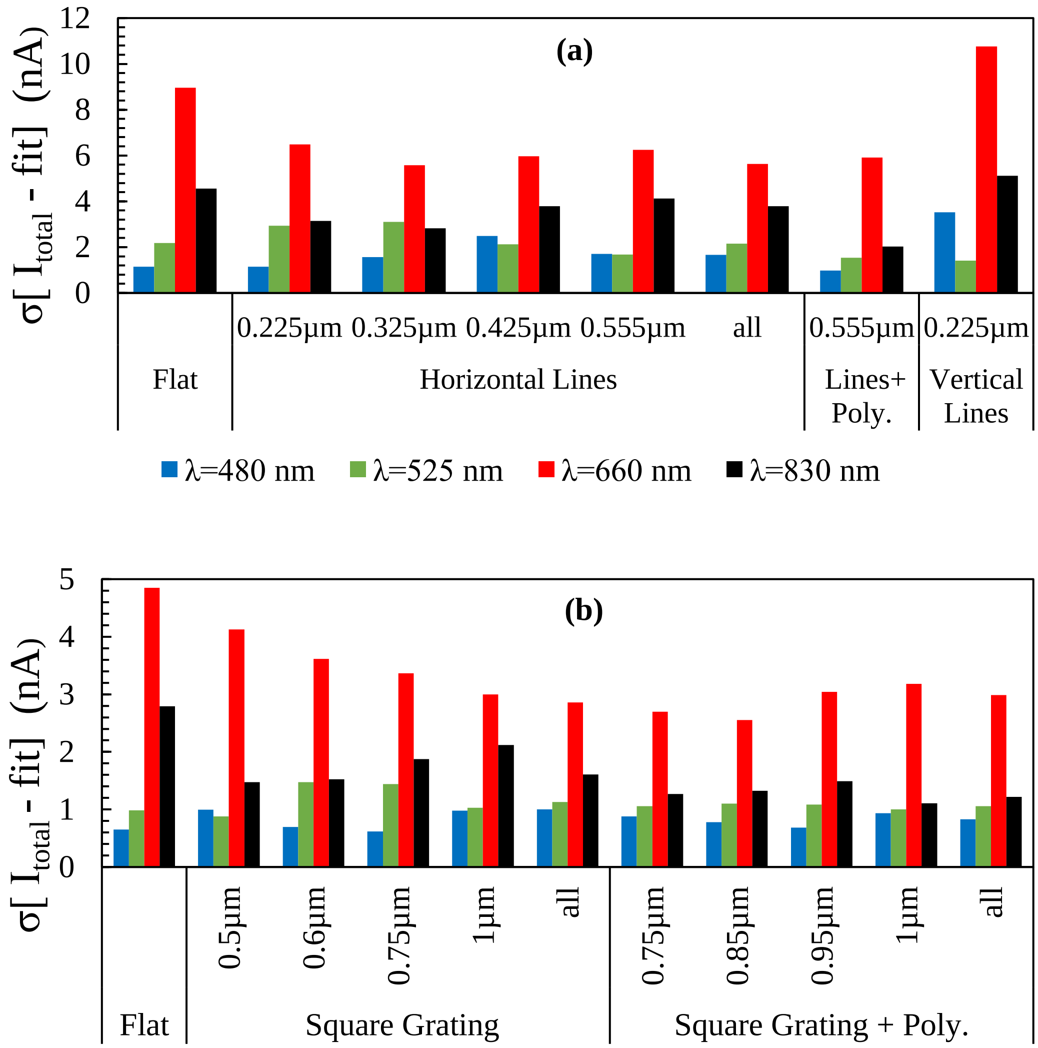

Fig.6.8: Standard deviation of the amplitude of sine like patterns of (a) 1-d and (b) 2-d grating types for $|\theta_{in}| < 40°$ under the illumination of λ=480 nm (blue),525 nm (green), 660 nm (red) and 830 nm (black).

Fig.6.8 shows the standard deviation of the amplitude of sine like patterns of 1-d and 2-d grating types for 40°< θ_{in} < 40° for four different wavelengths. The wavelength with highest quantum efficiency λ=660 nm, shows the amplitude of the deviation patterns decreases with the grating width, and in both 1-d and 2-d sensors the alternating arrangement of gratings results in lower deviation amplitude compared to the best single-direction grating arrangement. Comparing the gratings of same width, with and without polysilicon, gratings with polysilicon show a significant drop in the deviation amplitude for λ=830 nm. Vertical gratings made in 1-d sensors significantly increase the amplitude of the fluctuations for longer wavelengths. Trends in shorter wavelengths are not significant as they have a shallow absorption depth.

Although gratings enhance photocurrent signal and stability, experimental results show that the impact of gratings is not significant enough to decrease the amplitude of the fluctuations of the normalized signal Σ. Σ normalizes out the interference effects along with the photocurrents and hence show little to no variations in *S*.

6.3 Packaging

For the experiments, second generation Astrolabe sensors were wire bonded into Kyocera KD-S86832 20 lead side brazed dual inline packages. Fig.6.9 shows the variation of Σ with incident angle for two different orientations of 2-d sensor M 100. By the symmetry, orientation A and orientation B should give the same result as it corresponds to Σ_x and Σ_y respectively. However, orientation B shows a deviated signal due to the reflections coming from wire bonds on the LED trajectory. Also, the shining surface of the package may be interfering with the experimental results, something which need to be further investigated. Having shorter wires bonded to one side of the sensor package and a nonreflective black package may reduce these errors to some degree.

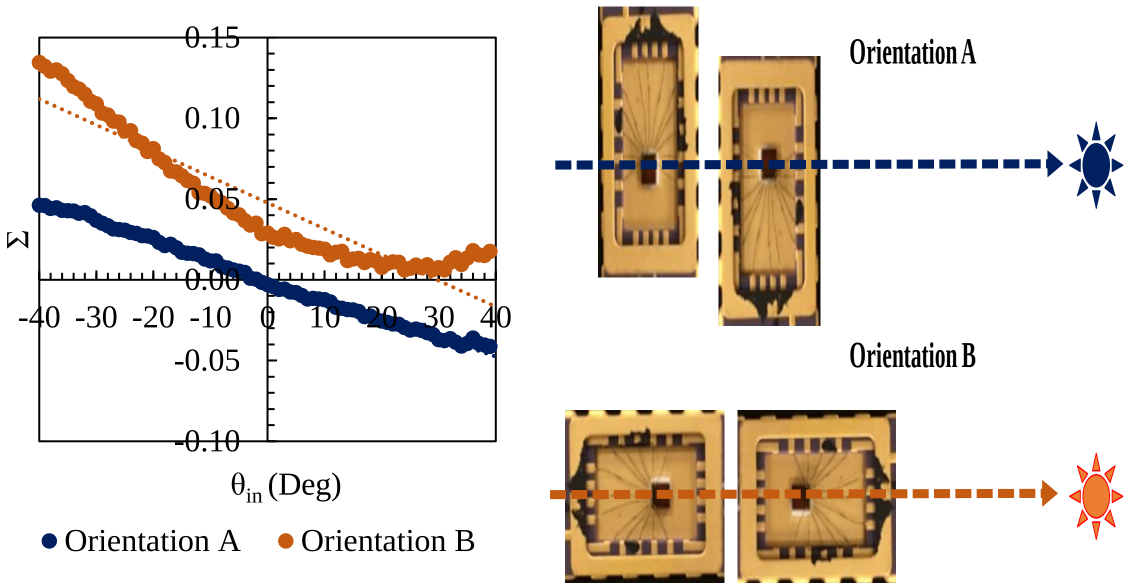

Fig.6.9: Angular response of Normalized photocurrent signal, Σ for two different orientation of the sensor package.

CHAPTER 7

CONCLUSIONS AND FUTURE DIRECTIONS

A simple integrated circuit Si "Astrolabe" capable of electronically tracking the angular position of a point-source light tag is demonstrated in this dissertation. These IC Astrolabes were fabricated using standard commercial Si CMOS processing and hence can be made at very low marginal cost. The use of pinhole optics obviates the need for external optics, so these sensors are simple, compact, and cost-effective to implement. A simple 1-d model of sensor response is developed in chapter 2, and the fundamental performance characteristics of several layout variations of first generation prototype sensors are presented in Chapter 3. Due to the mismatch between the theoretical model and experimental results of the prototype sensors, a more advanced theoretical model was developed for 1-d and 2-d sensors by considering the time dependent diffusion of the carriers in steady state. Based on the prototype experiments and modeling, a second generation of both 1-d and 2-d Astrolabe sensors was designed and manufactured in order to compare with the theoretical models. The experimental results obtained from the 1-d sensors agree well with the advanced theoretical model and with TCAD simulation results. Measurements, theory, and TCAD are all within ~ 30% of each other. Further, physical parameters such as carrier recombination and reflection at the surface obtained from TCAD simulations can be introduced as a correction terms in the theoretical model in order to design an optimal sensor for a given application in future generations.

7.1 Proposed improvements to the theoretical model

The advanced theoretical model assumes the edges of the cathodes to be the boundary of the active region of the sensor. TCAD simulations show the photodiode *p-n* junction created at the edge of the cathode introduces a depletion region of about 1 μm width into the active region of the sensor for all the 1-d sensors. The cathode separation should account for this change in the theoretical model. Although this difference is insignificant compared to the dimensions of cathode separation (107 μm and 79.5 μm) in the second generation sensors, it might impact on future sensors with small unit cell dimensions.

Further the photogeneration rate G in the theoretical model (Eq.4.7-Eq.4.16 in 1-d model and Eq.4.23 to Eq.4.33 in 2-d model in Chapter 4) could be modified to G_1 considering the reflection of light at the surface of the sensor and the depth dependence of the incident light. The absorbed amount of incident photons at the surface is $(1-R)I_{in}$ where; R is the reflection coefficient at the surface which can be calculated using Fresnel's reflection [24] and I_{in} is the incident intensity in photons. Also, the incident intensity at the top of the surface decay exponentially with the depth Therefore, for a given wavelength. G_1 can be written as;

$$G_1 = (1-R)I_{in}e^{-\alpha z} \tag{7.1}$$

Here, α absorption coefficient, z is the coordinate normal to the surface and I_{in} is given by,

$$I_{in} = \frac{P_{in} cos\theta_{in}}{\pi r^2}\left(\frac{\lambda}{hc}\right) \tag{7.2}$$

Where, P_{in} is the power for a normal incidence read by a detector with a radius r, h is the Plank's constant, c is the Speed of light and λ is the wavelength of the incident light.

In addition to diffusion, photogenerated carriers undergo recombination which was neglected in the theoretical model. Carrier recombination can happen through multiple relaxation process including band-to-band recombination, Shockley–Read–Hall trap-assisted recombination, Auger recombination and surface recombination [37] [38] [39] [40] [41]. The contribution of each recombination process depends on the incident wavelength, surface properties, doping concentrations etc. which makes the theoretical calculation of carrier loss due to recombination complex.

An easy approach to address the correction terms is to simulate a realistic device in TCAD that matches the process parameters used for sensor fabrication with fine meshing in order to account for reflection effects and recombination effects. Our collaborator at Texas Instruments, Dr. Hal Edwards, has done optical simulations for the 1-d sensor TCAD models made in the same process flow of sensor fabrication with effective optical simulation parameters taken from the literature for optical devices [42] [43].

Fig.7.1 shows the TCAD simulation results of modified Generation rate G_1 (solid lines) and Recombination $\mathcal{R}$ for different θ_{in} for λ=660 nm on the Astrolabe layout D00 with 9% open area. The parameters used for the photogeneration match the standard laboratory measurement conditions. Table 7.1 contains the maximum value of $\mathcal{R}$ at θ_{in} =0° obtained for different layouts for λ=830 nm, 660 nm and 525nm. One can simply replace G in the theoretical model (Eq.4.7-Eq.4.16 in 1-d model and Eq.4.23 to Eq.4.33 in 2-d model in Chapter 4) with $G1\text{-}\mathcal{R}\cos\theta_{in}$. to add the correction terms into the theoretical model. The TCAD models can further be improved with fine meshing and increased number of incident rays (reduce the possible contribution to edge noise due to random fluctuations), in order to obtain results that are close to the experimental results.

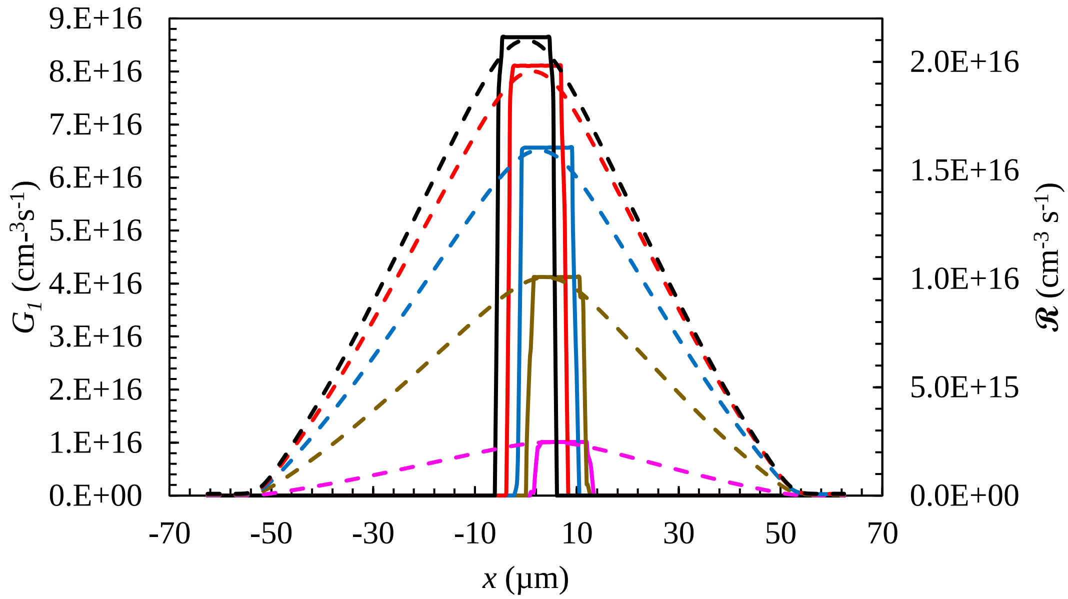

Fig.7.1: TCAD simulation results of modified Generation rate G_1 (solid lines) and Recombination $\mathcal{R}$ (dashed-line)s vs. distance from the two cathodes in Astrolabe layout D00. Here the cathode boundaries are at x = ± 50 µm. The incident angles are θ_{in} =-40° (pink), -60°(yellow), -40° (blue), -20° (red) and 0° (black) for λ=660 nm light.

Table 7.1: TCAD simulation results for the carrier recombination $\mathscr{R}$ (at θ_{in} =0°) obtained for different layouts for 830 nm IR, 660 nm red and 525 nm green LEDs.

Layout Name	$\mathscr{R}\times10^{16}$ ($cm^{-3}s^{-1}$)		
	IR	Red	Green
D00	2.36	2.10	1.15
D10	4.01	3.60	2.01
D15	3.04	2.71	1.51
D20	5.88	5.30	3.02
D25	4.37	3.90	2.24
D30	7.77	7.01	4.10
D40	9.41	8.49	5.11

7.2 Proposed Layout improvements

The second generation 1-d sensors show very good agreement with the advanced theoretical model and the TCAD simulation results. The theoretical model can be further improved by incorporating the device physics of the TCAD models. Also, for a given cathode separation, for a given wavelength, normalized photocurrent signal fluctuations show a quadratic relation with the open area of the sensor. By using the modified theoretical model and the quadratic relation with the noise figure, one can predict the dimensions of a sensor with a particular FoM needed for an application. Due to the complexity of the 2-d sensors it is difficult to simulate accurately in TCAD and the deviations between the experimental and theoretical model results are hard to explain.

There is high demand for an industrial application sensor capable of 2-d tracking. For the goal of 2-d tracking, a sensor was made with alternating simple 1-d sensor unit cells in x and y direction arranged in a "checkerboard" geometry (Fig.7.2 (a)).

Fig.7.2 (b) shows the repeating unit cell of the sensor with cathode separation comparable to the 2-d model. If the currents read on the cathodes C_{ax}, C_{-ax}, C_{ay} and C_{-ay} are , I_{ax}, I_{-ax}, I_{ay} and I_{-ay} respectively. Then the normalized photocurrent signals corresponds to horizontal and vertical movement of the LED, Σ_x and Σ_y are given by,

$$\Sigma_x = \frac{I_{a_x} - I_{-a_x}}{I_{a_x} + I_{-a_x}}$$
$$\Sigma_y = \frac{I_{a_y} - I_{-a_y}}{I_{a_y} + I_{-a_y}} \tag{7.3}$$

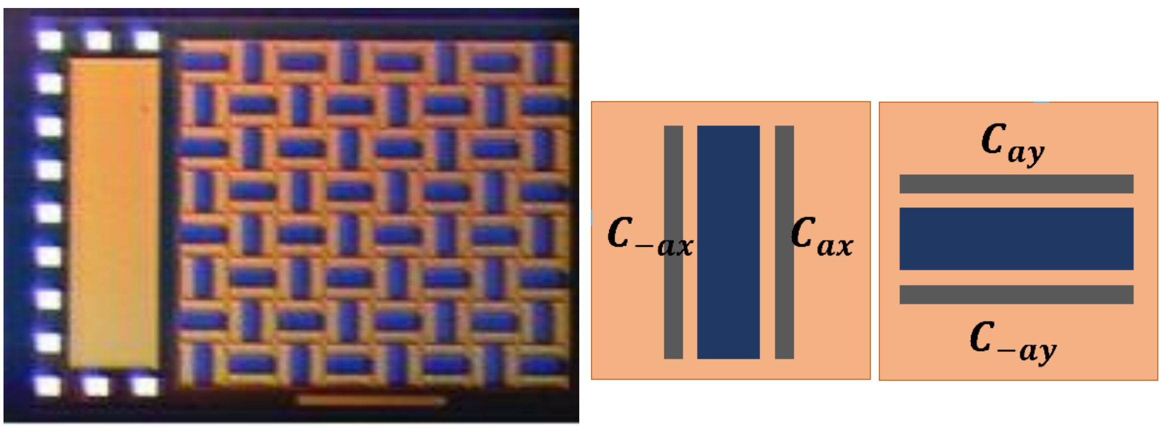

(a) (b)

Fig.7.2: (a) The sensor made by alternating simple 1-d sensor unit cells in *x* and *y* direction in a "checkerboard" arrangement (b) repeating unit of the sensor with comparable cathodes to 2-d model.

By symmetry, *S* for horizontal and vertical displacement of the light spot should be the same. Therefore, the checkerboard arrangement of the 1-d sensors operates in the same way as a 2-d sensor array but can be described with a much simpler and effective theoretical model. Fig.7.3 show the photocurrent responses of cathode C_{ax}, C_{-ax}, C_{ay} and C_{-ay} obtained from the checkerboard arrangement of 1-d sensor D30 with 30% open area for the horizontal movement of an LED light tag.

The photocurrent responses at each cathode are almost identical and do not show photocurrent imbalance with respect to the position of the light spot.

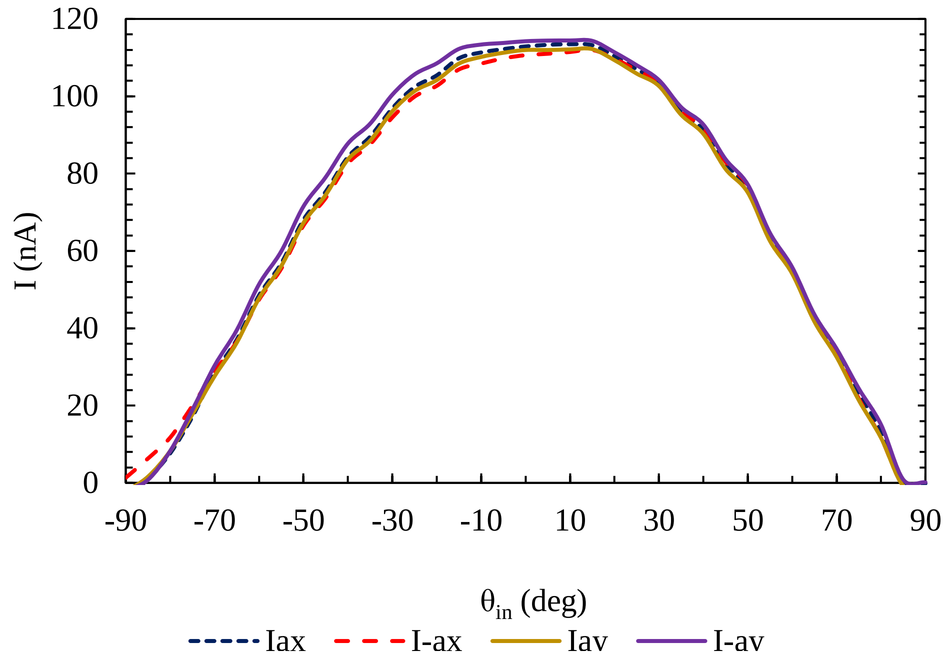

Fig.7.3: Photocurrent responses obtained from the checkerboard arrangement of 1-d sensor D30 with 30% open area for the horizontal movement of LED. Blue dashed, red dashed, gold solid and purple curves show the photocurrent at cathode C_{ax}, C_{-ax}, C_{ay} and C_{-ay} respectively.

The main drawback of the sensor construction in practical operation is that the orientation of the sensors allows the photocarriers to travel all the way to the cathodes of the neighboring unit cell, resulting in nonlinear Σ_x and Σ_y. However, we realized this problem only in retrospect, after measuring the angular response of this layout. This problem could be prevented by adding a guard ring around each unit cell to prevent carriers moving to the neighboring unit cell. As an added benefit, such guard rings can reduce the dark current which lowers the noise density and hence increases the sensor performance.

Patterning ridges on the Si surface can reduce the reflections and increase the quantum efficiency of the sensor (Sec.6.2). Experimental results discussed in Chapter 6 shows ridges parallel to the cathode increase the quantum efficiency compared to ridges perpendicular to the cathodes. However, ridges perpendicular to the cathode shows good signal stability (standard deviation of the signal is low) compared to ridges parallel to the cathode. Therefore, it would be interesting to try vertical and horizontal ridges in a "herringbone pattern" on the Si surface in future generations.

7.3 Noise Model

A figure-of-merit is introduced that helps determine the uncertainty in angular measurement for any given measurement bandwidth and incident optical power. Sensors with better performance should have a smaller FoM. First generation prototype sensors showed 85% improvement in FoM when used with an amplifier on board, placed a few centimeters away from the sensor and connected via soldered wire leads. However, the FoM of the first generation Astrolabes was still a factor of ~ 20 too large to be practically useful.

A significant FoM performance improvement was expected by integrating an on-chip amplifier 50 µm away from the sensor into the layout of the advanced second generation sensors as it eliminates the long electrical line connections which are vulnerable to noise pick-up. Second generation sensors were made with and without integrated on-chip amplifiers. The second generation sensors used without an amplifier showed FoM ~ 30% lower than the unamplified signals from first generation devices. When used with an on-board amplifier the FoM of these second generation sensors was further reduced by ~ 30%, not the 85% reduction in FoM seen in the first generation Astrolabes upon use with an amplifier on board. Unfortunately, second generation sensors with integrated on-chip amplifier did not show better FoM compared to the sensors using on-board amplifier. Therefore, possible noise sources were investigated to identify the impact of each noise source on sensor performance.

The sensor characteristics presented in this dissertation were analyzed for the photocurrents relative to the different background laboratory environments.

Comparisons of sensor signal with and without background illumination and in a dark environment (covered with a black box) showed that the noise density σ varied by less than 10% across these backgrounds, which confirms the noise interference from the background is negligible.

Fig.7.4 shows that σ obtained from the unamplified signal of second generation sensor M 100 is roughly inversely proportional to the root of the measurement integration time for frequencies higher than 50 Hz when the LED is powered by a DC battery and when it is powered by an AC power supply. For the same measurement conditions, the results of sensors with on-board amplifier show similar behavior. Therefore, we conclude that white noise is dominant for frequencies greater than 50 Hz, rather than power-line interference.

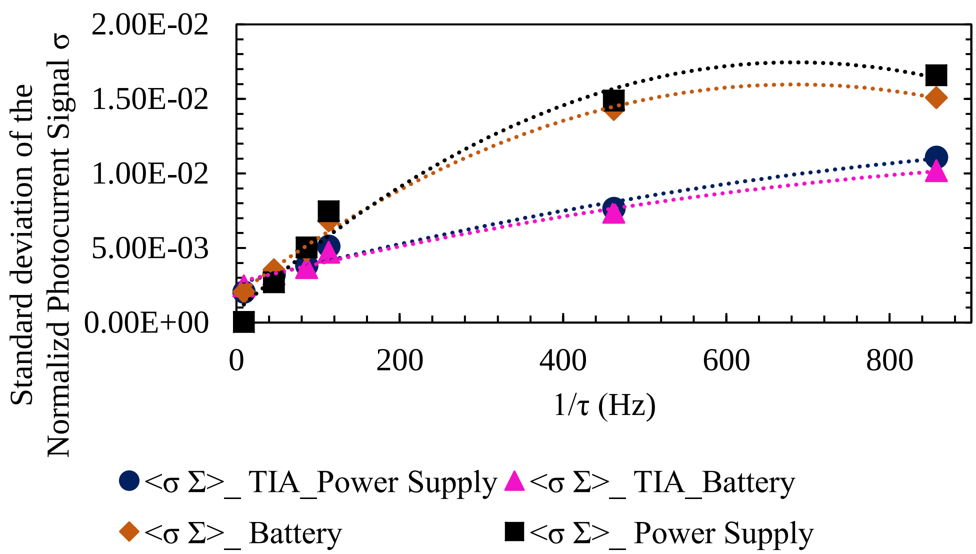

Fig.7.4: Variation of σ with different measurement integration time obtained from the unamplified signal of second generation sensor M 100 when the LED is powered by a DC battery (in orange diamonds) and when its powered by a AC power supply (in black squares). Pink triangles and blue circles show the results obtained from the same sensor with a TIA mounted on a board when the LED is powered by a DC battery and when its powered by a AC power supply.

The noise model in Fig.7.5 shows the possible noise sources in a single photodiode and amplifier circuit network that could affect the final output of the signal. This model was designed by our collaborators at the UTD Electrical Engineering Department, Dr. Andrew Marshall and Akash Dey, based on the Astrolabe design layouts and measurement data we shared with them. The shunt resistance of the photodiode R_{ph} has a Johnson noise associated with it. This type of noise is the dominant current noise in photovoltaic (unbiased) operation mode [44]. The Johnson noise of a load resistor R for a measurement bandwidth B can be calculated by, $V_{nR} = \sqrt{4k_B TRB}$ where k_B is the Boltzmann's constant and T is the absolute operating temperature in Kelvin [44]. The shot noise of the photodiode I_{nph} is related to the statistical fluctuation in both the photocurrent and the dark current [30]. For the bandwidth of measurement B the shot noise can be calculate using,

$$I_{nph} = \sqrt{2q\left(I_{ph} + I_D\right)B} \tag{7.4}$$

Further the I_D of Eq.7.4 can be found by studying the current-voltage characteristics of the photodiode. If the reverse saturation current is I_{sat} then;

$$I_D = I_{sat}\left(e^{\frac{qV_{RB}}{k_B T}} - 1\right) \tag{7.5}$$

Where, V_{RB} - Reverse bias voltage and q = charge of the electron [30].

The photodiode capacitance C_{ph} is mainly the *pn*- junction depletion capacitance which can be calculated by,

$$C_{ph} = \frac{A}{(V_0 - V)^{1/2}}\left[\frac{q\epsilon_{Si} N_a N_d}{(N_a + N_d)}\right]^{1/2}$$

$$V_0 = \left(\frac{k_B T}{q}\right) ln\left[\frac{N_a N_d}{{n_i}^2}\right] \tag{7.6}$$

Where, N_a = acceptor concentration of the anode, N_d- donor concentration of the cathode, n_i = intrinsic carrier concentration of Si, V_0 = built in voltage, ϵ_{Si} = dielectric constant of the Si, and, A = cross sectional area of the depletion region [30].

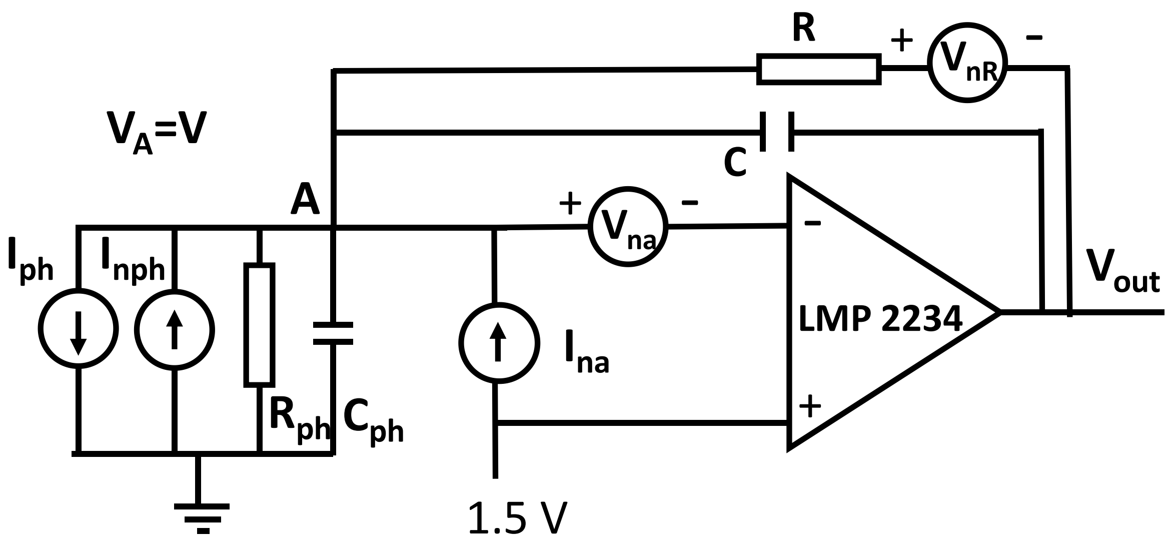

Fig.7.5: Noise Model; shows the possible noise sources in a single photodiode and an ideal amplifier circuit network. R_{ph},C_{ph} and I_{nph} are the shunt resistance, the *pn*-junction capacitance and the shot noise of the photodiode respectively. R and C are the load resistance and the compensation capacitance of the network. V_{nR} is the voltage drop due to the load resistor. I_{na} and V_{na} are the current and the voltage noise of the amplifier respectively.

The other component of the noise model is compensation capacitance of the network C. I_{na} and V_{na} are the current and the voltage noise from the amplifier respectively. The total current of the network at the angular frequency $\omega = 2\pi f$ when the voltage at the joint A is equal to V;

$$I_{nph} + I_{na} = V\left(\frac{1}{R_{ph}} + j\omega C_{ph}\right) + \frac{V - V_{out}}{\frac{1}{j\omega C}} + \frac{V - V_{out} - V_{nR}}{R} \tag{7.7}$$

After subtracting the quiescent 1.5 V quiescent voltage of the network, the voltage output is then;

$$V_{out} = V_{na}\left[1 + \frac{\left(\frac{1}{R_{ph}} + j\omega C_{ph}\right)}{\left(\frac{1}{R} + j\omega C\right)}\right] - \frac{V_{nR}}{1 + j\omega RC} - \frac{I_{nph}R}{1 + j\omega RC} + \frac{I_{na}R}{1 + j\omega RC} \qquad (7.8)$$

Therefore, the root mean square noise (RMSN) at the output,

$$RMSN = \left\{\left(V_{na}\left[1 + \frac{\left(\frac{1}{R_{ph}} + j\omega C_{ph}\right)}{\left(\frac{1}{R} + j\omega C\right)}\right]\right)^2 + \left(\frac{\sqrt{4k_BTRB}}{\sqrt{1 + \omega RC}}\right)^2 + \left(\frac{I_{nph}R}{\sqrt{1 + \omega RC}}\right)^2 + \left(\frac{I_{na}R}{\sqrt{1 + \omega RC}}\right)^2\right\}^{1/2} \qquad (7.9)$$

Fig.7.6 shows the signal to noise ratio at the output for (a) I_{ph} =0.5 nA, (b) I_{ph} =5 nA , (c) R=10 MΩ, (d) R=1000 MΩ, (e) C= 0.5pF and (d) C= 50 pF. The values were calculated from Eq.7.10 and 7.11 by using the LMP 2234 amplifier noise density values at f = 1kHz; I_{na}=10 fA/$\sqrt{Hz}$ and V_{na}= 60 nV/$\sqrt{Hz}$. Also, at f = 1kHz V_{nR} is white noise equal to $\sqrt{4k_BTR}$.

The R and C values used to build the circuit are 100 MΩ and 5 pf respectively. R_{ph} was obtained from the slope of the current-voltage curve of the photodiode at the origin and the C_{ph} was calculated from Eq. 7.8. For the Astrolabe sensor R_{ph} ~ 5 GΩ and C_{ph} ~ 5pF.

Calculated values in Fig.7.6 show that the photodiode noise is dominant. The signal to noise ratio at the output is low for frequencies lower than 100 Hz. Fig.7.6 (a) and (b) show that at high signal intensities the overall signal-to-noise at the output doesn’t improve owing to the photodiode shot noise and flicker noise. With high transimpedance gain (Fig.7.6 (c) and (d)) or high compensated capacitance value (Fig.7.6 (e) and (f)) the overall signal to noise at the output improves significantly. This however will increase the RC time constant and hence reduce the speed of the measurement.

The most important lesson overall would be to use a band-pass filter to tightly filter the signal frequencies of interest.

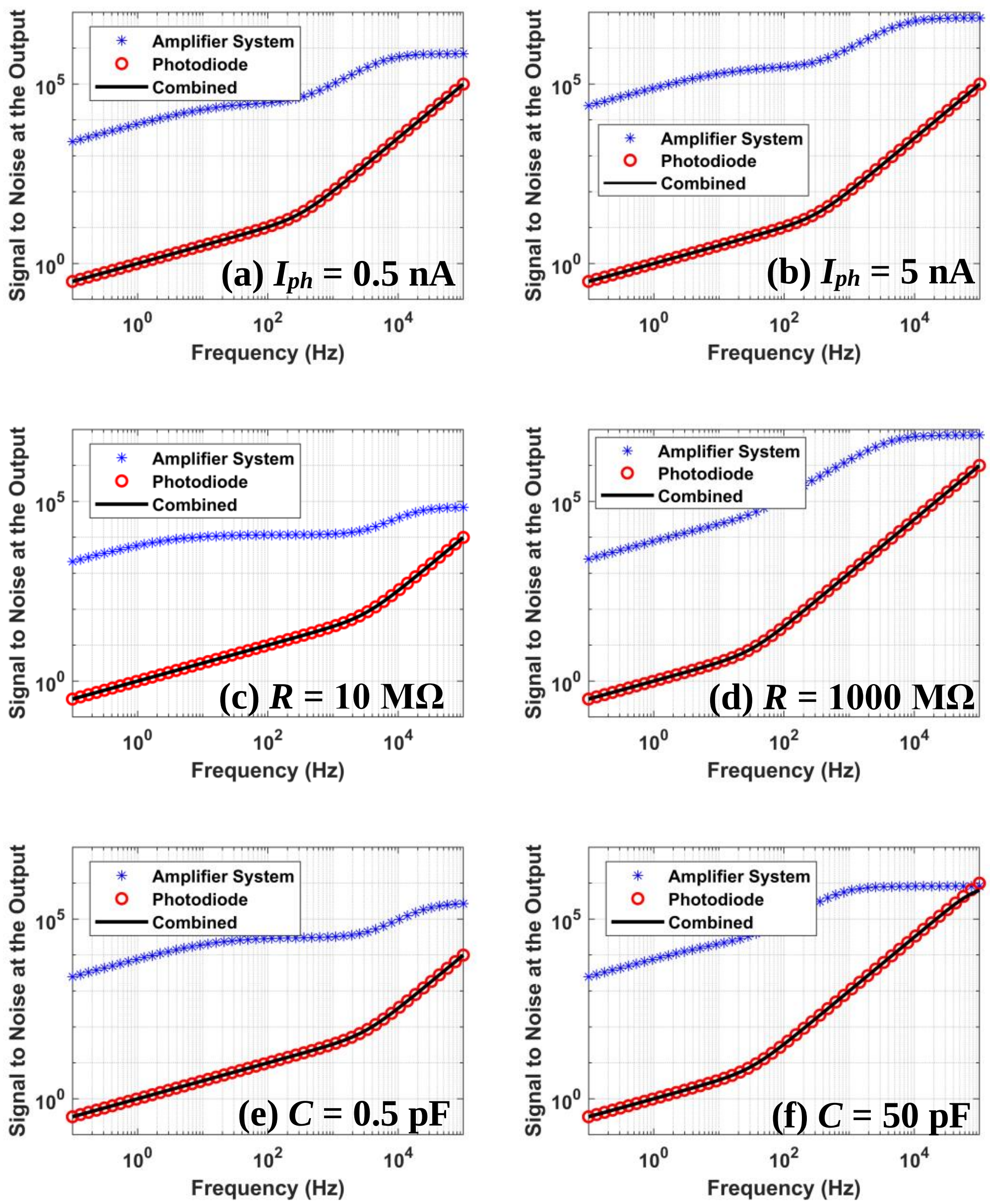

Fig.7.6: Signal to noise ratio at the output for (a) I_{ph} =0.5 nA, (b) I_{ph} =5 nA , (c) R=10 MΩ, (d) R=1000 MΩ, (e) C= 0.5pF and (d) C= 50 pF. Blue asterisks, red circles and the black line represents the signal to noise ratio of the output from amplifier system, Photodiode and the amplifier photodiode combined.

A lock-in amplifier could be used to implement such band-pass filtering. The lock-in amplifier detects a modulated signal, i.e., a signal that oscillates at a well-defined frequency and phase that could be obscured by much larger noise sources. To do so, a reference signal whose frequency and phase is the same as the signal modulation is supplied to the lock-in. This reference provides both the frequency and phase of the expected signal. To narrow its output to a small bandwidth around the expected frequency at the specified phase, the input and reference signals are multiplied together. If the signal and reference are correlated their multiplication will be positive on average. Random noise and the reference, even at the same frequency, are uncorrelated and therefore their multiplied value will fluctuate in time and average to zero. A low pass filter picks out the part of the signal that is correlated with the reference essentially by averaging the output of the mixer, This is the output from the lock-in amplifier [45] [46].

Table 7.2: Average standard deviation of an amplified photocurrent signal $I_{a_x}$of layout M 100 measured by a Lock-in amplifier for 50 s with 10 ms and 30 ms integration time at θ_{in} = -40°,0° and 40° for λ =830 nm.

Blinking Frequency (Hz)	$\sigma_{V_{a_x}}$ ×10^{-4} (V)	
	τ =10 ms	τ =30 ms
166	12.5	4.90
495	3.26	1.75

Table 7.2 summarizes the standard deviation of an amplified photocurrent signal measured by a lock-in amplifier for 50 s with 10 ms and 30 ms integration time for two modulation frequencies. The reference of the lock-in amplifier is the square-wave voltage used to drive the LED, which was generated by a programmable Arduino setup in order to cause the LED to blink at a known frequency and phase.

The $\sigma_{V_{a_x}}$ shown in Table 7.2 is the average of three values obtained at θ_{in} = -40°,0° and 40° under the standard laboratory conditions from the layout M 100. With the onboard amplifier and our standard DC Source Measure Unit setup , $\sigma_{V_{a_x}}$ = 8.03×10^{-4} V for τ =21.7 ms and λ=830 nm in steady state (no blinking).

Compared to this DC value of $\sigma_{V_{a_x}}$, the average value of $\sigma_{V_{a_x}}$ obtained using a modulated (blinking) LED and lock-in amplifier for τ =10 ms and τ =30 ms at 495 Hz blinking frequency, shows a 66% improvement. Future work aims to improve the performance characteristics by using a measurement setup with lock-in amplifiers.

APPENDIX A

SECOND GENERATION SENSOR IDENTIFICATION

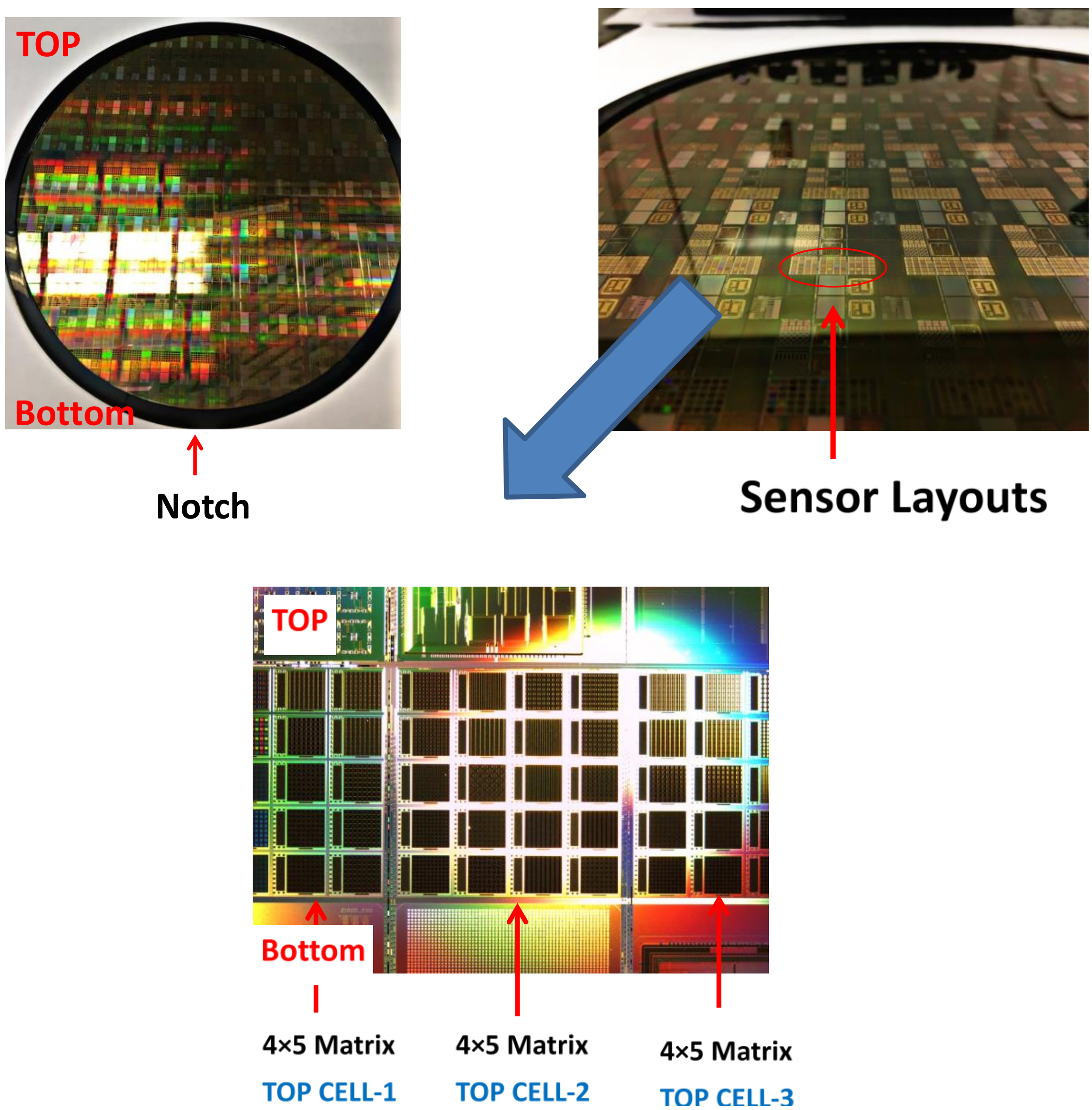

Fig.A.1: How to identify the second generation sensor layouts on the wafer.

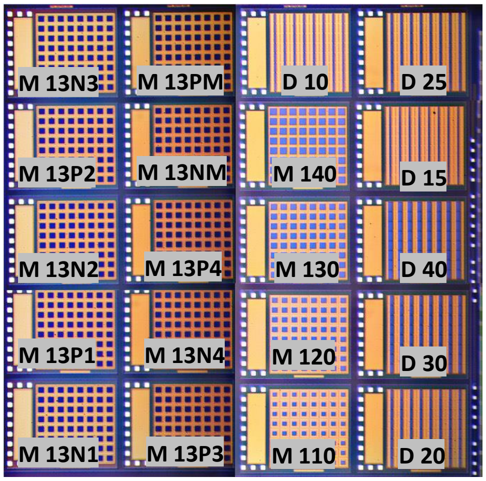

TOP CELL 1			
1.5.1	1.5.2	1.5.3	1.5.4
1.4.1	1.4.2	1.4.3	1.4.4
1.3.1	1.3.2	1.3.3	1.3.4
1.2.1	1.2.2	1.2.3	1.2.4
1.1.1	1.1.2	1.1.3	1.1.4

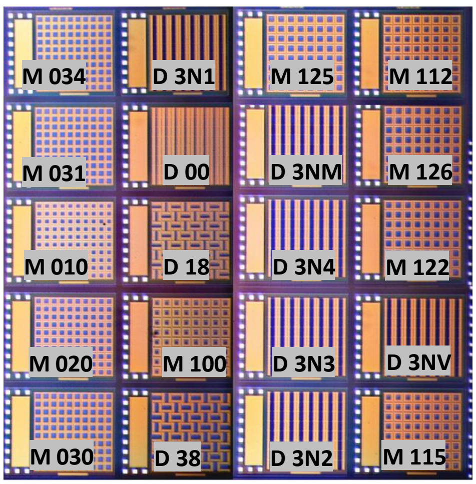

TOP CELL 2			
2.5.1	2.5.2	2.5.3	2.5.4
2.4.1	2.4.2	2.4.3	2.4.4
2.3.1	2.3.2	2.3.3	2.3.4
2.2.1	2.2.2	2.2.3	2.2.4
2.1.1	2.1.2	2.1.3	2.1.4

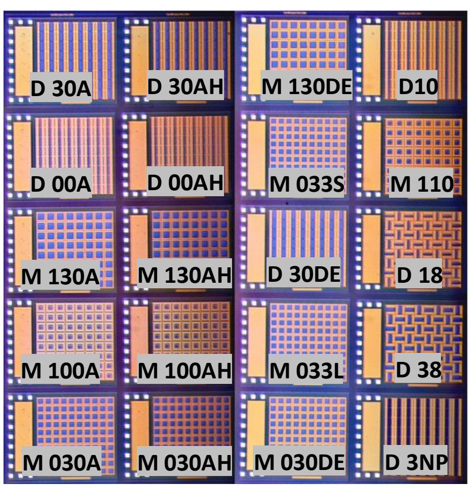

TOP CELL 3			
3.5.1	3.5.2	3.5.3	3.5.4
3.4.1	3.4.2	3.4.3	3.4.4
3.3.1	3.3.2	3.3.3	3.3.4
3.2.1	3.2.2	3.2.3	3.2.4
3.1.1	3.1.2	3.1.3	3.1.4

Fig.A.2: Sensor identification; on the left sensor Layout names and on the right packaging names of the sensors for each top cell.

Table A.1. Top Cell 1; Sensor Description

Module Name	NX	NY	pitch (um)	Aperture size (um)	Aperture fraction %	Cathode Separation (um)	Cathode type	Guard Ring	Grating Type	Checker board	1D	Amplifier	De-Embedding
D 10	8	8	125	20 ×125	16	107	113um,line	F	F	F	T	F	F
D 15	8	8	125	20 ×125	16	79.5	113um,line	F	F	F	T	F	F
D 20	8	8	125	31.25 ×125	25	107	113um,line	F	F	F	T	F	F
D 25	8	8	125	31.25 ×125	25	79.5	113um,line	F	F	F	T	F	F
D 30	8	8	125	45 ×125	36	107	113um,line	F	F	F	T	F	F
D 40	8	8	125	61.25 ×125	49	107	113um,line	F	F	F	T	F	F
M 110	8	8	125	50 × 50	16	107	91um,line	F	F	F	F	F	F
M 120	8	8	125	62.5 × 62.5	25	107	91um,line	F	F	F	F	F	F
M 130	8	8	125	75 × 75	36	107	91um,line	F	F	F	F	F	F
M 13N1	8	8	125	75 × 75	36	107	91um,line	F	0.5 um squares	F	F	F	F
M 13N2	8	8	125	75 × 75	36	107	91um,line	F	0.6 um squares	F	F	F	F
M 13N3	8	8	125	75 × 75	36	107	91um,line	F	0.75 um squares	F	F	F	F
M 13N4	8	8	125	75 × 75	36	107	91um,line	F	1 um squares	F	F	F	F
M 13NM	8	8	125	75 × 75	36	107	91um,line	F	4 by 4 array of above	F	F	F	F
M 13P1	8	8	125	75 × 75	36	107	91um,line	F	0.75 um squares + Poly.	F	F	F	F
M 13P2	8	8	125	75 × 75	36	107	91um,line	F	0.85 um squares + Poly.	F	F	F	F
M 13P3	8	8	125	75 × 75	36	107	91um,line	F	0.95 um squares + Poly.	F	F	F	F
M 13P4	8	8	125	75 × 75	36	107	91um,line	F	1 um squares + Poly.	F	F	F	F
M 13PM	8	8	125	75 × 75	36	107	91um,line	F	4 by 4 array of above	F	F	F	F
M 140	8	8	125	87.5 × 87.5	49	107	91um,line	F	F	F	F	F	F

Table A.2. Top Cell 2 Sensor Description

Module Name	NX	NY	pitch (um)	Aperture size (um)	Aperture fraction %	Cathode Separation (um)	Cathode Type	Guard ring	Grating	Checker board	1D	Amplifier	De-Embedding
D 00	8	8	125	11.25 ×125	9	107	113um,line	F	F	F	T	F	F
D 18	8	8	125	20 ×125	16	107	113um,line	F	F	T	T	F	F
D 38	8	8	125	45 ×125	36	107	113um,line	F	F	T	T	F	F
D 3N1	8	8	125	45 ×125	36	107	113um,line	F	0.225um ⊥ lines	F	T	F	F
D 3N2	8	8	125	45 ×125	36	107	113um,line	F	0.325um ⊥ lines	F	T	F	F
D 3N3	8	8	125	45 ×125	36	107	113um,line	F	0.425um ⊥ lines	F	T	F	F
D 3N4	8	8	125	45 ×125	36	107	113um,line	F	0.550um ⊥ lines	F	T	F	F
D 3NM	8	8	125	45 ×125	36	107	113um,line	F	4 by 4 array of above	F	T	F	F
D 3NV	8	8	125	45 ×125	36	107	113um,line	F	0.225um // lines	F	T	F	F
M 010	10	10	100	40 × 40	16	82	66um,line	F	F	F	F	F	F
M 020	10	10	100	50 × 50	25	82	66um,line	F	F	F	F	F	F
M 030	10	10	100	60 × 60	36	82	66um,line	F	F	F	F	F	F
M 031	10	10	100	60 × 60	36	82	33um,line	F	F	F	F	F	F
M 034	10	10	100	60 × 60	36	82	66um line , 2×2 um2 n+ well	F	F	F	T	F	F
M 100	8	8	125	37.5 × 37.5	9	107	91um,line	F	F	F	F	F	F
M 112	8	8	125	50 × 50	16	79.5	63.5um,line	T	F	F	F	F	F
M 115	8	8	125	50 × 50	16	79.5	63.5um,line	F	F	F	F	F	F
M 122	8	8	125	62.5 × 62.5	25	79.5	63.5um,line	T	F	F	F	F	F
M 125	8	8	125	62.5 × 62.5	25	79.5	63.5um,line	F	F	F	F	F	F
M 126	8	8	125	62.5 × 62.5	25	107	63.5um,line	F	F	F	F	F	F

Table A.3. Top Cell 3 Sensor Description

Module Name	NX	NY	pitch (um)	Aperture size (um)	Aperture fraction %	Cathode Separation (um)	Cathode type	Guard ring	Grating Type	Checker board	1D	Amplifier	De-Embedding
D 00A	8	8	125	11.25 ×125	9	107	113um,line	F	F	F	T	High Confidance	F
D 00AH	8	8	125	11.25 ×125	9	107	113um,line	F	F	F	T	High Performance	F
D 10	8	8	125	20 ×125	16	107	113um,line	F	F	F	T	F	F
D 18	8	8	125	20 ×125	16	107	113um,line	F	F	T	T	F	F
D 30A	8	8	125	45 ×125	36	107	113um,line	F	F	F	T	High Confidance	F
D 30AH	8	8	125	45 ×125	36	107	113um,line	F	F	F	T	High Performance	F
D 30DE	8	8	125	45 ×125	36	107	113um,line	F	F	F	T	F	T
D 3NP	8	8	125	45 ×125	36	107	113um,line	F	0.550um ⊥ lines +Poly	F	T	F	F
D 38	8	8	125	45 ×125	36	107	113um,line	F	F	T	T	F	F
M 030A	10	10	100	60 × 60	36	82	66um,line	F	F	F	F	High Confidance	F
M 030AH	10	10	100	60 × 60	36	82	66um,line	F	F	F	F	High Performance	F
M 030DE	10	10	100	60 × 60	36	82	66um,line	F	F	F	F	F	T
M 033L	10	10	100	60 × 60	36	82	33um corner line	F	F	F	F	F	F
M 033S	10	10	100	60 × 60	36	82	4umcorner line	F	F	F	F	F	F
M 100A	8	8	125	37.5 × 37.5	9	107	91um,line	F	F	F	F	High Confidance	F
M 100AH	8	8	125	37.5 × 37.5	9	107	91um,line	F	F	F	F	High Performance	F
M 110	8	8	125	50 × 50	16	107	91um,line	F	F	F	F	F	F
M 130A	8	8	125	75 × 75	36	107	91um,line	F	F	F	F	High Confidance	F
M 130AH	8	8	125	75 × 75	36	107	91um,line	F	F	F	F	High Performance	F
M 130DE	8	8	125	75 × 75	36	107	91um,line	F	F	F	F	F	T

APPENDIX B

SECOND GENERATION SENSOR PACKAGING

Fig.5.3 in Sec. 5.1 shows the pin configuration of the astrolabe sensor second generation sensors. The sensors are wire bonded to Kyocera KD-S86832 20 pin lead side brazed packages as shown in Fig.B.1. Work was done by VLSIP Technologies, Richardson 75081.

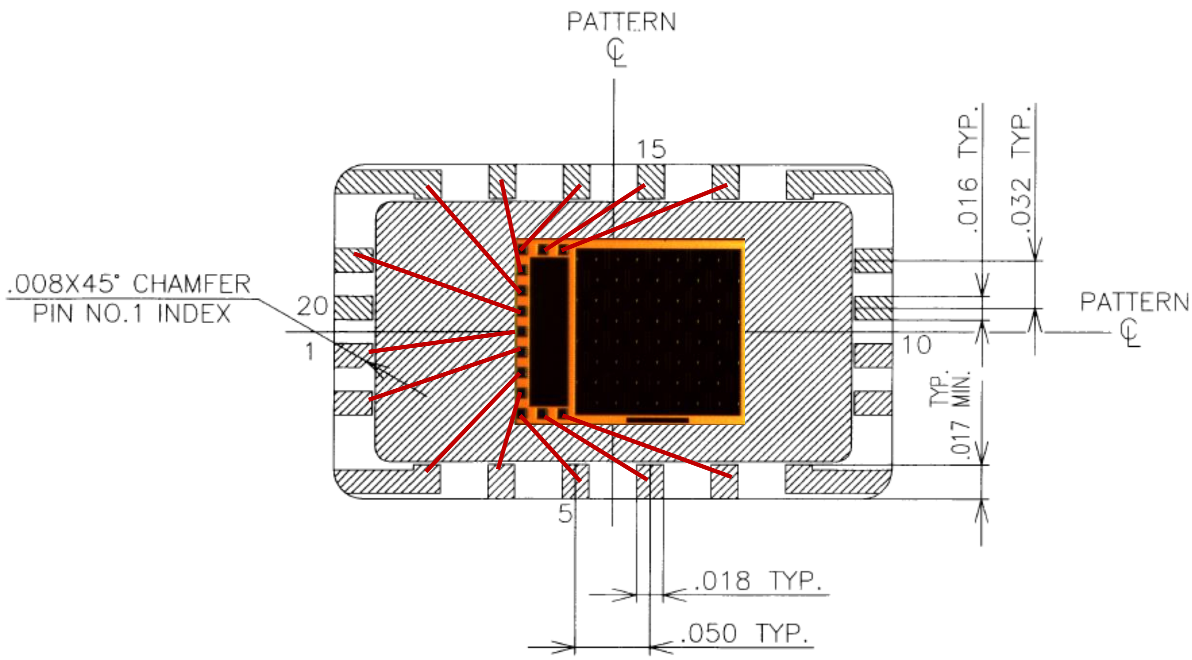

Fig.B.1: Packaged sensor, wire bonds are marked in red.

APPENDIX C

FRESNELS REFLECTION CALCULATIONS

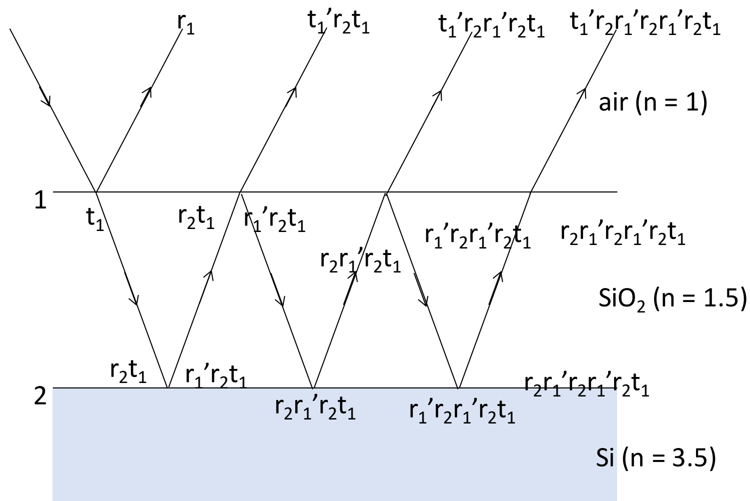

Fig.C.1: Reflections occur at the Si-SiO_2 interface

Fresnel Equations for Normal Incidence

$r_1 = (1–1.5)/(1+1.5) = –0.2$; $r_1' = –r_1 = 0.2$

$t_1 = 2(1)/(1+1.5) = 0.8$; $t_1' = 2(1.5)/(1+1.5) = 1.2$

$r_2 = (1.5–3.5)/(1.5+3.5) = –0.4$

Note: $t_1t_1' = 1 + r_1r_1'$

Sum the series of partial reflection amplitudes at air-to-SiO_2 interface:(assume SiO_2 is lossless)

$r_{total} = r_1 + t_1'r_2t_1 + t_1'r_2r_1'r_2t_1 + t_1'r_2r_1'r_2r_1'r_2t_1 + \ldots$

$= r_1 + (r_2t_1't_1)\,[1 + r_2r_1' + (r_2r_1')^2 + (r_2r_1')^3 + \ldots]$

$= r_1 + (r_2t_1't_1) / [1 – (r_2r_1')]$

$= –0.56$

Total power reflection coefficient:

$R = |r_{total}|^2 = 0.31$

Total power transmission coefficient to Si:

$P = 1 – R = 0.69$

APPENDIX D

TRACKING DEMONSTRATION

By making the connection in Fig.D.1 and pre run the code below in Arduino and post run in Realterm for the Arduino serial term one can obtain the *x* and *y* coordinates of the position of the light tag.

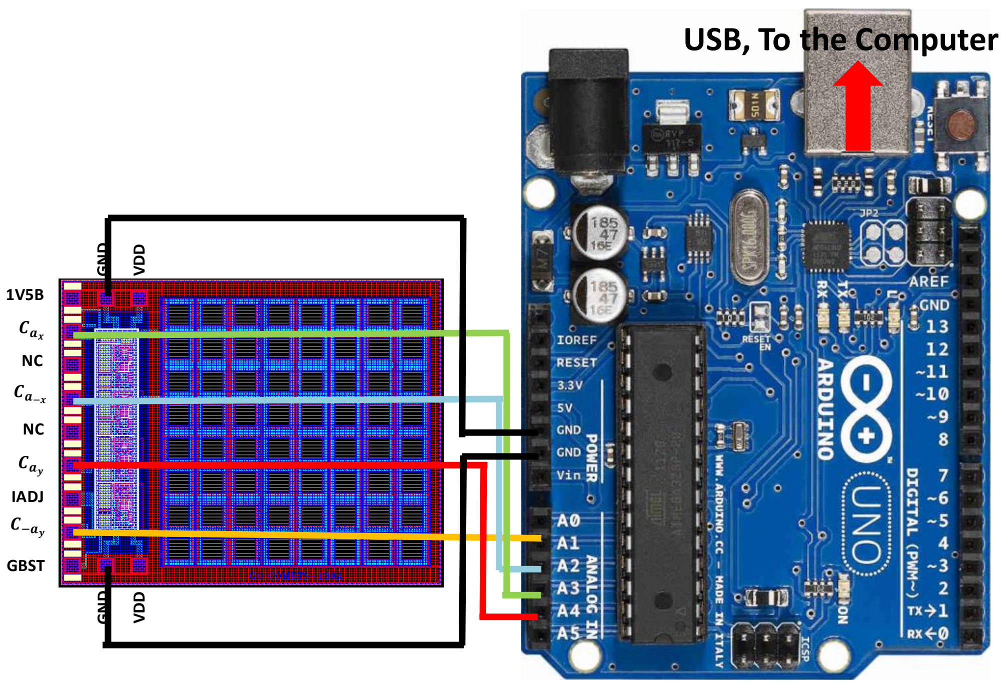

Fig.D.1: Sensor output and Arduino connections

Arduino code for the tracking demonstration

```
/*
 Measures the real signal value by substracting the ambient light value from the measured signal.
The signal is a pulsed LED source
*/
float v1,v2,v3,v4;          // Voltage measurements when LED is OFF (Ambient)
float V1,V2,V3,V4;          // Voltage measurements ehn LED is ON (Ambient + Signal)
```

```
float vol1,vol2,vol3,vol4;  // Effective signal (Signal)
float fy,fx;                // Angular functions
int T = 10;                 // Delay time in milliseconds
void setup()
{
  Serial.begin(230400);        // For transmitting data to the PC serially
  pinMode(LED_BUILTIN, OUTPUT); // LED switch control signal
}
void loop()
{
   digitalWrite(LED_BUILTIN, LOW);    // turn the LED off by making the voltage LOW
   delay(T);
   v1 = 5.0/1024.0 * analogRead(A1);   // Connected to channel 4 i.e. pin 4 of the astrolabe
   v2 = 5.0/1024.0 * analogRead(A2);   // Connected to channel 1 i.e. pin 19 of the astrolabe
   v3 = 5.0/1024.0 * analogRead(A3);   // Connected to channel 2 i.e. pin 17 of the astrolabe
   v4 = 5.0/1024.0 * analogRead(A4);   // Connected to channel 3 i.e. pin 2 of the astrolabe
   delay(10);        // delay in between reads for stability
//Serial.print(v1,4);
//Serial.print(" ");
//Serial.print(v2,4);
//Serial.print(" ");
//Serial.print(v3,4);
//Serial.print(" ");
//Serial.print(v4,4);
//Serial.println(" OFF");
  digitalWrite(LED_BUILTIN, HIGH);   // turn the LED on (HIGH is the voltage level)
  delay(T);                          // wait
  V1 = 5.0/1024.0 * analogRead(A1);
  V2 = 5.0/1024.0 * analogRead(A2);
```

```
  V3 = 5.0/1024.0 * analogRead(A3);
  V4 = 5.0/1024.0 * analogRead(A4);
  delay(10);                    // delay in between reads for stability
//Serial.print(V1,4);
//Serial.print(" ");
//Serial.print(V2,4);
//Serial.print(" ");
//Serial.print(V3,4);
//Serial.print(" ");
//Serial.print(V4,4);
//Serial.println(" ON");
vol1 = v1 - V1;         // Actual Signal value
vol2 = v2 - V2;         // Actual Signal value
vol3 = v3 - V3;         // Actual Signal value
vol4 = v4 - V4;         // Actual Signal value
//Serial.print(vol1,4);
//Serial.print(" ");
//Serial.print(vol2,4);
//Serial.print(" ");
//Serial.print(vol3,4);
//Serial.print(" ");
//Serial.print(vol4,4);
//Serial.println(" DIFFERENCE");
 fx = (vol2 - vol3)/(vol2 + vol3);    // Angular Function
 fy = (vol1 - vol4)/(vol1 + vol4);    // Angular Function
  Serial.print("X");
  Serial.println(fx,6);          // Transmit "X0.878345" (six decimal precision)
  Serial.print("Y");
  Serial.println(fy,6);          // Transmit "X0.878345" (six decimal precision)}
```

REFERENCES

[1] G. Nejat and B. Benhabib, "High-precision task-space sensing and guidance for autonomous robot localization," 2003.

[2] X. Zhang and Y. L. Sui J, "pplication of PSD in space point position measurement," in *IEEE The Eighth Int. Conf. Electronic Meas. and Instrum*, 2007.

[3] S. Nam and S. Oh, "Real-time dynamic visual tracking using PSD sensors and extended trapezoidal motion planning," *Applied Intelligence,* vol. 10, pp. 53-70, 1999.

[4] S. Blank, Y. Shen, N. Xi, Z. Zhang and U. C. Wejinya, "High precision PSD guided robot localization: design, mapping, and position control," in *Proc. of the 2007 IEEE/RSJ Int. Conf. Intelligent Robots and Syst*, 2007.

[5] A. Mäkynen, "Position-Sensitive Devices and Sensor Systems for Optical Tracking and Displacement Sensing Applications," Academic Dissertation, Univ. of Oulu, 2000.

[6] U. Wijesinghe, A. Dey, A. Marshall, W. Krenik, C. Duan, H. Edwards and M. Lee, "Integrated Circuit Angular Displacement Sensor with On-chip Pinhole Aperture," *Sensors (Basel),* vol. 20(6), 2020.

[7] R. Burns, J. Shah, C. Hong, S. Pepic, J. Lee, R. Homsey and P. Thomas, "Object location and centroiding techniques with CMOS active pixel sensors," *IEEE Trans. Electron. Dev*, vol. 50(12), p. 2369 2377, 2003.

[8] T. Constandinou and C. Toumazou, "micropower centroiding vision processor," IEEE J. Solid-State Circuits," *IEEE J. Solid-State Circuits*, vol. 61(6), pp. 1430-1443, 2006.

[9] M. Habibi and M. Sayedi, "High speed, low power VLSI CMOS vision sensor for geometric centre object tracking," *International J. Electronics,* vol. 96(8), pp. 821-836, 2009.

[10] L. Salles and D. de Lima Monteiro, "Designing the Response of and Optical Quad-Cell as Position-Sensitive Detector," *IEEE Sensors Journal,* vol. 10 (2), pp. 286-293, 2010.

[11] R. Exper-Chaín, A. Escuela, D. Fariña and S. J.R, "Configurable Quadrant Photodetector: An Improved Position Sensitive Device," *IEEE Sensors Journal,* vol. 16(1), pp. 109-119, 2016.

[12] J. T. Wallmark, "New Semiconductor Photocell Using Lateral Photoeffect," *Proc. IRE,* vol. 45(4), pp. 474-483, 1957.

[13] H. Woltring, "Single- and Dual-Axis Lateral Photodetectors of Rectangular Shape," *IEEE Trans. Electron. Dev.,* vol. 22 (8), pp. 581-590, 1975.

[14] H. Liu, Y. Xiao and Z. Chen, "A High Precision Optical Position Detector Based on Duo-Lateral PSD," *Proc. 2009 International Forum on Computer Science Technology and Applications,* pp. 90-92, 2009.

[15] J. Steiningera, M. Bibl, H. Yoo and G. Schitter, "High bandwidth deflection readout for atomic force microscopes," *Review of Scientific Instruments,* vol. 86, 2015.

[16] A. Mäkynen, J. Kostamovaara and R. Myllylä, "Displacement Sensing Resolution of Position-Senstive Detectors in Atmospheric Turbulence Using Retroreflected Beam," *IEEE Trans. Instrum. and Meas,* vol. 46(5), pp. 1133-1136, 1987.

[17] "Astrolabes," [Online]. Available: www.ifa.hawaii.edu/tops/astlabe.html. [Accessed 20 Oct 2020].

[18] J. Henry and J. Livingstone, "Comparison of Layered Metal-Semiconductor Optical Position Sensitive Detectors," *IEEE Sensors Journal,* vol. 2(4), pp. 372-376, 2002.

[19] M. Young, "Pinhole Optics," *Applied Optics,* vol. 10(12), pp. 2763-2767, 1971.

[20] M. Green, "Self-consistent optical parameters of intrinsic silicon at 300 K including temperature coefficients," *Sol. Energy Mater. Sol. Cells,* vol. 92, p. 1305–1310, 2008.

[21] W. West, Absorption of electromagnetic radiation, McGraw-Hill Education, 2014.

[22] H. Carslaw and J. J.C, Conduction of Heat in Solids, Oxford: Clarendon Press, 1959.

[23] D. Schroeder, An Introduction to Thermal Physics, New York: Addison Wesley Longman, 2000.

[24] M. Born and E. Wolf, Principles of Optics, Cambridge University Press, 1999.

[25] M. Abramowitz and I. Stegun, Handbook of Mathematical Functions,, California: U.S. Government Printing Office, 1970.

[26] I. Gradshteiyn and R. I.M, Table of Integrals, Series, and Products, Elsevier Science, 2007.

[27] I. Synopsys,"Taurus TSUPREM-4," 2020. [Online]. Available: https://www.synopsys.com/silicon/tcad/process-simulation/taurus-tsuprem-4.html. [Accessed 20 10 2020].

[28] I. Synopsys, "Taurus Medici," 2020. [Online]. Available: https://www.synopsys.com/silicon/tcad/device-simulation/taurus-medici.html. [Accessed 20 10 2020].

[29] G. Barbottin and A. Vapaille, "Instabilities in silicon devices : silicon passivation and related instabilities," *Materials Science,* vol. 1 (1), 1986.

[30] S. Sze and K. Ng, Physics of Semiconductor Devices, New Jersey: John Wiley & Sons, Inc, 2007.

[31] S. Hava, J. Ivri, M. Auslender and B. Lacquet, "Reflection of infrared radiation from lamellar gratings on a silicon wafer," *J. Appl. Phys,* vol. 83(3), 1997.

[32] Y. Suido, Y. Yamamoto, G. Thomas, Y. Ajiki and T. Kan, "Extension of the Measurable Wavelength Range for aNear-Infrared Spectrometer Using a Plasmonic Au," *Micromachines,* vol. 10(403), 2019.

[33] D. Cai, Y. Lu, K. Lin, P. Wang and H. Ming, "Improving the sensitivity of SPR sensors based on gratings by double-dips method (DDM)," *Opt. Express,* vol. 16, p. 14597, 2008.

[34] L. Cheng, S. Mao, Z. Li, Y. Han and H. Fu, "Grating Couplers on Silicon Photonics: Design Principles, Emerging Trends and Practical Issues," *Micromachines,* vol. 11 (666), 2020.

[35] J. Munday and H. Atwater, "Large Integrated Absorption Enhancement in Plasmonic Solar Cells by Combining Metallic Gratings and Antireflection Coatings," *Nano Lett.,* vol. 11, p. 2195–220, 2011.

[36] H. Raut, V. Ganesh, A. Nair and S. Ramakrishna, "Anti-reflective coatings: A critical, in-depth review," *Energy Environ. Sci,* vol. 4, p. 3779, 2011.

[37] S. Li, Semiconductor Physical Electronics, New York: Springer, 2006.

[38] K. Böer and U. Pohl, Carrier Recombination and Noise, Springer , 2017.

[39] L. P.T, "Auger effect in semiconductors," *Solid State Electron,* vol. 30, p. 1107, 1987.

[40] K. Vliet and H. Mehta, " Theory of transport noise in semiconductors," *Phys Stat Sol,* vol. B 106, 1981.

[41] K. Vliet and V. Ziel, "On the noise generated by diffusion mechanisms," *Physica,* vol. 24, p. 415, 1958.

[42] M. Law, E. Solley, M. Liang and D. Burk, "Self-Consistent Model of Minority-Carrier Lifetime, Diffusion Length, and Mobility," *IEEE Electron Device Lett.,* vol. 12(8), 1991.

[43] P. Altermatt, H. Plagwitz, R. Bock, J. Schmidt, R. Brendel, M. Kerr and A. Cuevas, "The surface recombination velocity at boron-doped emitters: Comparison between various passivation techniques," in *21st European Photovoltaic Solar Energy Conference,* Dresden, Germany, 2006.

[44] K. S.O, Principles of Electronic Materials and Devices, New York: McGraw-Hill, 2006, p. 559.

[45] J. H. Scofield, "Frequency-domain description of a lock-in amplifier," *American Journal of Physics*, vol. 62 (2), p. 129–133, 1994.

[46] R. Wolfson, "The lock-in amplifier: A student experiment," *American Journal of Physics*, vol. 59 (6), p. 569–572, 1991.

BIOGRAPHICAL SKETCH

Udumbara Wijesinghe was born in Kandy, Sri Lanka, one of the most beautiful places on Earth. She is an artist inspired by the balance and symmetry of mother nature. With time she learned the similarities between art and science and wanted to become a scientist who can create something great.

In 2012 she received her Bachelor of Science degree in Physics and Chemistry from the University of Peradeniya. During her bachelor's degree, she learned about nanotechnology's marvelous inventions from science news and magazines and wanted to contribute with her knowledge in physics and chemistry. The following year Udumbara was admitted to the Post Graduate Institute in Science University of Peradeniya and received her Master of Science in Nanoscience and Nanotechnology in 2014. While she was studying for her master's degree, she realized her fundamental knowledge in physics was not enough and was fascinated by the idea of being in a classroom with scientists from all over the world. In 2015 she attended The University of Texas at Dallas. During her five years at The University of Texas at Dallas, she completed three degrees, Master of Science in Physics, Master of Science in Materials Science and Engineering, and Doctor of Philosophy in Materials Science and Engineering. She also works as a visiting researcher and a Process Integration Engineering intern at Texas Instruments. During her PhD, working with Texas Instruments, she learned how to apply physics theories to semiconductor device engineering and discovered a new canvas where she can design innovative semiconductor devices. She will be joining Texas Instruments in 2021 as a Process Integration Engineer.

Udumbara thinks knowing one thing is boring and wants to be the next Leonardo da Vinci, a scientist, engineer and inventor who is remembered as an artist.

CURRICULUM VITAE

EDUCATION

University of Texas at Dallas, Richardson, TX

Doctor of Philosophy in Materials Science and Engineering 2020

Master of Science in Materials Science and Engineering 2020

Area of Study: Optical Sensors

University of Texas at Dallas, Richardson, TX

Master of Science in Physics 2017

Area of Study: Quantum Well Silicon NMOS Transistors

Post Graduate Institute in Science University of Peradeniya, Sri Lanka

Master of Science in Chemistry: Nanoscience and Nanotechnology 2014

Area of Study: Semiconductor Thin Films

University of Peradeniya, Sri Lanka

Bachelor of Science in Physics and Chemistry 2012

WORK EXPERIENCE

Graduate Research Assistant

University of Texas at Dallas Spring 2018-Fall 2020

Process Integration Engineering Intern

Analog Technology Development Department at Texas Instruments Summer 2020

Visitor Research Student

Texas Instruments May 2019 – May 2020

Graduate Teaching Assistant

Department of Bioengineering at University of Texas at Dallas Fall 2017

Graduate Teaching Assistant

Department of Physics at University of Texas at Dallas Fall 2015-Spring 2017

PROFICIENT TOOLS AND PROGRAMMING LANGUAGES

Programming Languages: Matlab, LabVIEW, C, Sentaurus, TSuprem, Medici, Cadence layout environment (Virtuoso, Assura DRC checking and layout optimization, Cadence SKILL programming for layout automation), Arduino, Realterm, Spotfire

Proficient Tools: Machine Shop training (Completed 2 levels out of 5 at UTD Machin Shop), CPX-VF Probe Station, 4156 Precision Semiconductor Parameter Analyzer, SR770 FFT Network Analyzer, Optical Table

PROJECTS

Astrolabe Optical Sensor 2017

Measurements of Negative and Positive Gain in Quantum Well Silicon NMOS transistors 2016

Optical and Electrical Properties of Copper doped Zinc Oxide thin films 2015

PUBLICATIONS

Udumbara Wijesinghe, Akash Dey, Andrew Marshall, William Krenik, Can Duan, Hal Edwards, Mark Lee, "Integrated Circuit "Astrolabe" Angular Displacement Sensor Using On-chip Pinhole Optics", MDPI Sensors. 20, 6, 1794 (2020)

Gangyi Hu, **Udumbara Wijesinghe**, Clint Naquin, Ken Maggio, H. L. Edwards, Mark Lee, "Positive and Negative Gain Exceeding Unity Magnitude in Silicon Quantum Well MetalOxide-Semiconductor Transistors", Appl. Phys. Lett. 111, 153503 (2017)

P. Samarasekara, **Udumbara Wijesinghe**, Eranji Jayaweera, "Impedance and Electrical Properties of Cu doped ZnO Thin Films", GESJ:Physics (2015)

P. Samarasekara, **Udumbara Wijesinghe**, "Optical properties of spin coated cu doped zno nanocomposite films", GESJ:Physics (2015)

PROFESSIONAL & HONOR SOCIETIES

American Vacuum Society (Secretary)

University of Texas at Dallas 2019- 2020

Materials Science and Engineering Student Representation Committee (General Member)

University of Texas at Dallas 2019

Institute of Electrical and Electronics Engineers (Member)

University of Texas at Dallas 2019